Defense Threat Reduction Agency
8725 John J. Kingman Road, MS
6201 Fort Belvoir, VA 22060-6201

DTRA-TR-18-2

TECHNICAL REPORT

Combining Advanced Turbulent Mixing and Combustion Models with Advanced Multi-Phase CFD Code to Simulate Detonation and Post-Detonation Bio-Agent Mixing and Destruction

October 2017

HDTRA1-11-1-0053

Suresh Menon and
Michel Akiki

Prepared by:

School of Aerospace
Engineering, Georgia
Institute of Technology
270 Ferst Dr
Atlanta, GA 30332

DESTRUCTION NOTICE:

Destroy this report when it is no longer needed.
Do not return to sender.

PLEASE NOTIFY THE DEFENSE THREAT REDUCTION AGENCY, ATTN: DTRIAC/ J9STT, 8725 JOHN J. KINGMAN ROAD, MS-6201, FT BELVOIR, VA 22060-6201, IF YOUR ADDRESS IS INCORRECT, IF YOU WISH IT DELETED FROM THE DISTRIBUTION LIST, OR IF THE ADDRESSEE IS NO LONGER EMPLOYED BY YOUR ORGANIZATION.

REPORT DOCUMENTATION PAGE

Form Approved
OMB No. 0704-0188

1. REPORT DATE *(DD-MM-YYYY)*	**2. REPORT TYPE**	**3. DATES COVERED** *(From - To)*
19-10-2017	Technical	1 July 2011 - 30 April 2016

4. TITLE AND SUBTITLE

Combining Advanced Turbulent Mixing and Combustion Models with Advanced Multi-Phase CFD Code to Simulate Detonation and Post-Detonation Bio-Agent Mixing and Destruction

5a. CONTRACT NUMBER

5b. GRANT NUMBER
HDTRA1-11-1-0053

5c. PROGRAM ELEMENT NUMBER

6. AUTHOR(S)

MICHEL AKIKI
SURESH MENON

5d. PROJECT NUMBER

5e. TASK NUMBER

5f. WORK UNIT NUMBER

7. PERFORMING ORGANIZATION NAME(S) AND ADDRESS(ES)

School of Aerospace Engineering, Georgia Institute of Technology Colorado
270 Ferst Dr
Atlanta, GA 30332

8. PERFORMING ORGANIZATION REPORT NUMBER

CCL-TR-2016-06-19

9. SPONSORING / MONITORING AGENCY NAME(S) AND ADDRESS(ES)

Defense Threat Reduction Agency
8725 John J. Kingman Road, STOP 6201
Fort Belvoir, VA 22060-6201

10. SPONSOR/MONITOR'S ACRONYM(S)

DTRA

11. SPONSOR/MONITOR'S REPORT NUMBER(S)

DTRA-TR-18-2

12. DISTRIBUTION / AVAILABILITY STATEMENT

Distribution Statement A. Approved for public release; distribution is unlimited.

13. SUPPLEMENTARY NOTES

14. ABSTRACT

This work is focused on the development of computational models for the simulation of blast waves, heterogeneous combustion and their interaction with particle dispersion. In particular, a novel Eulerian-Lagrangian (EE/EL) hybrid approach is combines a hybrid Eulerian and Lagrangian framework for dense loading of particles. The Eulerian approach (EE) tracks particles in the dense regime however in the dilute regime the Lagrangian formulation becomes superior. Transition from dense to dilute is achieved by locally tracking the volume loading and at present, using a numerically determine transfer criteria. Verification and validation tests are conducted using canonical cases and compared to analytical and/or data as available. Good agreement is demonstrated, although further studies are still warranted.

15. SUBJECT TERMS

Detonation, Multi-room Blast, EE-EL modeling, Dense Sprays

16. SECURITY CLASSIFICATION OF:			**17. LIMITATION OF ABSTRACT**	**18. NUMBER OF PAGES**	**19a. NAME OF RESPONSIBLE PERSON**
a. REPORT	**b. ABSTRACT**	**c. THIS PAGE**	SAR	129	Allen Dalton
Unclassified	Unclassified	Unclassified			**19b. TELEPHONE NUMBER** *(include area code)* 703-767-3054

UNIT CONVERSION TABLE

U.S. customary units to and from international units of measurement*

U.S. Customary Units	Multiply by → / ← Divide by†		International Units
Length/Area/Volume			
inch (in)	2.54	$\times 10^{-2}$	meter (m)
foot (ft)	3.048	$\times 10^{-1}$	meter (m)
yard (yd)	9.144	$\times 10^{-1}$	meter (m)
mile (mi, international)	1.609 344	$\times 10^{3}$	meter (m)
mile (nmi, nautical, U.S.)	1.852	$\times 10^{3}$	meter (m)
barn (b)	1	$\times 10^{-28}$	square meter (m^2)
gallon (gal, U.S. liquid)	3.785 412	$\times 10^{-3}$	cubic meter (m^3)
cubic foot (ft^3)	2.831 685	$\times 10^{-2}$	cubic meter (m^3)
Mass/Density			
pound (lb)	4.535 924	$\times 10^{-1}$	kilogram (kg)
unified atomic mass unit (amu)	1.660 539	$\times 10^{-27}$	kilogram (kg)
pound-mass per cubic foot (lb ft^{-3})	1.601 846	$\times 10^{1}$	kilogram per cubic meter (kg m^{-3})
pound-force (lbf avoirdupois)	4.448 222		newton (N)
Energy/Work/Power			
electron volt (eV)	1.602 177	$\times 10^{-19}$	joule (J)
erg	1	$\times 10^{-7}$	joule (J)
kiloton (kt) (TNT equivalent)	4.184	$\times 10^{12}$	joule (J)
British thermal unit (Btu) (thermochemical)	1.054 350	$\times 10^{3}$	joule (J)
foot-pound-force (ft lbf)	1.355 818		joule (J)
calorie (cal) (thermochemical)	4.184		joule (J)
Pressure			
atmosphere (atm)	1.013 250	$\times 10^{5}$	pascal (Pa)
pound force per square inch (psi)	6.984 757	$\times 10^{3}$	pascal (Pa)
Temperature			
degree Fahrenheit (^oF)	$[T(^oF) - 32]/1.8$		degree Celsius (^oC)
degree Fahrenheit (^oF)	$[T(^oF) + 459.67]/1.8$		kelvin (K)
Radiation			
curie (Ci) [activity of radionuclides]	3.7	$\times 10^{10}$	per second (s^{-1}) [becquerel (Bq)]
roentgen (R) [air exposure]	2.579 760	$\times 10^{-4}$	coulomb per kilogram (C kg^{-1})
rad [absorbed dose]	1	$\times 10^{-2}$	joule per kilogram (J kg^{-1}) [gray (Gy)]
rem [equivalent and effective dose]	1	$\times 10^{-2}$	joule per kilogram (J kg^{-1}) [sievert (Sv)]

*Specific details regarding the implementation of SI units may be viewed at http://www.bipm.org/en/si/.

†Multiply the U.S. customary unit by the factor to get the international unit. Divide the international unit by the factor to get the U.S. customary unit.

TABLE OF CONTENTS

LIST OF TABLES

LIST OF FIGURES

CHAPTER I

EXECUTIVE SUMMARY

This work is focused on the development of computational models for the simulation of blast waves, heterogeneous combustion and their interaction with particle dispersion. In particular, an Eulerian-Lagrangian (EE/EL) hybrid approach is formulated. In this approach, the concept is to employ the Eulerian framework for the dense part of the particles. The Eulerian approach (EE) is suitable for the simulation of dense regimes with a particular advantage of efficiently simulating a large number of particles. This is made possible by assuming a body of particles instead of individually tracking each particle. However, this assumption is weakened and becomes inaccurate in a dilute regime. At this point, the Lagrangian formulation becomes superior. Such transitions from dense to dilute is a common encounter in the dispersion of particles due to blast waves. Our hybrid implementation takes into account the regimes of the particles being simulated and employs the appropriate formulation, which provides the advantages of both worlds while maintaining the required level of accuracy.

To achieve this goal, the implementation of the approach is first validated in three classic test cases with experimental or theoretical validation. The first is the Sedov case where the pressure decay and blast wave front are validated based on analytical solutions. In this test case, the Adaptive Mesh Refinement (AMR) capabilities are also validated. The second is the Boiko case where experimental data for the dispersion of a cloud of particles in a confined tube are available. The good agreement of the results from these simulations validate the EE, EL and hybrid EE/EL approach. The third validation case is the Rouge case which employs a similar setup to Boiko's. These results validate the EE/EL approach as well as the implementation of the Discrete Element Method (DEM).

After validating the numerical approach and its implementation, several cases with relevance to blast wave applications have been performed and analyzed. A first study simulates the propagation of a blast wave due to a spherical charge of TNT in a confined room with a window or vent. The simulation captures the various wave interactions as well as the wall reflections to form pressure focusing. The results also demonstrate the shape imprinting on the wave front from the initial geometrical and structural features of the room and charge. Another study observes the qualitative differences in the detonation of a cylindrical charge with two configurations of detonators. The first configuration consists of a detonator along the axis of the cylindrical charge. In this manner, the detonation wave travels in a radially symmetric manner. This allows the assumption of using a detonation profile at the moment the charge has been consumed completely to initialize the propagation of the blast wave. The second configuration sets the detonator at the center of the charge which causes two detonation waves propagating axially from the center to the extremities. In this case, the condensed phase propagation is required to be resolved, which renders the simulation costly. The results show a substantial influence of the initial stages on the longer term blast wave shape and propagation.

A more complex application that combines the features of the previous simulations is

the propagation of a blast wave in rooms connected with hallways. In this case, C4 and Nitro-methane charges are used. The simulation captures the wave interactions, reflections, and pressure focusing, and carbon soot is tracked. Comparisons of pressure confinement with one room and rooms with hallways depict the expected pressure relief. Additionally, the effect of the charge shape, after-burning, and spore aerosol modeling has been studied.

Building on these studies, a two-room configuration is implemented to study the dispersion of particles due to a blast wave in a confined room. The two-room comes into play because of a vent in the first room that would disperse the soot particles and pressure wave into the larger room. A cloud of spore particles is initialized in a corner of the smaller room to investigate their survivability. Results show hydrodynamic instabilities due to RMI and RTI particularly at the locations where the reflected pressure waves encounter detonation products. When the blast wave contacts the spore particles, the spore particle cloud is deformed along the contact surface of the shock. The spores are driven towards the wall, and pushed onto the corner of the inner room with relatively higher gaseous temperature.

In another study, wave interactions due to multi-blasts are investigated. These also include pressure wave interactions with a fixed wall. Finally, a study employing the transition of a shock to detonation and then to a blast wave is performed to study the influence of micro-structural changes in the energetic material on the long term blast wave. Three configurations are studied where the charge constitutes of either pure energetic material or contains crystals with a polymer binder. Additionally, the shock location is varied. The results show a substantial influence of minute changes in the initial micro-structure on the resulting blast wave and turbulent mixing.

CHAPTER II

INTRODUCTION/MOTIVATIONS

Deployment of explosives is ubiquitous in several engineering industries encompassing numerous different applications ranging from mining to modern warfare, from fire quenching in oil field to agent-defeat etc. Although explosions have been widely studied by the research community for well over a century, many phenomena still remain to be investigated in order to properly understand and characterize the flow-field in the post-detonation regime. The complexity of post-detonation flow field aided by vigorous turbulent mixing can be distinctive due to the presence of many scales of motions, flow jetting, high level of shearing motion, plume surface interactions etc. All these imply that an initial quiescent ambient can become highly turbulent in the post-detonation regime which in turn can affect the final after burning significantly. In addition to this, when detonation is being initiated in a confined space, it can generate higher level of pressure load. When the incident pressure wave impinges on a structure that is not parallel to the direction of the wave travel, it is reflected and reinforced, producing what is known as reflected pressure. The reflected pressure is the force to which the structure ultimately responds.

The problem of explosions in the presence of particles waxes the complexity by an order of magnitude as the flow now involves strong discontinuities such as shocks and contact surfaces, as well as smooth flow regions such as shear layers. Also, efficient measures have to be taken to track these particles accurately without penalizing the computational efficiency. In general these particles can be reactive e.g. soot particles, bio-agents etc. which can be ignited by blast wave and eventually combusted via its entrainment into flames. In addition to this, more than one type of particles may be present in the domain e.g. bio-agents and Aluminum, soot and Aluminum etc. which might react with each other as well. Overall, there exists a plethora of challenges when it comes to model explosions with particles. The dispersion of these particles is highly transient involving wide gamut of length and time scales. The detonation generated plume can impact the dispersion, mixing and burn-out. Due to this, in-homogeneous mixing resulting in plume-induced instability (i.e. RM instability) can aggravate burn-out or augment dispersion. Confined space adds to the flow complexity by introducing corner recirculation, pressure wave reflections etc. Also, in confined spaces, mixing process is much more rapid to allow combustion-induced pressure waves to coalesce and create sustained pressure loads on the walls. Characterization of the particle behavior in the post-detonation regime inside a confined space is an active area of research which requires accounting for the particle-turbulence- shock/detonation-chemistry interactions in complex three dimensional flows. The present research effort aims to address some of these issues.

Experimental measurements can be highly expensive and difficult to perform as the ambient is hostile. Simulation can play a critical role in this scenario. However, simulating this kind of complex flow mandates to use higher order spatial and temporal accuracy that can be achieved by direct numerical simulation (DNS) or large-eddy simulation (LES). DNS

with its huge computational requirement is beyond the scope of current and perhaps, the near-future hardware capability. On the other hand, LES of these complex flows requires advanced sub-grid models as well as a robust parallel code. Application and validation of the complex turbulent reacting flows have been demonstrated previously by the 3D LES code developed and maintained in the Computational Combustion Lab (CCL) at Georgia Institute of Technology (called LESLIE3D, hereafter) under DTRA funded work. The current effort aims to evaluate the capability of the code by validating it against the confined space explosion results. The next step is to enhance the capability of the code by incorporating improved sub-grid models for calculating particle dispersion.

The goal of this report is to summarize the progress made so-far in order to build a simulation capability to perform and predict the complex physics of detonations and blast waves together with its interaction with particle dispersion and heterogeneous combustion in confined spaces. The report is organized as follows: Section 2.1.2 presents the technical objectives and statement of the work. Section 2.1.3 states the experimental configuration which is followed by computational setup in Section 2.1.4. Section 2.1.5 deals with the numerical setup. Section 2.1.6 discusses the results. The report is wrapped up with Section 2.1.7 which summarizes future plans of this project.

CHAPTER III

OBJECTIVES

The primary objective of this effort was to develop and deploy a state-of-the-art and next-generation simulation tool for WMD studies that includes advanced subgrid models for turbulent momentum and scalar mixing, and combustion in complex domains.

The proposed study will leverage the availability of both turbulent mixing models and ANN based reaction kinetics and enhance them with new subgrid models for spores. Both detonations and shear turbulence, are captured in the solver using a hybrid approach that combines a robust shock capturing model with a less dissipative O(4) central scheme in regions without strong discontinuities. A Lagrangian particle-tracking model can track liquid and/or solid particles with full coupling between the phases [25, 4, 6]. This solver has been successfully employed to simulate RM instability, gas and two-phase detonations. Effect of collisions between parcels and within the parcel is included. This method will allow modeling the effect of collisions, non-spherical particles and local clustering.

Whereas the research in Georgia Tech is basic (unclassified) research investigating fundamental mixing and combustion processes our partner CRAFT-Tech has developed an advanced CFD code capable of simulating many complex (and restricted) problems of interest to DTRA, such as tests at Eglin AFB and Ladeburg Bunker in Germany. The CRAFT-Tech code is well established with a long history of application to many classified test cases. This combined effort will add sub models developed in Georgia Tech to enhance this codes capability for these applications.

The following technical objectives apply to both members of this research team.

1. Establish a new coupled Eulerian-Lagrangian approach to track dense clouds of particles with particular emphasis on subgrid models for spore physics, spore distribution and its response to turbulent mixing in the post detonation flow field.

   A dense Lagrangian particle-tracking model is being validated in Georgia Tech currently under exiting DTRA funding [15, 16]. This method track parcels as in a Lagrangian approach but also includes a subgrid stochastic model to account for local clustering. A key advantage of this model is that it can approximate the presence of large number of small particles in a subgrid cloud without explicitly tracking each of the particles. Thus, it has the ability to track a very large number of particles in a deterministic but cost-effective manner. This approach offers an approach to track particle distribution changes locally (due to afterburning, collisions/merger, breakup, etc.) unlike a classical volume fraction based Eulerian approach. Therefore, it has the potential to deal with spore clouds as well as Al particles in the explosives and their interactions. The current approach is very fundamental (studies in isotropic turbulence, spray dispersion etc) but will have to be generalized to deal with walls etc. Extension of the model to handle subgrid turbulence (i.e., turbulence at the small scales), spore sub-models (including kinetics)

2. Validate and implement computationally efficient rate kinetics using advanced lookup approaches based on ANNs for thermobaric explosive and spore mechanism.

   To study the physics of thermobaric explosives, detailed (or at least multi-step) kinetics or finite rate models are needed for accurate prediction of afterburning, spore thermal and chemical neutralization mechanisms. Due to a wide range of scales computational cost of full-scale problems can become prohibitively expensive, and on top of this there is a need for proper treatment under turbulent mixing conditions. The subgrid model developed in Georgia Tech has combined a turbulent mixing model with finite rate kinetics and also developed efficient ANNs to paratemetrize rate mechanisms. This strategy will be extended for the current applications and integrated into the simulation codes.

3. Integration of turbulent mixing and combustion models into full-scale production code for DTRA related restricted application studies This objective will transition all the models developed during this research into the CRAFT Tech production code and then this will be used to study various test cases identified by DTRA. Further refinements may be needed and will be part of this overall objective. Another part of this effort will be the release of some versions of the codes for DTRA use in Federal Laboratories, as requested.

The goals are specifically driven by DTRA's requirement to obtain greater confidence in the accuracy of computational simulations involving advanced high energy explosives in closed compartments/structures and agent defeat simulations with lower energy release and dispersion for neutralizers. The overarching technical objective is to assess the ability in capturing the effects of turbulent mixing, disparate time-scales, multi-phase physics and scenario input uncertainty on AD in a complex geometry.

CHAPTER IV

MATHEMATICAL FORMULATION AND NUMERICAL METHODOLOGY

4.1 Modeling

There are different modeling approaches for simulating two-phase flows, which depend upon parameters such as mass and volume loading, Stokes number, spray regime and the method used for simulating the carrier phase [37, 38, 39]. Some of the typical approaches to numerically model practical multiphase flow systems are denoted as Eulerian-Lagrangian (EL), Eulerian-Eulerian (EE), hybrid and statistical methods (others may exist but are not addressed here). Table 4.1 summarizes some of these models used to study swirling spray combustion (non-swirling spray mixing and combustion are not directly addressed here). A brief description of these methods with their advantages and limitations is provided below.

In the Eulerian-Eulerian approach, also referred to as the two-fluid method [40, 41, 38, 39], both carrier and disperse phases are solved using an Eulerian framework. The two phases are considered to be interpenetrating and requires transport equations for the volume fraction, velocity, temperature and moments of size distribution of the dispersed phase, which is obtained after homogenization. The mass, momentum and energy exchange with the carrier phase occurs through source/sink terms. Since the method utilizes a common Eulerian framework, consistent numerical method can be used for both phases, thus leading to easy implementation and scalable high-performance parallel computing. However, the method requires substantial initial modeling effort to obtain the aforementioned transport equations for the dispersed phase. Additionally, the method is considered to be expensive for polydisperse systems, although there have been some development to deal with multisize particle sprays in a computationally efficient manner [42]. Another limitation of the method is associated with the numerical stability, which requires that the concentration gradient should not be very high for the disperse phase within the flow system.

In the Eulerian-Lagrangian method, Lagrangian tracking of the dispersed phase is performed and the carrier phase is simulated using the conventional Eulerian framework [43, 44, 45, 46]. The EL method is the most common approach to simulate flow systems considered here, due to its robustness, accuracy and ability to model complex phenomena such as poly-dispersity, particle/wall and particle-particle interactions, crossing trajectories, and particle break-up. However, the method is computationally expensive, as large number of particles are required within each computational cell used by the carrier phase to allow for a smooth Eulerian reconstruction of the feedback force to the carrier phase.

Another major issue with the EL method is related to the accuracy of the dispersed phase statistics, which is dependent on the number of particles, particularly in regions of a physically observed sparse distribution of the disperse phase. In general, the convergence rate of the dispersed phase statistics by the EL method scales as $N^{-1/2}$, where N is the

Table 4.1: Modeling approaches for simulating typical swirling spray combustors.

Method	References	Remarks
Eulerian-Eulerian	[4, 5, 6, 7, 8, 9, 10, 11, 12]	Scalable parallelization, consistent numerical method, subtantial modeling effort, expensive for polydisperse systems
Eulerian-Lagrangian	[13, 14, 15, 16, 17, 18, 19, 20, 21]	Robust for complex systems,
	[22, 8, 10, 23, 24, 25, 26, 27, 28, 29]	slower statistical convergence, inefficient parallelization,
Hybrid	[30, 31]	computationally expensive
Statistical	[32, 33, 34, 35, 36]	Consistent numerical method, closure is simpler, easy to parallelize, computationally expensive

number of particles in any parcel of the domain. Regions that have low number density tend to be poorly converged because N is small in comparison with regions where N is large.

The density-weighted spatially filtered LES equations can be obtained from the compressible form of the multi-species Navier-Stokes equations by employing the well known Favre filtering approach. The Favre filtered (resolved) quantity corresponding to a field variable $\phi(\boldsymbol{x}, t)$ is defined as

$$\widetilde{\phi}(\boldsymbol{x}, t) = \frac{1}{\overline{\rho}(\boldsymbol{x}, t)} \int_{\Omega} G(\boldsymbol{x}, \boldsymbol{x}' - \boldsymbol{x}) \rho(\boldsymbol{x}', t) \phi(\boldsymbol{x}', t) d\boldsymbol{x}', \tag{4.1}$$

where Ω is the computational domain, G is a spatial filter function, ρ is the density and $\overline{(.)}$ denotes the conventional spatial filtering, which when applied to the density field $\rho(\boldsymbol{x}, t)$ leads to the spatially filtered density field $\overline{\rho}(\boldsymbol{x}, t)$ given by

$$\overline{\rho}(\boldsymbol{x}, t) = \int_{\Omega} G(\boldsymbol{x}, \boldsymbol{x}' - \boldsymbol{x}) \rho(\boldsymbol{x}', t) \; d\boldsymbol{x}'. \tag{4.2}$$

Note that the two filtering approaches are related through $\overline{\rho\phi} = \overline{\rho}\widetilde{\phi}$.

The interphase coupling of the gas phase, the Lagrangian dispersed phase and the Eulerian dispersed phase can be tracked in terms of the volume fraction through

$$\overline{\alpha}_g + \overline{\alpha}_p + \overline{\alpha}_d = 1, \tag{4.3}$$

where $\overline{\alpha}_g$, $\overline{\alpha}_p$ and $\overline{\alpha}_g$ denote volume fraction of the gas phase, Lagrangian dispersed phase and Eulerian dispersed phase, respectively. The volume fraction of the Lagrangian dispersed phase $\overline{\alpha}_p$ is defined as

$$\overline{\alpha}_p = \frac{1}{\Delta V} \sum_{n=1}^{N} n_{p,n} \left[\frac{4}{3} \pi r^3{}_{p,n} \right], \tag{4.4}$$

where ΔV is the volume of the computational cell, n_p is the number of particles in each particle group (referred to as a parcel) and N is the total number of parcels in the computational cell. The volume fraction of the gas phase $\overline{\alpha}_g$ evolves in space and time according to

$$\frac{\partial \overline{\alpha}_g}{\partial t} + \widetilde{u}_{I,i} \frac{\partial \overline{\alpha}_g}{\partial x_i} = 0, \tag{4.5}$$

where $\widetilde{u}_{I,i}$ is the interface velocity field. From here onwards, subscripts 'g', 'p', 'd' and 'I' are used to indicate the gas phase, Lagrangian particle, Eulerian dispersed phase and interface quantity, respectively. As mentioned before, the governing system of equations for EE and EL formulations can be recovered by setting $\overline{\alpha}_p = 0$ and $\overline{\alpha}_d = 0$, respectively, in the general formulation presented below. Note that, typically for EL formulation for systems having low mass or volume loading, $\overline{\alpha}_g = 1$ is used.

4.1.1 Eulerian Gas Phase

Applying a box filter (appropriate for a finite-volume based implementation) to the system of transport equations yields the density-weighted filtered LES equations for the gas phase, which comprises of transport equations for mass, momentum, energy and species expressed as

$$\frac{\partial \overline{\alpha}_g \, \overline{\rho}_g}{\partial t} + \frac{\partial \overline{\alpha}_g \, \overline{\rho}_g \widetilde{u}_{g,i}}{\partial x_i} = \overline{\dot{\rho}}_D, \tag{4.6a}$$

$$\begin{aligned} \frac{\partial \overline{\alpha}_g \, \overline{\rho}_g \widetilde{u}_{g,i}}{\partial t} &+ \frac{\partial}{\partial x_j} \left[\overline{\alpha}_g \left(\overline{\rho}_g \widetilde{u}_{g,i} \widetilde{u}_{g,j} + \overline{p}_g \delta_{ij} + \tau^{sgs}_{g,ij} - \overline{\tau}_{g,ij} \right) \right] \\ &= \overline{p}_I \frac{\partial \overline{\alpha}_g}{\partial x_j} \delta_{ij} - \overline{\tau}_{I,ij} \frac{\partial \overline{\alpha}_g}{\partial x_j} + \overline{\dot{F}}_{D,i}, \end{aligned} \tag{4.6b}$$

$$\begin{aligned} \frac{\partial \overline{\alpha}_g \, \overline{\rho}_g \widetilde{E}_g}{\partial t} &+ \frac{\partial}{\partial x_j} \left[\overline{\alpha}_g \left(\overline{\rho}_g \widetilde{u}_{g,j} \widetilde{E}_g + \widetilde{u}_{g,j} \overline{p}_g + \overline{q}_{g,j} - \widetilde{u}_{g,i} \overline{\tau}_{g,ji} + H^{sgs}_{g,j} + \sigma^{sgs}_{g,j} \right) \right] \\ &= \overline{p}_I \widetilde{u}_{I,j} \frac{\partial \overline{\alpha}_g}{\partial x_j} - \widetilde{u}_{I,i} \overline{\tau}_{I,ij} \frac{\partial \overline{\alpha}_g}{\partial x_j} + \overline{\dot{Q}}_D + \overline{\dot{W}}_D, \end{aligned} \tag{4.6c}$$

$$\begin{aligned} \frac{\partial \overline{\alpha}_g \, \overline{\rho}_g \widetilde{Y}_{g,k}}{\partial t} &+ \frac{\partial}{\partial x_i} \left[\overline{\alpha}_g \left(\overline{\rho}_g (\widetilde{Y}_{g,k} \widetilde{u}_{g,i} + \widetilde{Y}_{g,k} \widetilde{V}_{g,i,k}) + Y^{sgs}_{g,i,k} + \theta^{sgs}_{g,i,k} \right) \right] \\ &= \overline{\alpha}_g \dot{\omega}_{g,k} + \overline{\dot{S}}_{D,k}, \quad \text{for} \quad k = 1, 2, \ldots, N_s, \end{aligned} \tag{4.6d}$$

where subscript 'D' denote the source term contribution from Lagrangian and Eulerian dispersed phases and N_s is the number of species. In Eq. (4.6) u_i is the velocity vector, p is the pressure, E is the total energy, Y_k is the mass fraction of the k^{th} species, τ_{ij} is the viscous stress tensor, q_i is the heat-flux vector and δ_{ij} is the Kronecker delta. The subgrid scale terms are denoted by superscript 'sgs' in Eq. (4.6) and they require closure approximation. These terms include subgrid stress tensor τ^{sgs}_{ij}, subgrid enthalpy flux H^{sgs}_i, subgrid viscous work σ^{sgs}_i, subgrid convective species flux $Y^{sgs}_{i,k}$ and subgrid diffusive species flux $\theta^{sgs}_{i,k}$. The closure models for these terms are discussed in sec. 4.3. The source terms $\overline{\dot{\rho}}_D$, $\overline{\dot{F}}_{D,i}$, $\overline{\dot{W}}_D$ and $\overline{\dot{S}}_{D,k}$, which appear in the transport equations for mass, momentum, energy

and species, respectively, represent the interphase exchange terms. They are obtained in terms of the source terms for Lagrangian and Eulerian dispersed phases through

$$\overline{\dot{\mathcal{F}}}_{D,m} = \overline{\dot{\mathcal{F}}}_{p,m} + \overline{\dot{\mathcal{F}}}_{d,m}, \tag{4.7}$$

where the vector $\boldsymbol{\mathcal{F}} = \left[\rho, \boldsymbol{F}^T, Q, W, \boldsymbol{S}^T\right]^T$ represents source term in different transport equations. Here, $\boldsymbol{F} = [F_1, F_2, \ldots, F_{\text{dim}}]^T$ and $\boldsymbol{S} = [S_1, S_2, \ldots, S_{N_s}]^T$, with 'dim' denoting the dimension of the considered flow system (2D/3D). Note that for mass transfer of single species, we obtain $\overline{\dot{S}}_D = \overline{\dot{\rho}}_D$. The contribution to source terms from the Lagrangian and Eulerian dispersed phases are provided in Eqs. (4.15) and (4.14), respectively.

By assuming a Newtonian fluid with the Stokes' hypothesis and the Fourier's law of thermal conduction, the filtered viscous stress tensor $\overline{\tau}_{g,ij}$ and the heat flux vector $\overline{q}_{g,j}$ can be approximated as

$$\overline{\tau}_{g,ij} = \mu_g \left(\frac{\partial \widetilde{u}_{g,i}}{\partial x_j} + \frac{\partial \widetilde{u}_{g,j}}{\partial x_i}\right) - \frac{2}{3}\mu_g \frac{\partial \widetilde{u}_{g,k}}{\partial x_k}\delta_{ij}, \tag{4.8a}$$

$$\overline{q}_{g,j} = -\kappa_g \frac{\partial \widetilde{T}_g}{\partial x_j} + \overline{\rho}\sum_1^{N_s} \widetilde{Y}_{g,k}\widetilde{h}_{g,k}\widetilde{V}_{g,j,k} + \sum_1^{N_s} q^{sgs}_{g,i,k}, \tag{4.8b}$$

where $\mu_g \equiv \mu_g(\widetilde{T}_g)$ is the dynamic viscosity of the gas, κ_g is the thermal conductivity of the gas, $\widetilde{h}_{g,k}$ is the resolved specific enthalpy of the k^{th} species, $q^{sgs}_{g,i,k}$ is the subgrid heat flux vector (described in sec. 4.3) and $\widetilde{V}_{g,j,k}$ is the resolved species diffusion velocities that can be modeled through a Fickian diffusion approximation through

$$\widetilde{V}_{g,j,k} = -\frac{D_{g,k}}{\widetilde{Y}_{g,k}}\frac{\partial \widetilde{Y}_{g,k}}{\partial x_j}. \tag{4.9}$$

Here, $D_{g,k}$ denotes diffusion coefficient of the k^{th} species and it can be obtained from a constant Lewis number (Le) assumption.

4.1.2 Lagrangian Particle Phase

The Lagrangian equations for the motion of a single particle within dense spray combustors are obtained with the assumption that the particle density is much greater than the carrier (gas) phase density ($\rho_p/\rho_g \approx 10^3$) and particle diameter is smaller than the Kolmogorov length scale. These equations are given by

$$\frac{dx_{p,i}}{dt} = u_{p,i}, \tag{4.10a}$$

$$\frac{dm_p}{dt} = -\dot{m}_p = -\frac{d}{dt}\left(\frac{4}{3}\pi r_p^3 \rho_p\right), \tag{4.10b}$$

$$m_p\frac{du_{p,i}}{dt} = \frac{\pi}{2}{r_p}^2 C_D \overline{\rho}_g |\widetilde{u}_{g,i} + u''_{g,i} - u_{p,i}|\left(\widetilde{u}_{g,i} + u''_{g,i} - u_{p,i}\right) - \frac{4}{3}\pi {r_p}^3 \frac{\partial \overline{p}_g}{\partial x_i} + m_p A_{c,i}, \tag{4.10c}$$

$$m_p C_p \frac{dT_p}{dt} = 2\pi r_p \kappa_g Nu\left(\widetilde{T}_g - T_p\right) - \dot{m}_p L_v, \tag{4.10d}$$

where x_i, m, r, T denote position vector, mass, radius and temperature, respectively. Some of the other terms in Eq. (4.10) include the drag coefficient C_D, acceleration due to inter-particle interactions $A_{c,i}$, the heat capacity C_p, the thermal conductivity of the gas phase κ_g, the Nusselt number Nu and the latent heat of vaporization L_v. The Nusselt number and the drag coefficient are typically expressed as empirical functions of Reynolds number (Re), Prandtl number (Pr), Mach number (M) and volume fraction α_g [47, 48, 49]. The closures for interface quantities can be found elsewhere [47, 48, 50]. The acceleration due inter-particle interactions, $A_{c,i}$, is computed as

$$A_{c,i} = -\frac{1}{\alpha_p \rho_p} \frac{\partial \tau}{\partial x_i}, \tag{4.11}$$

where τ is the inter-granular stress given by

$$\tau = \frac{P_s {\alpha_p}^{\beta}}{\alpha_{cs} - \alpha_p}, \tag{4.12}$$

with α_{cs} being the close packing volume fraction. Also, P_s and β are empirical constants, which are closed based on the nature of the flow being considered [51, 48, 50, 47].

In Eq. (4.10)(c), the sum $(\widetilde{u}_{g,i} + u''_{g,i})$ represents instantaneous $(u_{g,i})$ gas-phase velocity components, consisting of both the LES resolved velocity $\widetilde{u}_{g,i}$ and the unresolved fluctuating velocity $u''_{g,i}$, which can be reconstructed by employing a stochastic model [52, 23, 34]. For example, the unresolved velocity field can be obtained from the subgrid-scale turbulent kinetic energy at intervals coincident with the local characteristic eddy lifetime [52] or it can be based on a stochastic Markovian model [53]. In several other numerical implementations in the past, this term has been ignored, however, as mentioned in [23], in poorly resolved regions of the flow, where the subgrid-scale turbulent kinetic energy is more than 30% of the resolved turbulent kinetic energy, the effect of unresolved velocity fluctuations on the particle motion becomes important. In a similar way, the gas phase temperature at the particle location in Eq. (4.10)(d), ideally should include the unresolved temperature fluctuation, which in turn can be modeled through stochastic means [34], however, in the present formulation, we have ignored such contribution.

4.1.3 Eulerian Particle Phase

In the limit of a dense mass or volume loading, the dispersed phase can be modeled as a continuum fluid. In such cases, the governing equations for the dispersed phase can be

expressed in the Eulerian framework and are given by

$$\frac{\partial \overline{\alpha}_d\, \overline{\rho}_d}{\partial t} + \frac{\partial \overline{\alpha}_d\, \overline{\rho}_d \widetilde{u}_{d,i}}{\partial x_i} = -\overline{\dot{\rho}}_d, \tag{4.13a}$$

$$\begin{aligned}\frac{\partial \overline{\alpha}_d\, \overline{\rho}_d \widetilde{u}_{d,i}}{\partial t} &+ \frac{\partial}{\partial x_j}\left[\overline{\alpha}_d\left(\overline{\rho}_d \widetilde{u}_{d,i}\widetilde{u}_{d,j} + \overline{p}_d\delta_{ij} + \tau^{sgs}_{d,ij} - \overline{\tau}_{d,ij}\right)\right] \\ &= \overline{p}_I \frac{\partial \overline{\alpha}_d}{\partial x_j}\delta_{ij} - \overline{\tau}_{I,ij}\frac{\partial \overline{\alpha}_d}{\partial x_j} - \overline{\dot{F}}_{d,i},\end{aligned} \tag{4.13b}$$

$$\begin{aligned}\frac{\partial \overline{\alpha}_d\, \overline{\rho}_d \widetilde{E}_d}{\partial t} &+ \frac{\partial}{\partial x_j}\left[\overline{\alpha}_d\left(\overline{\rho}_d \widetilde{u}_{d,j}\widetilde{E}_d + \widetilde{u}_{d,j}\overline{p}_d + \overline{q}_{d,j} - \widetilde{u}_{d,i}\overline{\tau}_{d,ji} + H^{sgs}_{d,j} + \sigma^{sgs}_{d,j}\right)\right] \\ &= \overline{p}_I \widetilde{u}_{I,j}\frac{\partial \overline{\alpha}_d}{\partial x_j} - \widetilde{u}_{I,i}\overline{\tau}_{I,ij}\frac{\partial \overline{\alpha}_d}{\partial x_j} - \overline{\dot{Q}}_d - \overline{\dot{W}}_d,\end{aligned} \tag{4.13c}$$

with the source terms in the above equations given by

$$\overline{\dot{\rho}}_d = N_d \dot{m}_d = N_d \frac{d}{dt}\left(\frac{4}{3}\pi r_d^3 \overline{\rho}_d\right), \tag{4.14a}$$

$$\overline{\dot{F}}_{d,i} = N_d\left[\dot{m}_d u_{d,i} + \frac{\pi}{2} r_d^2 C_D \overline{\rho}_g |\tilde{u}_{d,i} - \tilde{u}_{g,i}|\left(\tilde{u}_{d,i} - \tilde{u}_{g,i}\right) + \frac{4}{3}\pi r_d^3 \frac{\partial \overline{p}_g}{\partial x_i}\right], \tag{4.14b}$$

$$\overline{\dot{Q}}_d = N_d\left[\dot{m}_d h_v + 2\pi r_d \kappa_g Nu\left(\widetilde{T}_d - \widetilde{T}_g\right)\right], \tag{4.14c}$$

$$\overline{\dot{W}}_d = N_d\left[\dot{m}_d \tilde{u}_{d,i}\tilde{u}_{d,i} + \frac{\pi}{2} r_d^2 C_D \rho_g |\tilde{u}_{d,i} - \tilde{u}_{g,i}|\left(\tilde{u}_{d,i} - \tilde{u}_{g,i}\right)\tilde{u}_{d,i} + \frac{4}{3}\pi r_d^3 \frac{\partial \overline{p}_g}{\partial x_i} u_{d,i}\right], \tag{4.14d}$$

where N_d is the number density of the Eulerian dispersed phase.

The source terms from the Lagrangian and Eulerian dispersed phases provided through Eqs. (4.15) and (4.14) can be combined through Eq. (4.7) to yield source terms for the gas phase. The governing system of equations given by Eqs. (4.6), (4.10) and (4.13), for the gas phase, Lagrangian disperse phase and Eulerian disperse phase, respectively are complete once the subgrid-scale models are specified, which are briefly described in the next section.

4.2 Coupling Between the Phases

As shown in Eq. (4.7), the source term needed for the gas phase transport equations given by Eq. (4.6) comprises of source terms corresponding to the Lagrangian and Eulerian dispersed phases. The source term contribution from the Lagrangian dispersed phase are obtained

through

$$\overline{\dot{\rho}}_p = \frac{1}{\Delta V}\sum_{n=1}^{N} n_{p,n}\dot{m}_{p,n}, \tag{4.15a}$$

$$\overline{\dot{F}}_{p,i} = \frac{1}{\Delta V}\sum_{n=1}^{N} n_{p,n}\left[\dot{m}_{p,n}u_{p,i,n} + \frac{4}{3}\pi r_{p,n}^3\frac{\partial \overline{p}_{g,n}}{\partial x_i}\right. \tag{4.15b}$$

$$\left. + \frac{\pi}{2}r_{p,n}^2 C_{D,n}\overline{\rho}_{g,n}|u_{p,i,n} - \tilde{u}_{g,i,n} - u''_{g,i,n}|\left(u_{p,i,n} - \tilde{u}_{g,i,n} - u''_{g,i,n}\right)\right], \tag{4.15c}$$

$$\overline{\dot{Q}}_p = \frac{1}{\Delta V}\sum_{n=1}^{N} n_{p,n}\left[\dot{m}_{p,n}h_{v,n} + 2\pi r_{p,n}\kappa_g N u_n\left(T_{p,n} - \tilde{T}_{g,n}\right)\right], \tag{4.15d}$$

$$\overline{\dot{W}}_p = \frac{1}{\Delta V}\sum_{n=1}^{N} n_{p,n}\left[\dot{m}_{p,n}u_{p,i,n}u_{p,i,n} + \frac{4}{3}\pi r_{p,n}^3\frac{\partial \overline{p}_{g,n}}{\partial x_i}u_{p,i,n}\right. \tag{4.15e}$$

$$\left. + \frac{\pi}{2}r_{p,n}^2 C_{D,n}\rho_{g,n}|u_{p,i,n} - \tilde{u}_{g,i,n} - u''_{g,i,n}|\left(u_{p,i,n} - \tilde{u}_{g,i,n} - u''_{g,i,n}\right)u_{p,i,n}\right], \tag{4.15f}$$

where h_v is the enthalpy change associated with the mass transfer.

4.3 Subgrid Terms and Closure

The density-weighted filtering of the governing equations leads to appearance of unclosed terms, also referred to as the subgrid-scale terms, which require further closure approximations to obtain a closed system of equations. As mentioned before, these terms include the subgrid stress tensor $\tau_{g,ij}^{sgs}$, subgrid enthalpy flux $H_{g,i}^{sgs}$, subgrid viscous work $\sigma_{g,i}^{sgs}$, subgrid convective species flux $Y_{g,i,k}^{sgs}$, subgrid diffusive species flux $\theta_{g,i,k}^{sgs}$ and the subgrid heat flux $q_{g,i,k}^{sgs}$ [54, 55]. Some of these terms can be closed using the models developed for non-reacting or reacting gas phase problems. Here, we briefly describe some well known models that are used for closure of subgrid-scale terms.

The subgrid stress and heat flux terms are typically closed following the Boussinesq approximation, where an eddy viscosity type gradient closure is employed. Such type of closure is very popular and a model is required for the eddy viscosity. Both algebraic/dynamic Smagorinsky (ASM/DSM) model [56, 57] and the model for subgrid kinetic energy [58, 59] are very popular. For example, when using the subgrid kinetic energy k^{sgs} closure, a transport equation for k^{sgs} needs to be solved, which is given by

$$\frac{\partial}{\partial t}\overline{\alpha}_g\,\overline{\rho}_g\,k^{sgs} + \frac{\partial}{\partial x_i}\left(\overline{\alpha}_g\,\overline{\rho}_g\,\widetilde{u}_{g,i}k^{sgs}\right) = \overline{\alpha}_g P_{k^{sgs}} + \frac{\partial}{\partial x_i}\left(\overline{\alpha}_g\overline{\rho}_g\nu_t\frac{\partial k^{sgs}}{\partial x_i}\right) - \overline{\alpha}_g D_{k^{sgs}} + \overline{\dot{F}}_{D,k}^{sgs}. \tag{4.16}$$

Here, $P_{k^{sgs}}$ and $D_{k^{sgs}}$ denote respectively, the production and dissipation of k^{sgs}, which can be obtained through

$$P_{k^{sgs}} = -\tau_{g,ij}^{sgs}\frac{\partial \widetilde{u}_{g,i}}{\partial x_j}, \qquad D_{k^{sgs}} = C_\epsilon\overline{\rho}_g\frac{(k^{sgs})^{1.5}}{\Delta}, \tag{4.17}$$

where ν_t is the subgrid eddy viscosity, and is modeled as $\nu_t = C_\nu \sqrt{k^{sgs}}\Delta$, where Δ is the local filter width. The constants C_ν and C_ϵ are obtained theoretically as 0.067 and 0.916, respectively [54] but can be computed using a dynamic procedure, referred to as the locally dynamic kinetic energy model (LDKM) [60, 55] that can be used locally without requiring any *ad hoc* averaging. With the eddy viscosity model, the subgrid stress tensor $\tau^{sgs}_{g,ij}$ is closed through

$$\tau^{sgs}_{g,ij} = -2\overline{\rho}_g \nu_t \left(S_{g,ij} - \frac{1}{3} S_{g,kk}\delta_{ij} \right) + \frac{2}{3}\overline{\rho}_g k^{sgs}\delta_{ij}, \tag{4.18}$$

where $S_{g,ij}$ is the rate of strain tensor given by

$$S_{g,ij} = \frac{1}{2}\left(\frac{\partial \widetilde{u}_{g,i}}{\partial x_j} + \frac{\partial \widetilde{u}_{g,j}}{\partial x_i} \right). \tag{4.19}$$

In Eq. (4.16) $\overline{\dot{F}}^{sgs}_{D,i}$ is the source term due to the Lagrangian and Eulerian dispersed phases that can be closed exactly [61, 62].

The subgrid total enthalpy, $H^{sgs}_{g,j}$, can also modeled using the eddy viscosity and gradient diffusion assumption through

$$H^{sgs}_{g,i} = -\overline{\rho}_g \frac{\nu_t}{Pr_t} \frac{\partial \widetilde{H}_g}{\partial x_i}, \tag{4.20}$$

where $\widetilde{H}_g$ is the filtered total enthalpy, given by $\widetilde{H}_g = \widetilde{h}_g + \frac{1}{2}\widetilde{u}_{g,i}\widetilde{u}_{g,i} + k^{sgs}$, where $\widetilde{h}_g = \sum_{k=1}^{N_s} \widetilde{h}_{g,k}\widetilde{Y}_{g,k}$. The turbulent Prandtl number Pr_t can be dynamically computed, but is typically assumed to be unity. In a similar manner, the subgrid convective species flux, $Y^{sgs}_{g,i,k}$, is modeled using the gradient diffusion assumption through

$$Y^{sgs}_{g,i,k} = -\frac{\overline{\rho}_g \nu_t}{Sc_t} \frac{\partial \widetilde{Y}_{g,k}}{\partial x_i}, \tag{4.21}$$

where Sc_t is the turbulent Schmidt number. It can also be dynamically computed; however, it is typically assumed to be unity in many studies.

The other subgrid terms, i.e., $\theta^{sgs}_{g,i,k}$ and $q^{sgs}_{g,i,k}$ are neglected in most studies [54, 63]. Note that in the Eq. (4.18)-(4.21), the subscript 'g' can be replaced with 'd' to obtain appropriate closures under the assumption that the Eulerian dispersed phase behaves as a pseudo gas phase. The so-called pseudo-fluid assumption is not very easy to justify and therefore, the closures for dispersed phase especially, in the context of dense flows is unknown.

A closure model for the reaction rate is also required for the combustion problem. Subgrid turbulence-chemistry interaction models have remained a challenging task even for gas phase combustion and these problems are made even more challenging when spray evaporation, mixing and combustion have to be included. Due to the discrete nature of the particles vaporizing and mixing is local and therefore, combustion can occur in multitude of manner ranging from non-premixed to fully premixed type. Partially premixing is the norm in spray combustion system and therefore, subgrid closures for turbulence-chemistry interaction need to address the complete regime. At this time there are not that many options for this goal.

4.4 Hybrid Solver transition

As two solvers for the simulation of dispersed phase are available in LESLIE, a hybrid approach has been developed as follows: the dense phase is simulated using the Eulerian particle phase approach, while the diluted phase is simulated using the Lagrangian phase.

The computations using Eulerian particle phase are fast and are accurate for dense to marginally dense flows. Lagrangian particle results are accurate over a wide range of dispersed phase volume fractions and particle size distributions and this technique can easily handle polydisperse flows. Moreover, as every particle can be tracked accurately and efficiently, the combustion and evaporation of Lagrangian particles can be studied more easily. The Lagrangian solver with dense correction can also be used for heavily loaded particle flows, but it can be very expensive when the number of particles increases. In order to take advantage of both methods, a hybrid method has been developed. It uses the Eulerian approach in dense regions where the liquid volume fraction is high, and Lagrangian approach when the loading is much lower. The technique to transfer information from the Eulerian dispersed phase to Lagrangian phase is determined by three parameters, namely, the transfer volume fraction α_T, the transfer fraction f_T , and the number of particles per parcel, Pp . The transfer volume fraction is the threshold value to switch from the Eulerian solver to the Lagrangian one ($\alpha \leq \alpha_T$). It indicates the region where the transition from EE to EL is desired. If this parameter is very low, the solver remains purely Eulerian and no Lagrangian particles are created. On the other hand, if $alpha_T$ is set to a relatively high value, all the Eulerian particles are transferred into the Lagrangian solver. It needs to be between 0 and 1. The choice of this parameter can be tricky, however, it depends on the computational cost and the required accuracy.

The transfer fraction is the fraction of particles in a computational cell transferred from Eulerian dispersed phase to Lagrangian dispersed phase. When the particles are added to the Lagrangian dispersed phase, the volume fraction of the Lagrangian dispersed phase, α_p, is incremented based on the number of particles added. The number of particles added to the Lagrangian dispersed phase is given as: $N_p = \frac{3\alpha_d f_T Vol}{4\pi P_p r_p^3}$. As the particles are removed from the Eulerian dispersed phase, the Eulerian liquid volume fraction is recomputed to conserve mass.

The mass, the momentum, the energy, the velocity, the temperature, the radius and the position of each particle transferred to the Lagrangian dispersed phase are set based on the values from the Eulerian dispersed phase in a given computational cell. If $f_T = 1$, then all the particles in a computational cell are transferred and if $f_T = 0$ no particle is transferred. A value between 0 and 1 is chosen to ensure stability instead of transferring all the particles.

CHAPTER V

RESULTS AND DISCUSSIONS

5.1 Validation

5.1.1 Sedov test cases

To assess the capability of the code to accurately solve blast waves, a first set of simulations has been performed and compared to the Sedov analytical solutions. These simulations assume a point explosion with a pressure field of 10^{-5} Pa. A high pressure blob is initialized at the center of the domain with a 1000 Pa value in a 5 mm radius disk. The density is equal to 1 kg/m^3 everywhere. Outflow conditions are imposed at the boundaries to avoid reflections. The simulated physical time is 100 ms. The evolution of the pressure peak and shock radius is compared on three different uniform grids (256 x 256, 512 x 512, 1024 x 1024), and in 3 dimensions, inside a 3D sector on three different meshes (250 x 45 x 45, 500 x 45 x 45, 1000 x 45 x 45), where the two angles ϕ and θ are 45 degrees.

The evolution of the shock radius and the pressure peak is presented in Fig. 5.1. The comparison is done using all the uniform meshes presented in this section with an additional simulation computed using AMR (Adaptative Refinement Method) around the shock. An empirical law is compared to these profiles. Results give good agreements for both the shock radius and the pressure peak evolution.

The quantitative comparison is provided in Fig. 5.2, comparing the Shock radius and the pressure peak evolution with time. These profiles are compared to an extra simulation using AMR around the shock radius, and an empirical law from Sedov derivations. From this study, a very good agreement is found.

5.1.2 Boiko test case

In this test, the EL solver is validated by simulating the interaction of a marginally dense particle cloud with a shock wave. The setup for this test is based on the experiments performed by Boiko et al. [1]. A shock tube of length 6.5 m and cross section 52 mm $\times$ 52 mm was used in the experiment and an acrylic plastic particle cloud of initial volume fraction 3.0% was impacted by a Mach 2.8 shock. The radius of each particle is 150 μm and the density is 1200 kg/m^3. For simulation, a domain with dimensions same as that of the shock tube is considered and is resolved using as grid of size 1250 $\times$ 10. The particle cloud is placed at a location 2 m from the high pressure end of shock tube. The initial width of the particle cloud is 13 mm and the cloud has 74600 particles. The driver section is filled with He and is initialized with high pressure p_4 obtained from Eqn. (5.1) such that a Mach 2.8 shock interacts with the particle cloud. The driven section is filled with air at 10^5 Pa. The driven section, the driver section and the particle cloud are initially at 298K. All boundaries of the shock tube are set to be no-flux boundaries except the outflow where

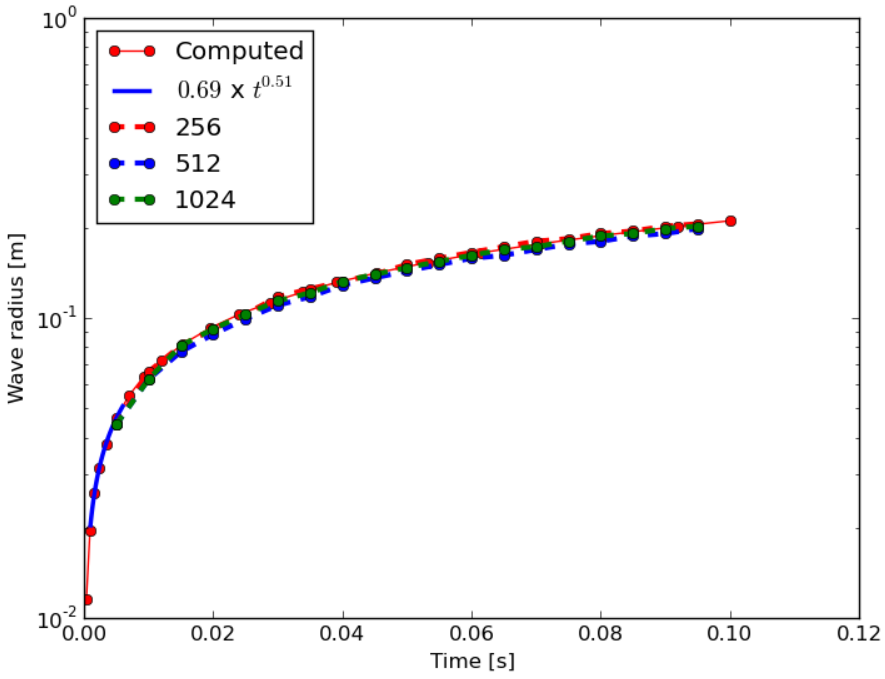

(a) Shock Radius

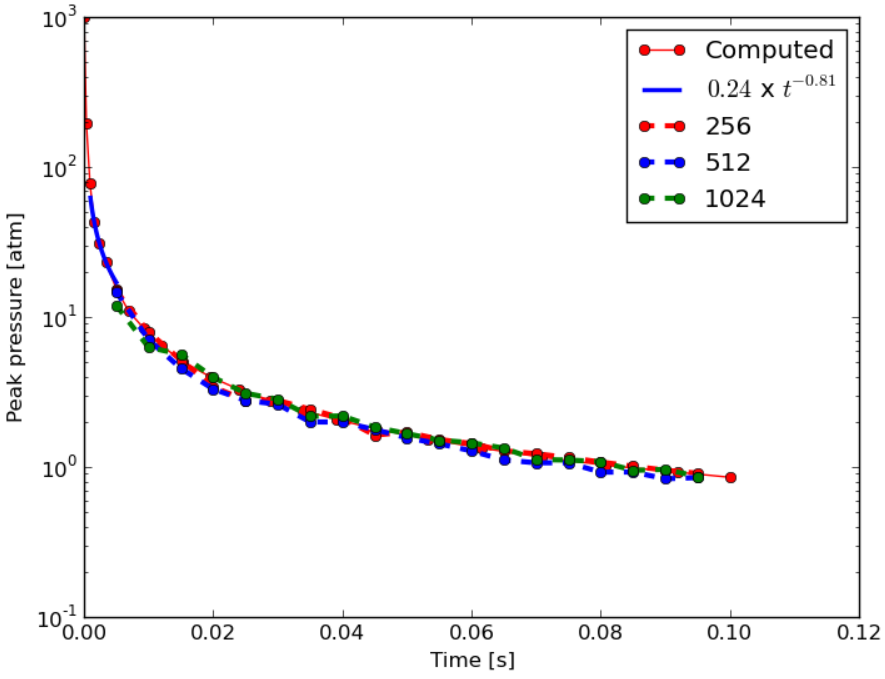

(b) Pressure peak evolution

Figure 5.1: Shock radius and pressure peak evolution with time for 2D simulations: all cases are compared with empirical law and an extra simulation done using Adaptative Refinement method

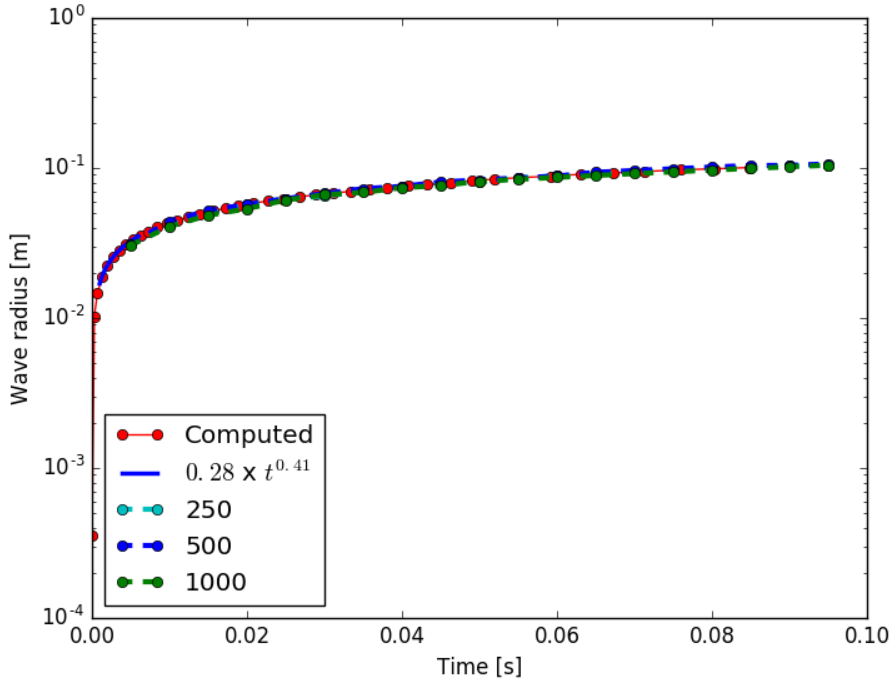

(a) Shock Radius

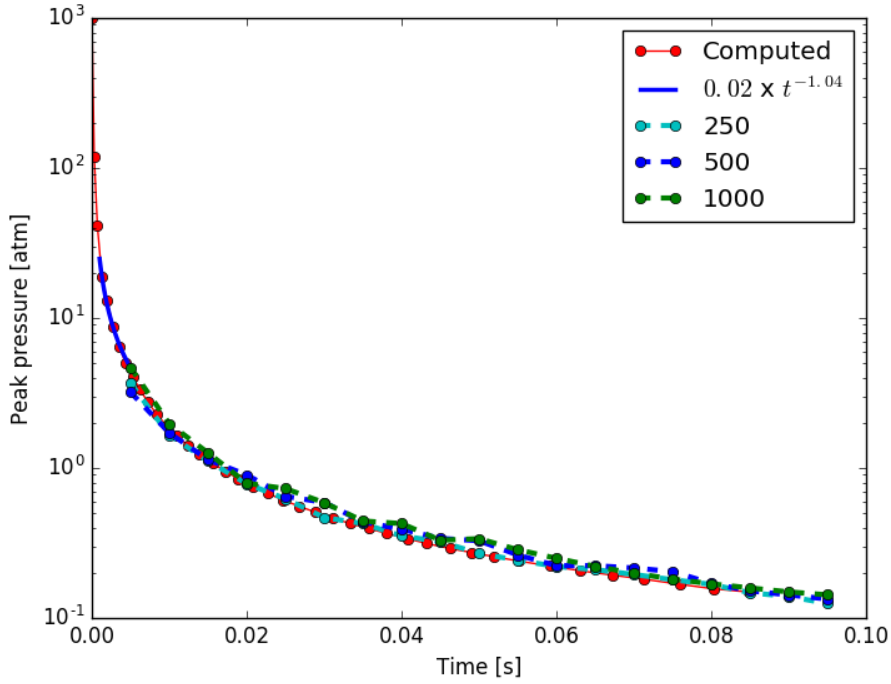

(b) Pressure peak evolution

Figure 5.2: Shock radius and pressure peak evolution with time for 3D simulations: all cases are compared with empirical law and an extra simulation done using Adaptative Refinement method

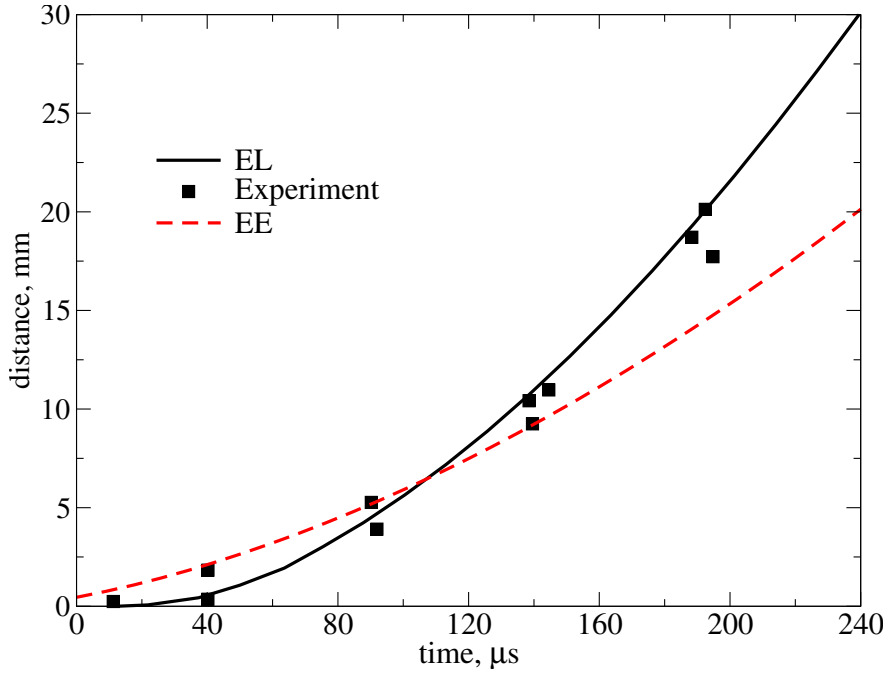

Figure 5.3: Dispersion of particle cloud by a shock wave. The experimental data is from [1]

the flow properties are extrapolated. The acceleration of the particle is computed using the drag law provided by Boiko et al. [1].

$$\frac{p_4}{p_1} = \frac{2\gamma_1 M_1^2 - (\gamma_1 - 1)}{\gamma_1 + 1} \left[1 - \frac{(\gamma_4 - 1)}{(\gamma_1 + 1)} \frac{a_1}{a_4} \left(M_1 - \frac{1}{M_1} \right) \right]^{\frac{-2\gamma_4}{\gamma_4 - 1}}, \tag{5.1}$$

The dispersion of the particle cloud after interaction with the shock wave is shown in Fig. 5.3. Here, unlike the single particle dispersion case, DEM is turned on and hence the gas-phase fluxes are influenced by the volume of the particles in the flow. The case shows the accuracy of the solver in simulating the particle dispersion for marginally dense clouds.

The Boiko test is repeated with EE method using a grid with resolution, $\Delta = 250.0$ μm and the variation of the location of the particle cloud with time is compared with the results from EL method. While EL method accurately captures the particle cloud motion, EE method shows an agreement in initial stages of the cloud dispersal. As the volume fraction of the particle cloud decrease from 0.03 to below the dilute limit (i.e. 0.01), the error in the particle cloud location obtained using EE scheme increases from 1.5 % to 33.0 %. Since, the particle cloud location is dependent on the accurate estimation of the cloud extremities, the error with EE increases in this case. Note that the dilute dispersion with EE is not as accurate as EL as EL accounts for the motion of each particle and accurately determines the particle cloud edges.

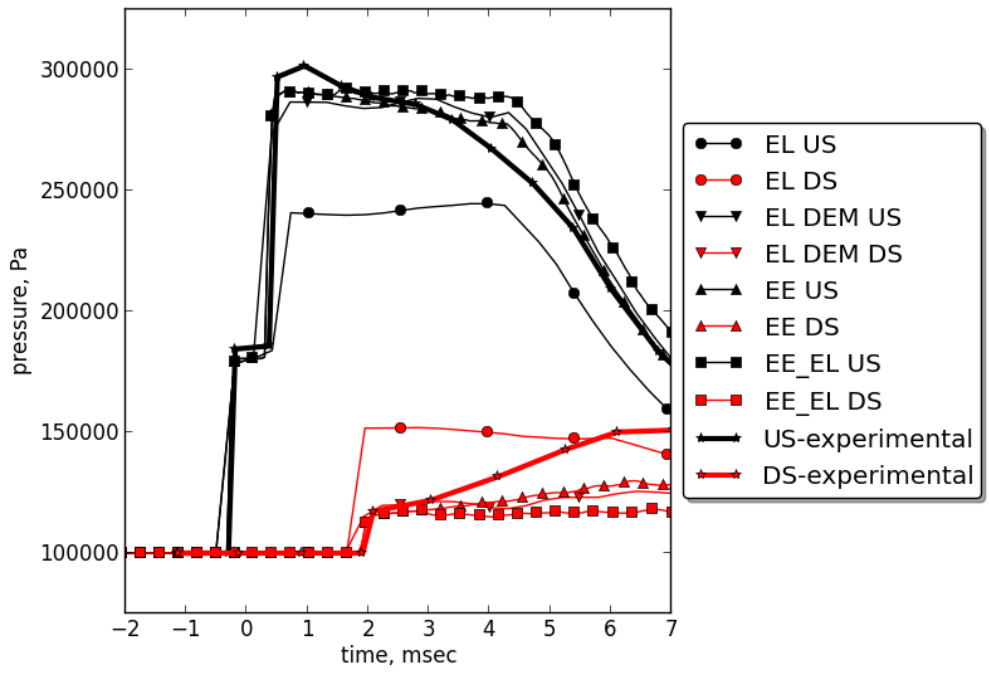

Figure 5.4: Comparision of pressures upstream (US) and downstream (DS) of a dense particle cloud. The experimental data is from [2]. The results with EE, EL and EE-EL are shown. Also, EL case without DEM is shown.

5.1.3 Rouge test case

The propagation of a shock wave through a dense particle cloud is simulated using both EE and EL methods to validate both the methods and investigate the importance of the gas-phase flux correction based on the particle volume fraction. The setup for this test is based on the experimental configuration described by Rouge et al. [2]. A vertical shock tube of length 6 m and cross section 13 cm $\times$ 13 cm has been employed in the experimental investigations. Glass particles of radius 750.0 μm are placed in the shock tube and are initially supported by a membrane. A Mach 1.3 shock is allowed to interact with the particles which initially form a bed of thickness 2 cm and volume fraction 65%. For these simulations, the geometry of the domain is set to be same as the experimental configuration and is resolved using a grid of size $600 \times 13 \times 13$. In order to perform simulations using EL solver, 15540 computational particles, i.e., parcels, are initialized with 8 particles per parcel. The shock tube is filled with air and the pressure in the driver section is set based on Eqn. (5.1). The pressure in the driven section is 10^5 Pa, initially. The initial temperature of the particles and the gas is at 298 K. The velocity of the particles is computed based on the quasi-steady drag relation described by Crowe et al. [64]. All walls of the shock tube are set to be no-flux boundaries except the outflow (the end away from the high pressure driver section) where the flow properties are extrapolated.

The pressure at locations 11 cm below the particle bed and 72 cm above the particle bed are recorded and compared with the experimental results. As the shock interacts with the dense particle bed, a transmitted shock propagates through the particle cloud and a reflected shock wave propagates upstream. In order to capture the pressure accurately, the gas-phase flux correction based on the volume fraction of the dispersed phase is very important. This is demonstrated in Fig. 5.4. In the case without DEM, the upstream pressure is under predicted and the downstream pressure is over predicted. Also, the downstream shock wave propagates through the particle cloud at relatively greater speed and reaches the upstream pressure trace point nearly 0.4 ms earlier. Thus, DEM is important to predict the gas-phase and the dispersed phase properties and its significance is increased with increase in the dispersed phase volume fraction.

For this test, the numerical simulations are performed using both EE and EL methods. The cases with EE are performed with and without the contribution from granular friction (p_f) and granular viscous dissipation terms ($\dot{\gamma}$ and ϕ). Figure 5.4 shows that the effect of friction and the granular viscous terms is not significant. Both EE and EL methods produce similar results and are in good agreement with the experimental results. The results with the combined EE-EL method, where the dispersed phase is transitioned from EE method to EL method if the Eulerian dispersed phase volume fraction reaches 0.01, are also in good agreement with the results from the experiment and the simulations using pure EE and pure EL methods.

5.2 Blast Wave in Room with Vent

5.2.1 Simulation setup

In this study, we simulate the propagation of a blast wave from a spherical charge in an enclosure with a vent. The explosive is initially set in the middle of the enclosure. A two-dimensional representation of the setup is simulated. The case is initialized with detonation wave profiles for the pressure, velocity, density, and temperature which are obtained using the Gas-Interpolated-Solid Stewart-Prasad-Asay (GISPA) method for the condensed phase detonation process. The energetic material in consideration is TNT and the charge is 11.63 cm in diameters. The room measures 20 charge diameters in length, 16 diameters in height, and the vent has a width of 2 diameters located in the center of the ceiling (top boundary), as shown in the schematic diagram in figure 5.5(a). The simulation captures the pressure front and subsequent reflections from the walls. These develop locations with wave focusing where pressure spikes can be observed. The simulation makes use of adaptive mesh refinement (AMR) to better resolve the thin blast front.

5.2.2 Results and discussions

Figure 5.6 plots the time evolution of the pressure at the location of the probes as described in 5.5(b). Figures 5.6 a, b, and c compare corresponding probes mirrored with a line crossing horizontally in the center of the domain. Up until 0.4ms, the probes show excellent agreement demonstrating a symmetry in the flow behavior. This is expected, since at this stage, the expanding blast wave is symmetric, and has yet to reach the vent, which is the source of

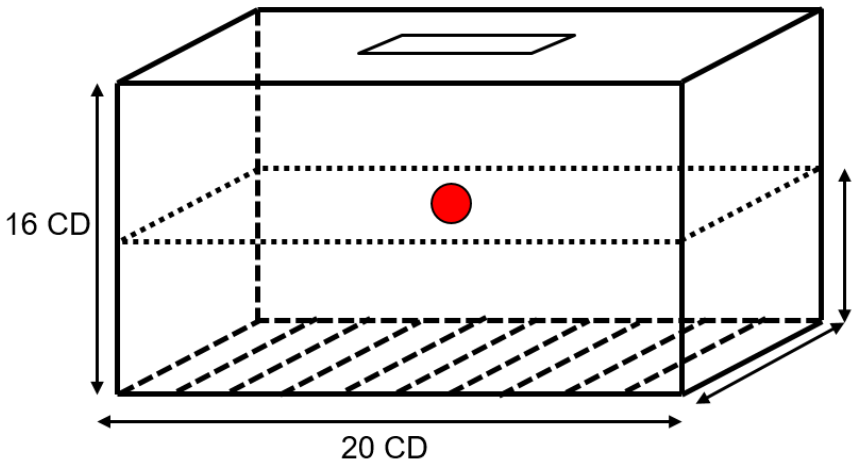

(a) Schematic diagram

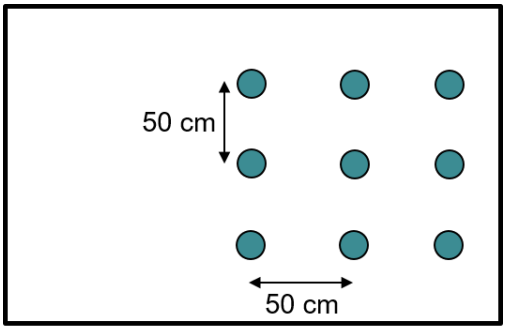

(b) Probes

Figure 5.5: Schematic diagram of domain and location of sensors.

asymmetry in the geometry. The three sensor show a similar behavior in the number of peaks depicting the wave front passage and subsequent reflections. Figure 5.6 d compares the pressure traces along the vertical centerline. The plot depicts an interesting pressure focusing in the center of the domain with higher peaks than its surrounding.

The propagation of the blast wave undergoes multiple characteristics that can be split here into three stages. The first stage can be seen as the outward propagation of the blast wave from the center charge. The blast wave maintains the initial spherical shape, which is imprinted from the initial charge shape. This can be seen in parts a and b of figures 5.7 and 5.8. The second stage appears as the waves get reflected from the walls. The wave reaches the top and bottom walls at the center and a pressure peak propagates along the walls. The reflected waves then coalesce at the corners propagating inwards. The propagation now takes the imprinted shape of the enclosure. The rectangular shape can be most clearly seen in part d of figures 5.7 and 5.8. However, the rectangular shape is not complete, particularly at the top part, where the vent imprint is noticeable. The vent allows pressure relief and thus, a delay in the wave propagation in this region is observed. The third stage, seen in parts e and f of figures 5.7 and 5.8 show a merging of the reflected waves that are now propagating back towards the walls. This wave propagation continues while the waves strength reduces as shows in the time traces in figure 5.6.

5.3 Blast wave in a Room Configuration

5.3.1 Simulation Setup

In this case, the computational domain is a rectangular shape single room which measures 3[m] in width and depth, and 1[m] in height. The imposed boundary condition is slip walls everywhere. The charge is cylindrical in shape, measuring 0.02286[m] radius and 0.2286[m] length, and placed at the center of computational domain. Two different methods of blast wave initialization are applied to the simulation in order to validate them. The first method is a full burnt simulation, which imports one-dimensional detonation profiles. Thus, the physical quantities, such as pressure, temperature, etc, are not distributed in the axial direction of charge. On the other hand, the second method, uses a center burn initialization where the detonation propagates from the center to the extremities of charge. This case is expected more faithfully represent the real life burning compared to the full burnt case. For full burnt case, the charge is composed by TNT, while HMX is used for center burnt case.

To measure the influence of Particles, the same computational grid is utilized. The size of explosive charge is kept the same, and HMX with center burnt initialization is applied. The particles are initially placed at charge, and propagates into the room driven by the blast wave. The parameters used for particle initialization is shown in Table 5.1.

5.3.2 Results and Discussion

At first, the grid resolution is investigated to guarantee the accuracy of resolution. The coarse, middle, and fine grid which respectively has about 20, 40, and 80 nodes are used for this verification. The center burnt case is used for initialization. The pressure history at three different locations are shown in Figure 5.9. The coarse grid shows a small deviation

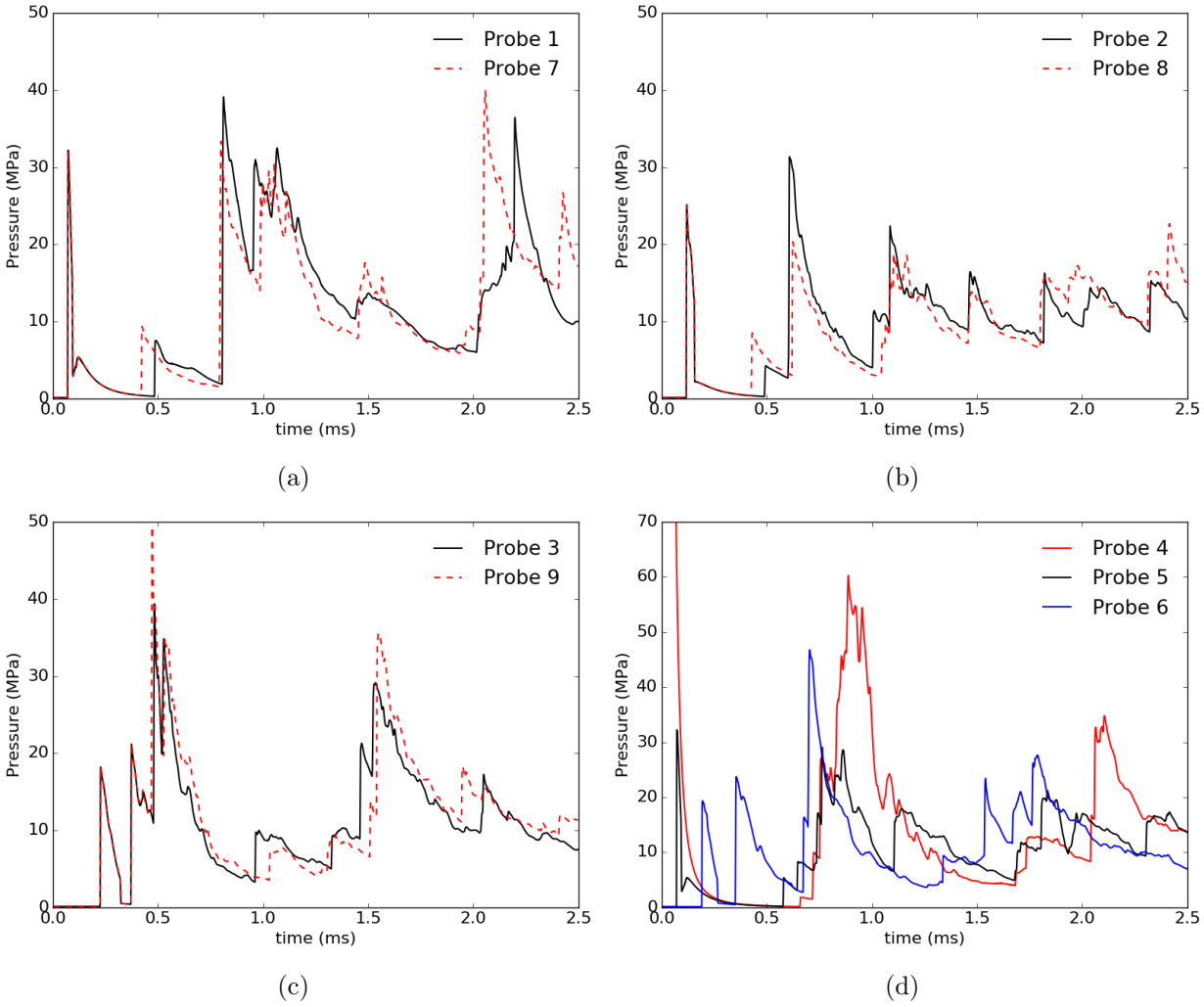

Figure 5.6: Time evolution of pressure at the different locations.

Table 5.1: Initial setup for particles.

Case	Number of Particles	Radius [μm]	Number of particles per parcel	Volume fraction
A	0	-	-	-
B	100,000	2.0	1	8.93e-2
C	100,000	20.0	1	8.893e-6
D	100,000,000	2.0	1	8.93e-6
E	100,000,000	20.0	1	8.93e-3

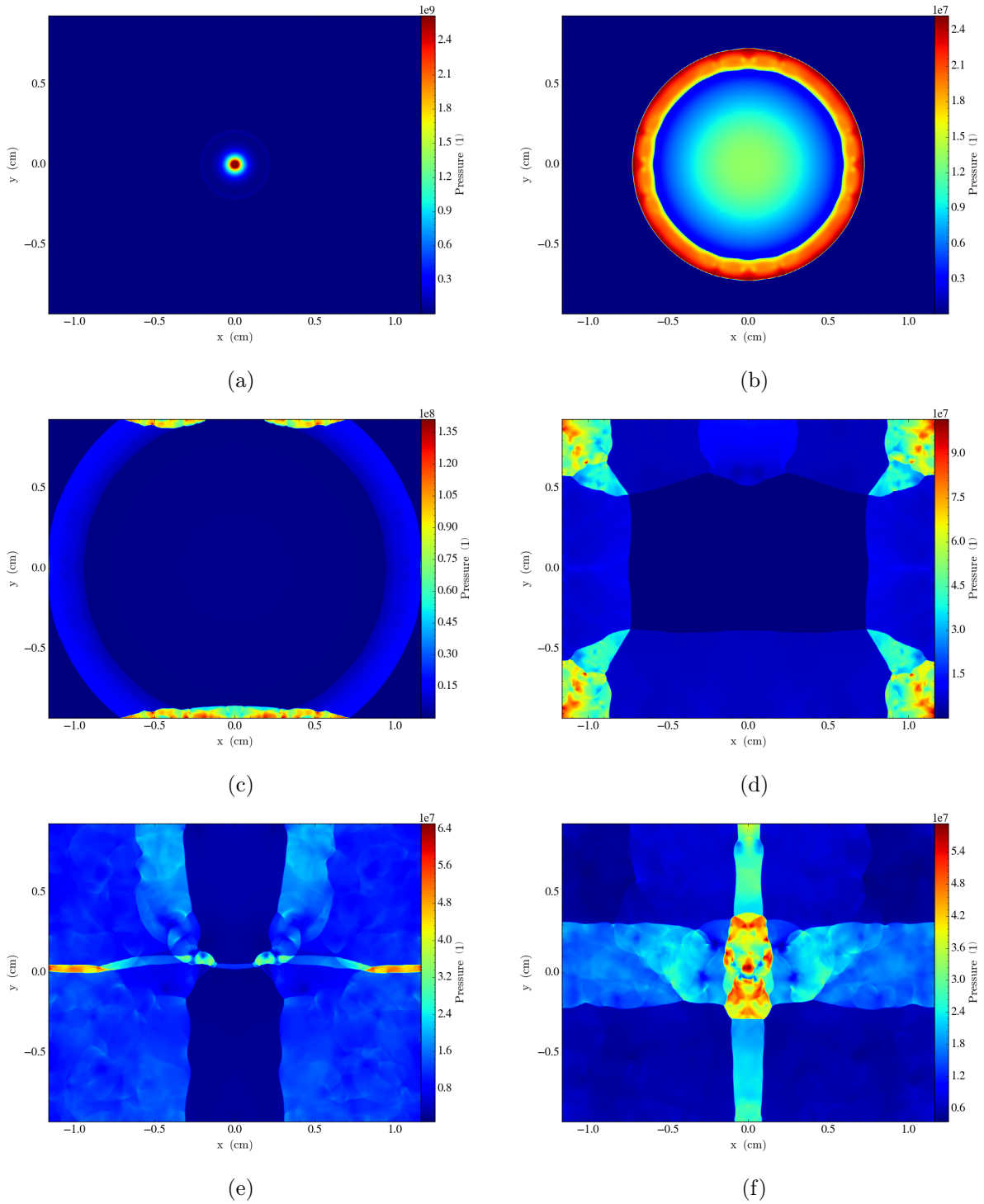

Figure 5.7: Pressure contour plots.

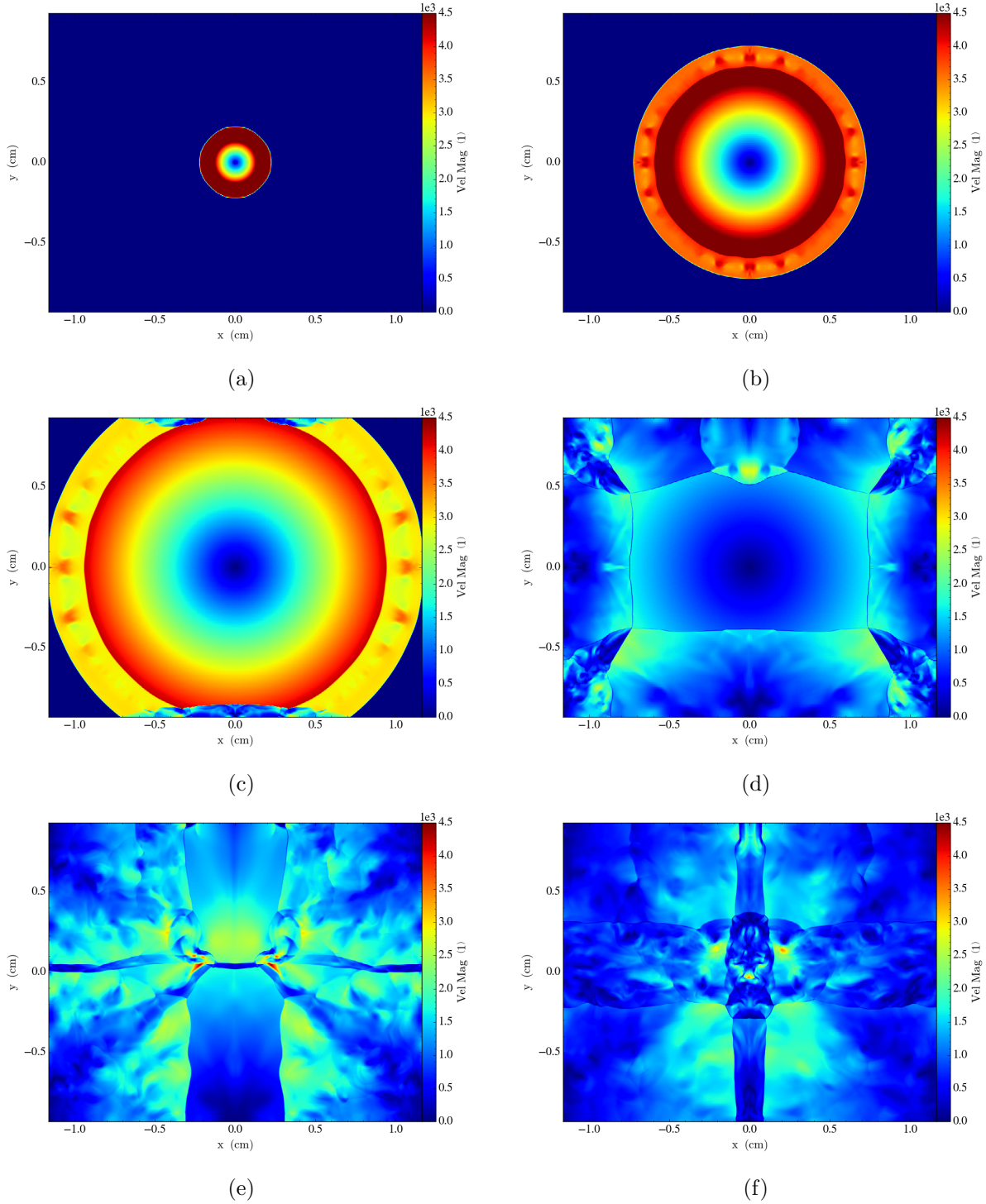

Figure 5.8: Velocity contour plots.

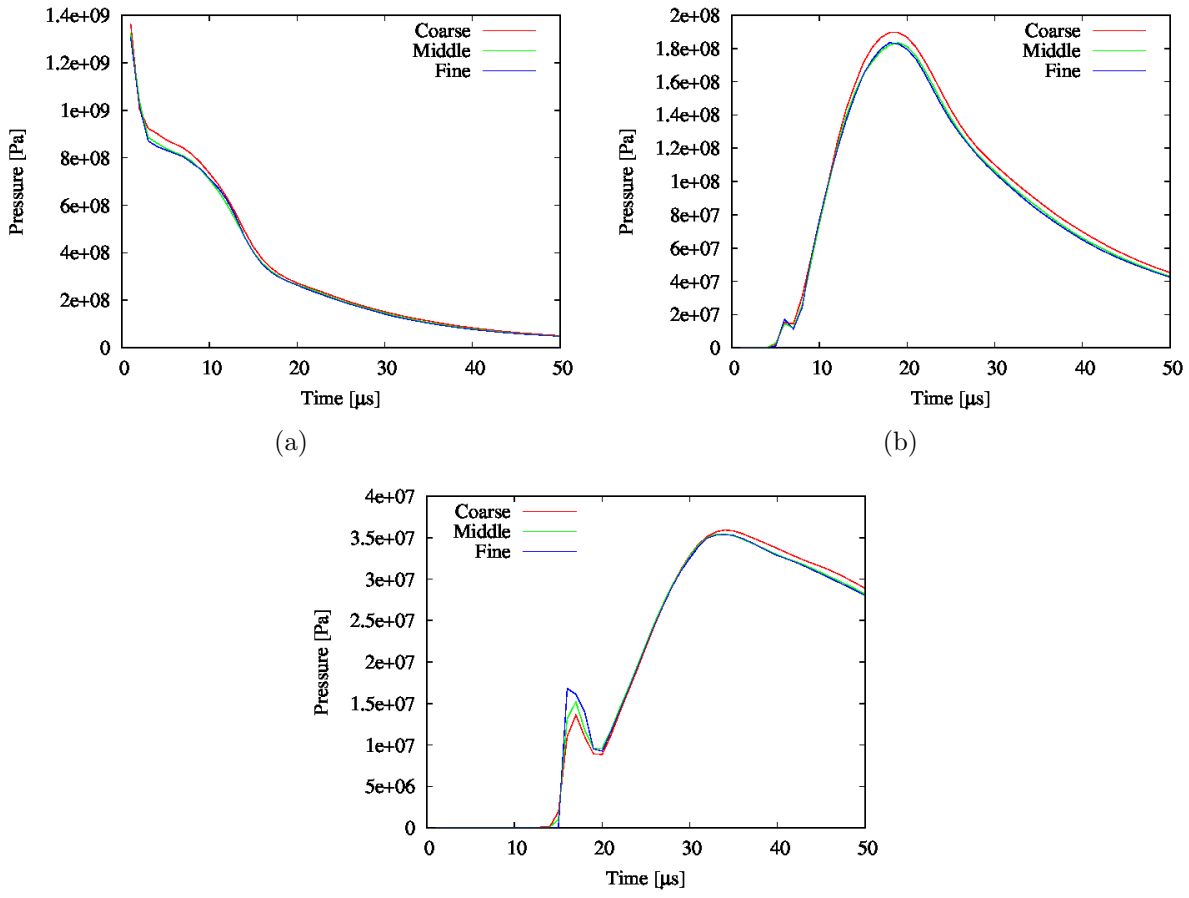

Figure 5.9: Pressure history at three different locations. All locations are in center plane which is parallel to the floor. The distance from center axis of charge d varies; (a) d = 0.02286[m], (b) d = 0.5[m], and (c) d = 1.0[m].

from the other two cases although the same tendency is captured. The middle and fine case shows good agreement in quantitative sense, which indicates that the grid is fine enough in middle size grid. Therefore, the middle size grid is used for all following studies.

Figure 5.10 to 5.13 show the evolution of the blast wave for CASE A. Initially the center part of charge is burnt and has high pressure, whereas the other part of charge is unburnt solid phase. Therefore, the jet going to outside is formed at first. The solid phase prevent the shock wave from propagating into the vertical direction, which results in high pressure region at the contact surface of charge and detonation products. As time passes, the detonation propagates in the vertical directions. Hence, the pressure distributes along the vertical directions, and has a curvature. The combustion of the charge completes around t = 14[s]. After the combustion, the detonation products start expand to the vertical direction with significant velocity. This shock wave expanding to the vertical direction initially has a flat shape due to the influence of charge shape. Also, there is a slight discontinuity between shock expanding to the horizontal and vertical directions, which is similar to the one in full

burnt case.

For the particle case, the evolutions of blast wave shape for case A to E are shown in Figure 5.14. In these figures, there are some perturbations at the top and side of the shock. Although these figures show that lighter particles tends to move faster than heavy one, there is no significant difference between all cases in quantitative sense. Also, the pressure histories seem identical for all cases, which are shown in Figure 5.15. This indicates that the numerical diffusion due to the numerical scheme or grid resolution is so large that the perturbations induced by particles are dissipated.

5.4 Blast Wave in Rooms with Hallways

5.4.1 Simulation Setup

The initial detonation profiles were obtained from Dr. Douglas Nance (Eglin Air Force Base) [65]. This is based on a one-dimensional Direct Numerical Simulation (DNS) employing the Gas-Interpolated-Solid Stewart-Prasad-Asay (GISPA) method for the detonation process [66]. This method permits time-accurate simulation of detonation from the time of the initial shock through the completion of the explosive burn. The robustness of the GISPA algorithm is emphasized by its ability to capture the reaction zone as well as the Von Neumann spike. The GISPA method is based upon the reactive Euler equations [67].

$$\frac{\delta U}{\delta t} + \frac{\delta F}{\delta x} = S_G + S_{Rx} \tag{5.2}$$

Here $U = (\rho, u, E, \rho\lambda)^T$ is the vector of conserved variables. λ denotes the reaction progress state variable, and $F = (\rho u, \rho u^2 + p, u(\rho E + p), \rho u\lambda)^T)$ is the flux vector. The source term S_G mathematically corrects the one-dimensional equations for non-planar coordinate systems.

$$S_G = \frac{-j}{x}(\rho u, \rho u^2 + p, u(\rho E + p), \rho u\lambda)^T) \tag{5.3}$$

Here x denotes distance, and j is set to 0 for planar, 1 for cylindrical, and 2 for spherical. The progress of the detonation is governed by a reaction rate expression S_{Rx}, which can take different forms for different explosives [68]. These equations are solved with the use of appropriate equations of state for both the condensed explosive and the detonation products. For the condensed explosive, the Hayes equation of state is used [69], while the JWL equation of state is used for the detonation products. The Glaister's [70] version of the Roe scheme is used with MUSCL reconstruction for solving the equations to obtain the initial detonation profile. The detonation initialization based on the GISPA method is more realistic than other ways of initialization, such as the "programmed burn" algorithm [71], and the constant volume explosion initialization. In the programmed burn algorithm, the detonation wave speed needs to be known a priori, which may not always be the case. In the constant volume explosion initialization, since the pressure field is assumed constant, the early momentum transfer characteristics from the gas to the particles can be erroneous. Since the GISPA algorithm is based on first principles, we believe that this initialization is more realistic than the other procedures.

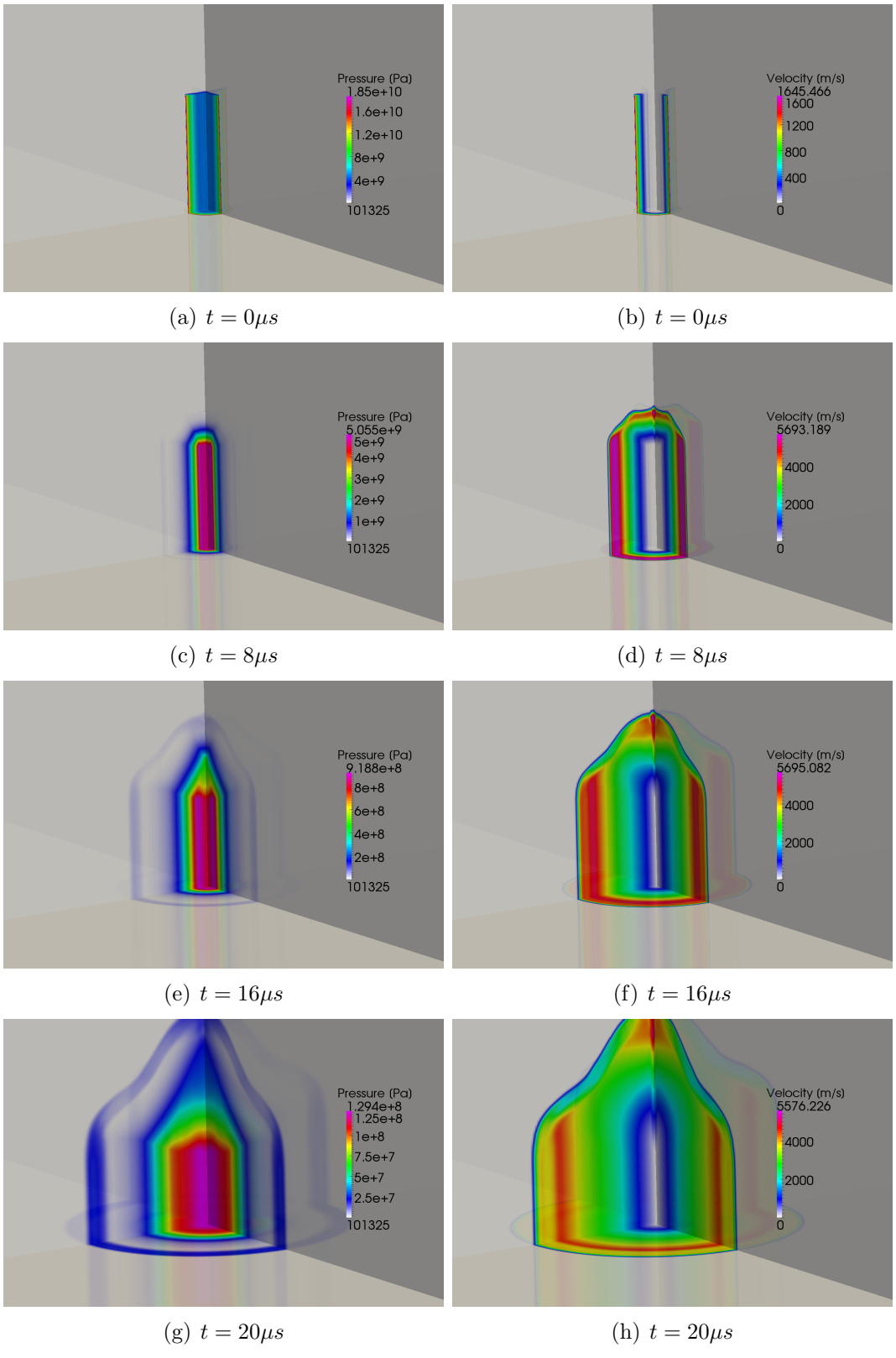

(a) $t = 0\mu s$ (b) $t = 0\mu s$

(c) $t = 8\mu s$ (d) $t = 8\mu s$

(e) $t = 16\mu s$ (f) $t = 16\mu s$

(g) $t = 20\mu s$ (h) $t = 20\mu s$

Figure 5.10: Blast wave formation of full burnt case. Left: pressure, right: velocity.

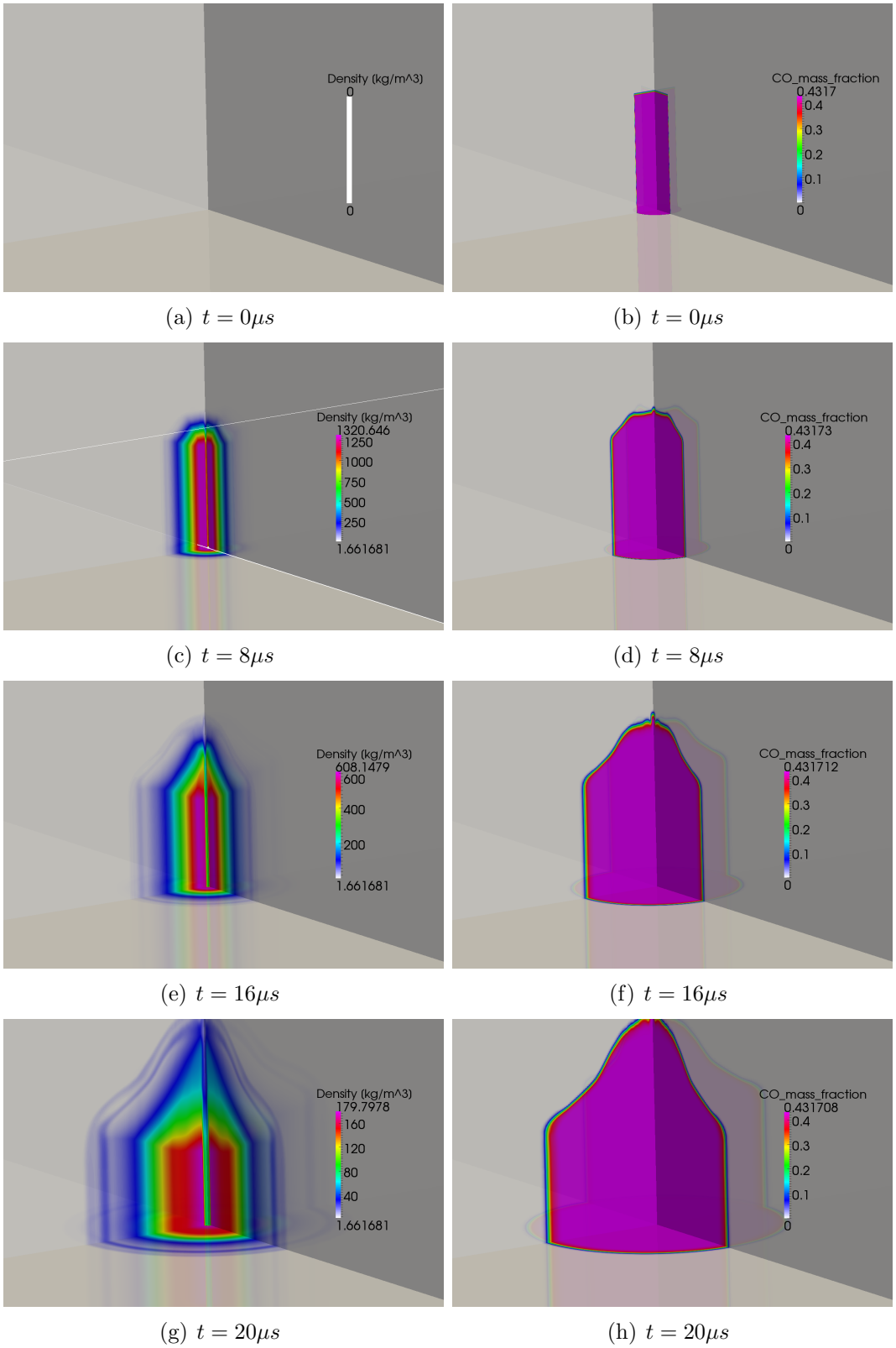

(a) $t = 0\mu s$ (b) $t = 0\mu s$

(c) $t = 8\mu s$ (d) $t = 8\mu s$

(e) $t = 16\mu s$ (f) $t = 16\mu s$

(g) $t = 20\mu s$ (h) $t = 20\mu s$

Figure 5.11: Blast wave formation of full burnt case. Left: Density, right: Mass Fraction of CO.

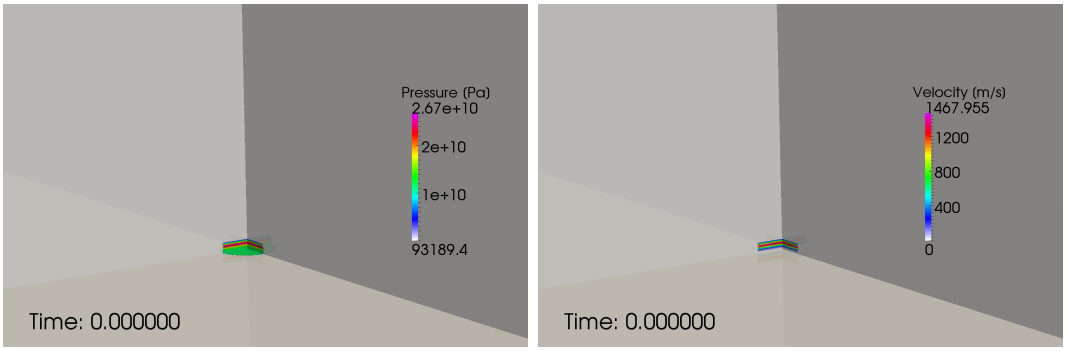

(a) $t = 0\mu s$

(b) $t = 0\mu s$

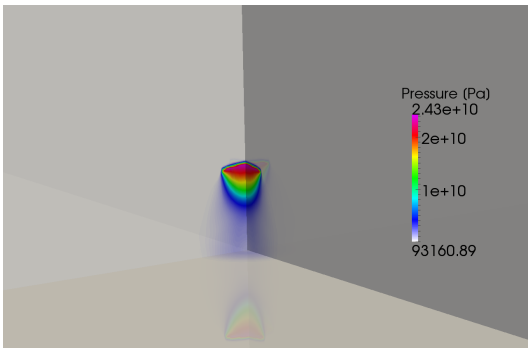

(c) $t = 8\mu s$

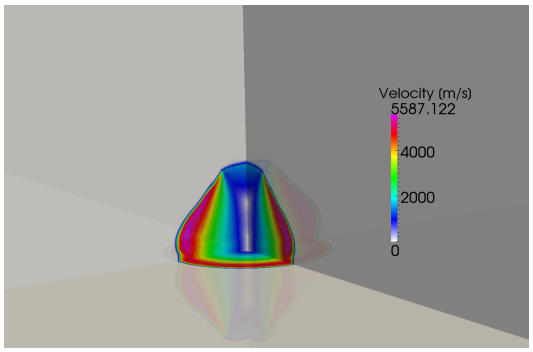

(d) $t = 8\mu s$

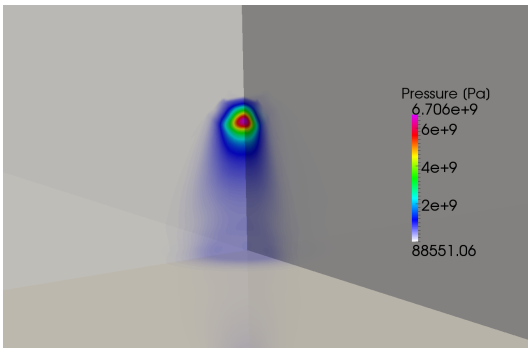

(e) $t = 16\mu s$

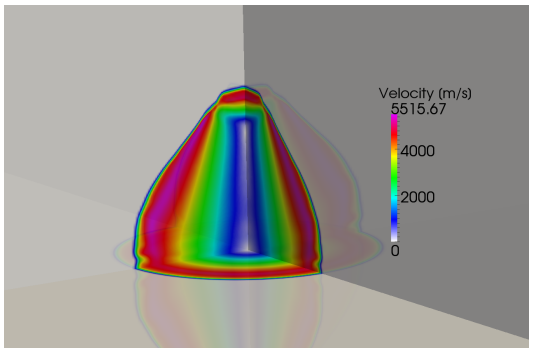

(f) $t = 16\mu s$

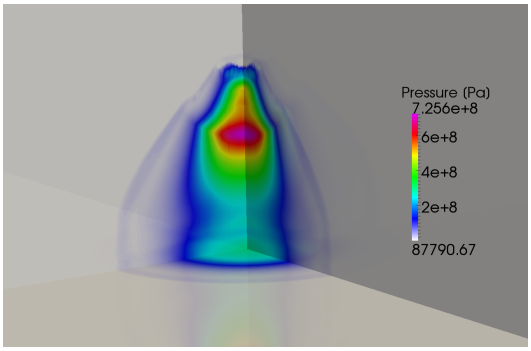

(g) $t = 20\mu s$

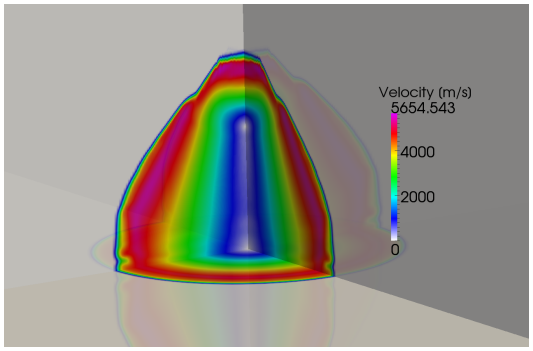

(h) $t = 20\mu s$

Figure 5.12: Blast wave formation of center burnt case. Left: pressure, right: velocity.

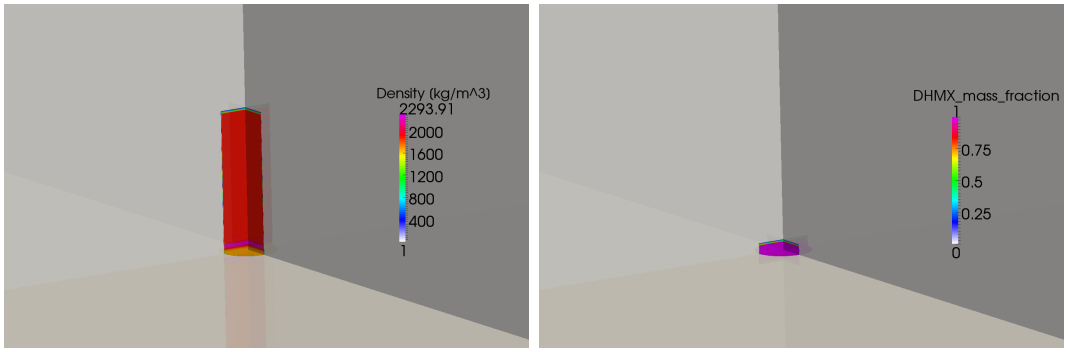

(a) $t = 0\mu s$

(b) $t = 0\mu s$

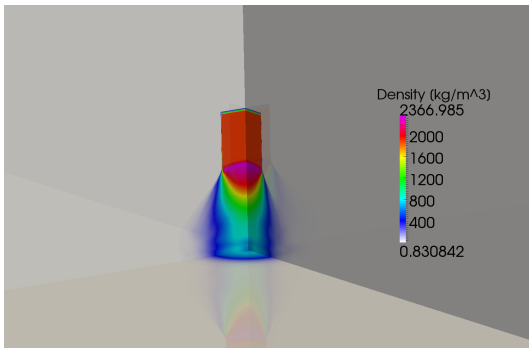

(c) $t = 8\mu s$

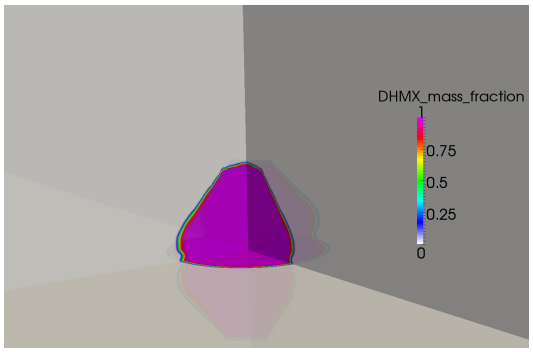

(d) $t = 8\mu s$

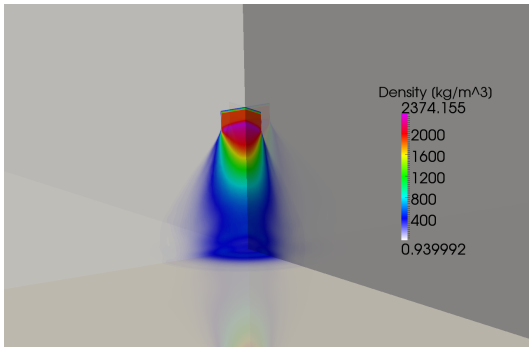

(e) $t = 16\mu s$

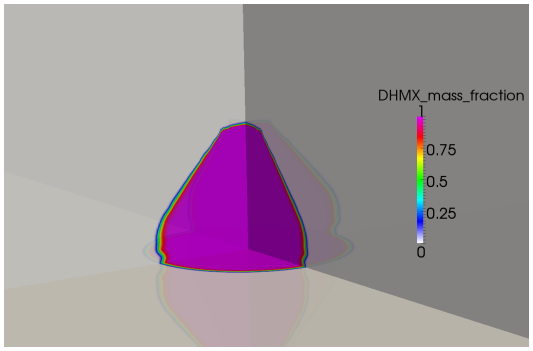

(f) $t = 16\mu s$

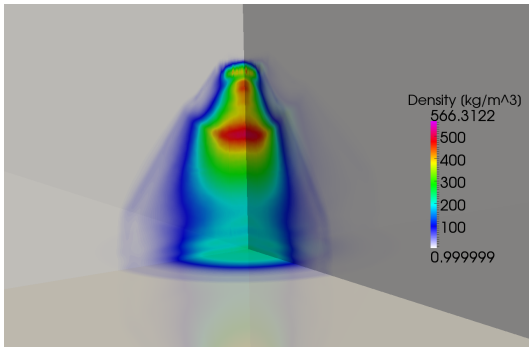

(g) $t = 20\mu s$

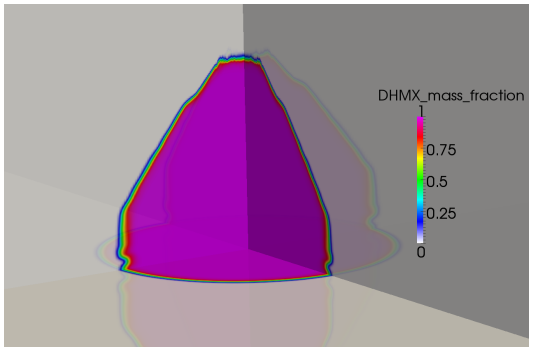

(h) $t = 20\mu s$

Figure 5.13: Blast wave formation of center burnt case. Left: density, right: mass fraction of DHMX.

(a) Case A

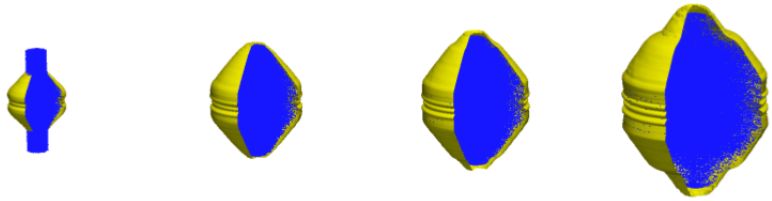

(b) Case B

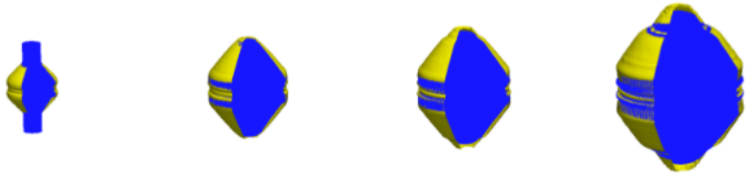

(c) Case C

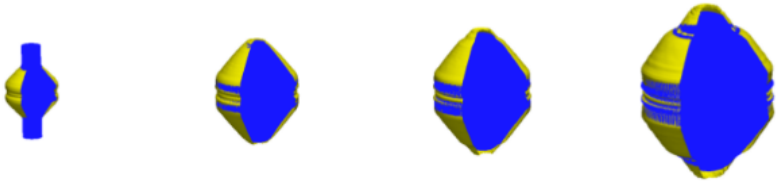

(d) Case D

(e) Case E

Figure 5.14: Evolution of blast wave. Contour corresponds iso-surface of $Y_{DHMX} = 0.5$, and particles distributions are also shown. From left to right, figure corresponds t = 8, 16, 20, and 30[s]

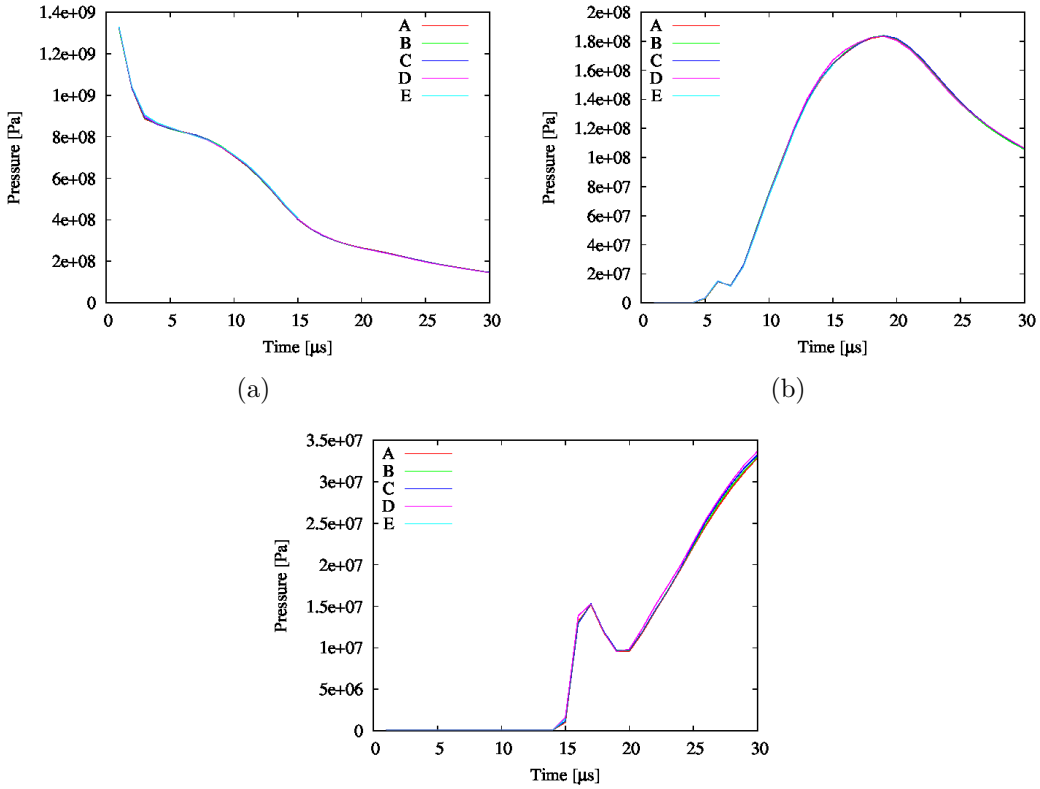

Figure 5.15: Pressure profiles for case A to E. All locations are in center plane which is parallel to the floor. The distance from center axis of charge d varies; (a) d = 0.02286[m], (b) d = 0.5[m], and (c) d = 1.0[m].

Table 5.2: Soot burning mechanism implemented in current study

Number	Elementary reactions
1	$C(S) + 0.5O_2 = CO$
2	$CO + 0.5O_2 = CO_2$

Table 5.3: Simplified reaction mechanism for C4

Number	Elementary reactions
1	$OH + O = H + O_2$
2	$OH + H = H2 + O$
3	$OH + OH = H2O + O$
4	$OH + H2 = H2O + H$
5	$H + H + M = H2 + M$
6	$H + O + M = OH + M$
7	$O + O + M = O2 + M$
8	$H + OH + M = H2O + M$
9	$OH + CO = CO2 + H$
10	$CO + O + M = CO2 + M$

5.4.2 Chemical Kinetics

MRTF tests are conducted with C4 explosive. Additionally in this work NM is used to carry out comparative study to check the charge effect on pressure signals. C4 is composed of 91% RDX ($C_3H_6N_6O_6$) and 9% binders such as DOP ($H_{38}C_24O_4$), PIB (H_8C_4), and fuel oil. The constituents of the fireball for C4 and NM charge are defined as:

$$\text{C4 Detonation} : 2.713\text{H2O} + 1.0732\text{H2} + 2.608\text{N2} + 2.608\text{CO} + 1.252\text{C(S)}$$
$$\text{NM Detonation} : 0.2296\text{N2} + 0.295\text{H2O} + 0.459\text{CO} + 0.0164\text{H2}$$

Chemical kinetics mechanism for hydrocarbons is typically very complex involving numerous species reacting with each other intermittently in several different steps. Currently, a simple two step mechanism has been employed in the study. This chemistry assumes soot to be present in the gaseous phase.

However, this approach has its limitation and therefore an implementation of a more complex and detailed chemistry is under progress. The proposed chemistry mechanism involves 9 species and 10 reversible reactions [72].

Table 5.4: Simplified soot oxidation path

Number	Elementary reactions
1	$C(S) + 0.5O_2 = CO$
2	$CO + 0.5O_2 = CO_2$

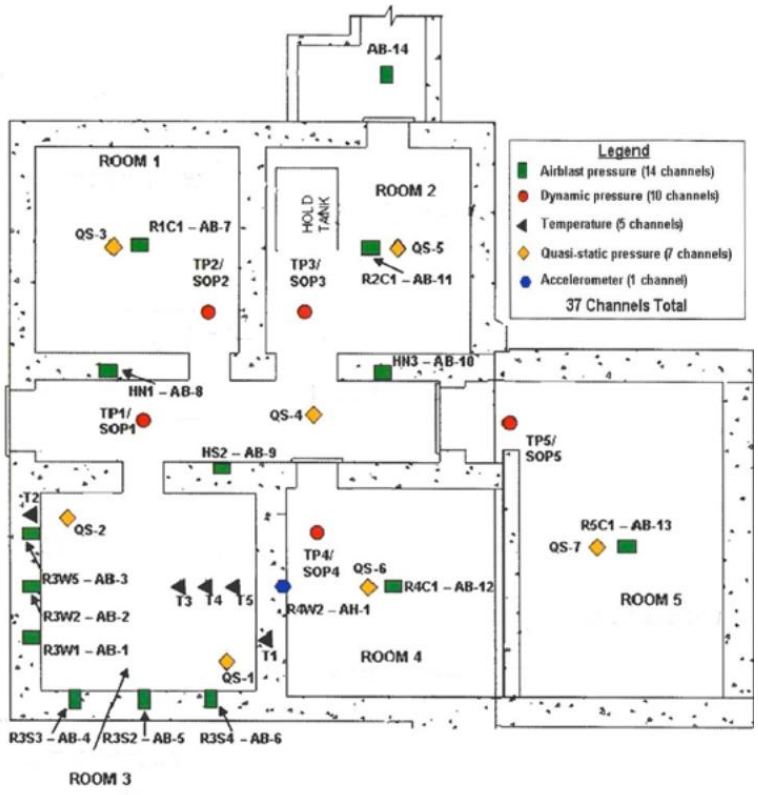

Figure 5.16: MRTF test structure and QSDD instrumentation

5.4.3 Experimental and Numerical Configuration

The MRTF or the multi room test facility is a five room concrete structure, as shown in Figure 5.40 [72]. There is an internal hall-way which connects these rooms. Pressure and temperature gauges are installed in the entire structure to measure various explosive parameters.

Room 3 is the cynosure of this study as this room serves as the static detonation room. The room is fit with 9 pressure gauges to measure the shock pressure and the quasi-static pressure. The room also includes 3 temperature gauges. The room dimensions are shown in Figure 5.17. Its a 21 ft. X 19 ft. X 9.5 ft. room with a 10 vent in the ceiling at the center. There is a 4 ft. X 4 ft. door which connects it to the hallway. Another configuration including the hall-way has been tested to make sure that the outflow boundary condition at the exit of the room is not making any difference to the chamber pressure signals. A detail of this configuration is given in Figure 5.17. Twenty lbs of C4 is detonated at the center of this room. The uncased cylindrical charge is 4.5 in diameter and 22.5 long.

The computational grid required for the simulation has been created using ICEM-CFD meshing software. The multi-block, structured mesh is composed of 2632 blocks enumerating 22 million grid points. Figure 5.18 shows the block distribution and the mesh. The blocking has been done in such a fashion that it enables to have a cylindrical grid at the center of the room to represent a cylindrical charge accurately.

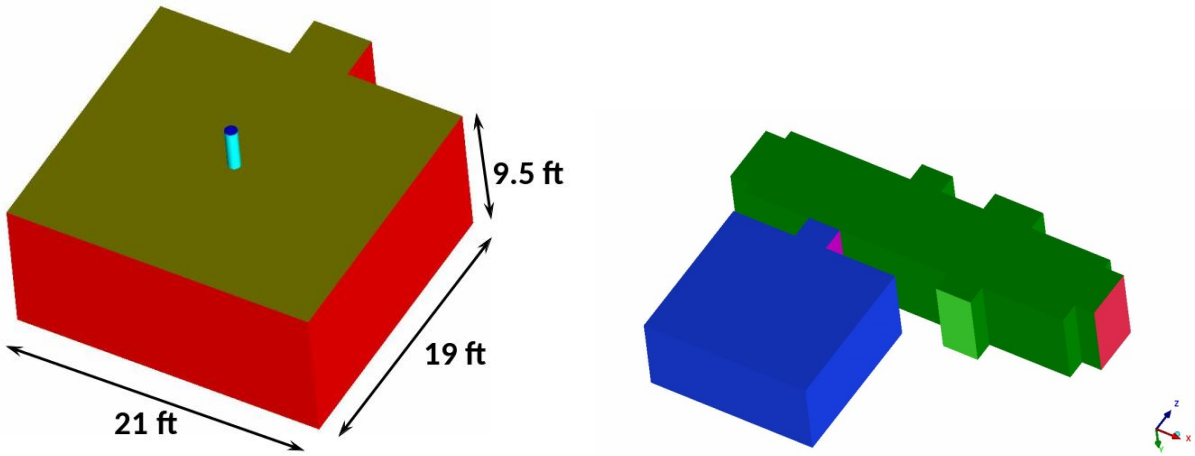

Figure 5.17: 2a : Dimension details of Room 3, 2b : Room 3 with hallway

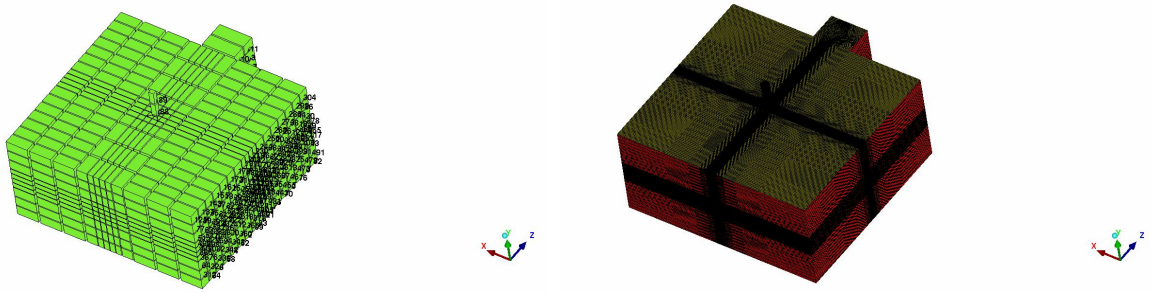

Figure 5.18: Block distribution and overall mesh details of Room 3 grid

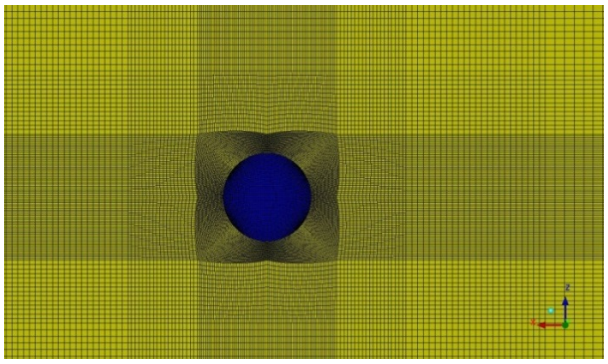

Figure 5.19: Section view of the O-grid (Room 3)

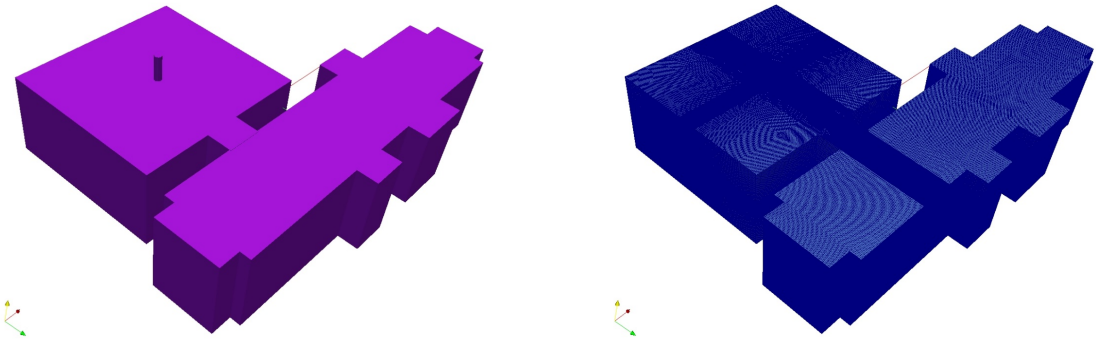

Figure 5.20: Room 3 grid with hall way

O-grids are used in the cylindrical region section while careful grid stretching has been implemented to gradually relax the grid size towards the walls of the room. This strategy saves grid points and thereby reduces computational effort. Figure 5.19 shows the section view of grid with core section detailing the O-grid.

Grid coarsening technique has been implemented for the room with hall-way configuration. Figure 5.20 shows the details of this configuration and grid.

Wall boundary condition is used on all walls whereas supersonic outflow condition is implemented at the vent-hole exit and the room-door exit plane.

5.4.4 Results and Discussions

In this section, results for various simulations have been reported. Table 5.5 summarizes the run matrix.

Run 1 and 2 evaluate the effect of the exit boundary condition. Run 2 domain is limited to the exit door of Room 3. The objective of comparing these two runs is to check whether, wave reflection from the door is significant to perturb the pressure signals as recorded by the pressure transducers fit in Room 3. Most of the earlier studies dealing with blast or explosion performed at CCL have dealt with spherical charge. In this study, the interpolation

Table 5.5: Simulation Matrix

Run	Configuration	Explosive	Reactive	Charge Shape
1	Room 3 with Hall	C4	No	Cylindrical
2	Room 3	C4	No	Cylindrical
3	Room 3	C4	No	Spherical
4	Room 3	NM	No	Cylindrical
5	Room 3	C4	Yes	Cylindrical

methodology to get the initial detonation profiles has been extended to cylindrical charges to calculate the initialization. A comparison study between a spherical and cylindrical charge has been carried out to understand the effect of charge shape on pressure signals and flow field. A comparative study between two different charges e.g. NM and C4 has also been reported. While the first four runs are carried out in non-reactive setup, the fifth run is performed with chemistry switched on. Te simulation runs were started with a grid with 16 million grid points. There after a systematic grid refinement is done throughout the domain to achieve a grid independent solution. The final grid has 22 million grid points. It should be noted that the study has been carried out for Room 3 in a non-reactive domain with the purpose of saving computational time. Once, the grid independency has been achieved, the same mesh resolution has been applied to the hall way.

One of the primary objectives of the project is to evaluate soot particle dispersion characteristics from the Euler-Lagrangian solution. Soot particles are typically of 3-3.5 micron size. To have considerable soot mass loading, it would require tracking billions of particles. Eulerian-Lagrangian calculations are computationally expensive, so any strategy to reduce domain dimension and/or grid points is cherished. The pressure pulse results for Room 3 configuration and Room 3 with hallway configuration has been presented in Figure 5.21. Again, it should be noted that this results are for non-reactive runs and the grid density for this run is intermediate (16 million). From the results it can be seen that there is insignificant (¡5%) difference in pressure pulse till 55 millisecond. After wards, there is considerable amount of difference in the pressure pulse behavior. Room 3 shows higher value afterwards primarily because of pressure wave reflection from the door exit.

Figure 5.22 shows the instantaneous flow field of pressure. The pressure waves leave the exit door of Room 3 and get reflected from the walls of the hall. Adding the other rooms to this domain would therefore be expected to completely mitigate the wave reflection and thereby affecting the pressure signals.

Figure 5.23 shows the soot mass fraction plots at two different time instances.

5.4.5 Non reactive C4 Charge

Figure 5.24 shows the comparison of pressure time history between experimental data and non-reactive C4 explosion in Room 3 configuration for non-reactive case (without after burning). From the chart it is visible that there exists considerable amount of delay for the first and subsequent shock arrival time. Also, the peak pressure is less for the simulation by about 50 psi. As time progresses, the delay in shock arrival time also increases. However,

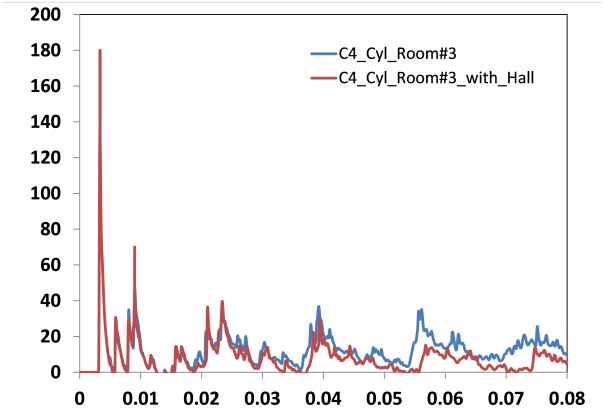

Figure 5.21: Comparison of the pressure signals between Room 3 and Room 3 with hallway configurations

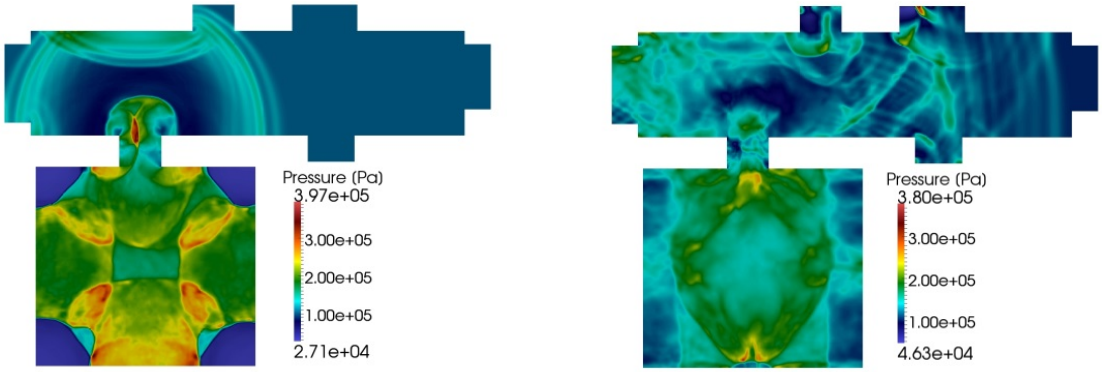

Figure 5.22: Room 3 with hall configuration: Instantaneous pressure fields at 15.5 and 34.2 milliseconds

the number of peaks obtained from the simulation is quite satisfactory as it matches the experimental data closely.

Figure 5.25 shows instantaneous flow fields of pressure for Room 3 configuration on a section plane that is at the center of the room. The explosion initiates a pressure wave which hits the wall, gets reflected and moves towards the center of the room colliding with the next wave generated by the blast. Every pressure peak in Figure 5.25 corresponds to the situation when two different pressure waves happen to coalesce at the location of pressure measurement generating a high pressure region. This can be seen from Figure 5.25 d where the high pressure region is concentrated approximately at the location of QSDD AB1 whereas from Figure 5.25-e it can be seen that the high pressure zone is at the corners. This phenomena keeps on repeating itself resulting in the pressure peaks as can be seen in the pressure signal data. With the passage of time, the strength of the blast diminishes resulting in increased time difference between two pressure peaks and reduced pressure peak values.

Figure 5.26 shows instantaneous flow fields of pressure for Room 3 configuration from

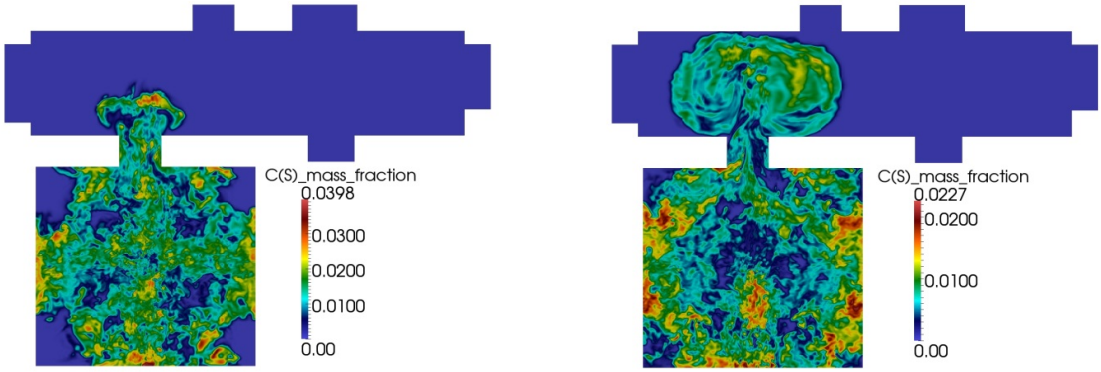

Figure 5.23: Room 3 with hall configuration: Instantaneous soot mass fraction at 15.5 and 34.2 milliseconds

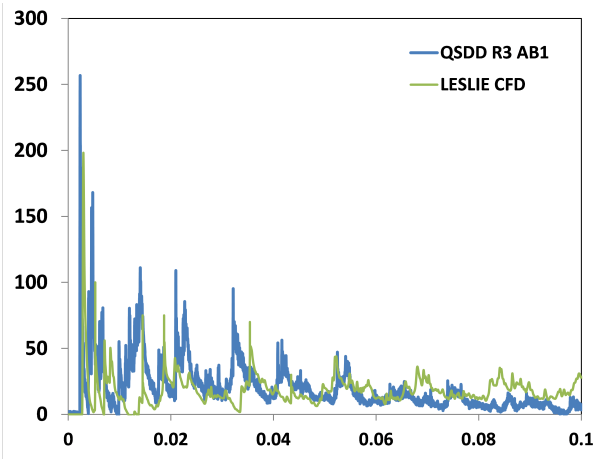

Figure 5.24: Comparison between experimental and simulation pressure history for QSDD AB1 sensor

another view (side view). The same conclusion can be drawn from this figure as well.

Figure 5.27 shows the soot evolutoon at this time shots. Untill 2.74 milliseconds the identity of the fireball can be distinguished, However, after that mixing dominates and identity of the fireball is lost. Interactions of pressure waves reflecting from the wall causes disturbances to the flow field and the RMI are further enhanced leading to a more complex mixing region. Further analysis is still needed to fully understand all these features.

5.4.6 Effect of Charge Shape

Figure 5.28 shows effect of charge shape (cylindrical vs. spherical) on the pressure pulse. For both the cases, mass and volume of the charge has been conserved. The equivalent radius of the spherical charge comes out to be 4.404 which has same volume as the cylindrical charge.

The arrival of first pressure peak is off by 2 milliseconds for the spherical charge compared to cylindrical charge. Also, peak pressure is 40 psi less compared to cylindrical charge. The

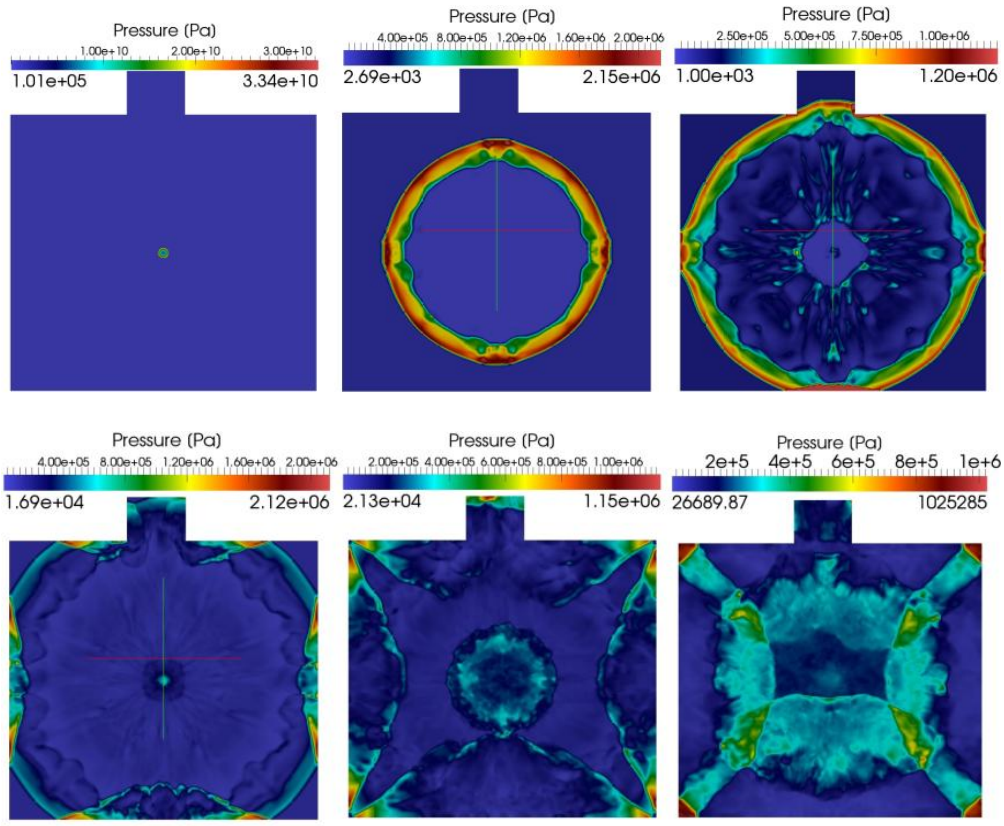

Figure 5.25: Instantaneous pressure field snapshot for Room 3 configuration as viewed from the top at 0, 1, 1.87, 2.74, 3.77 and 4.87 milliseconds

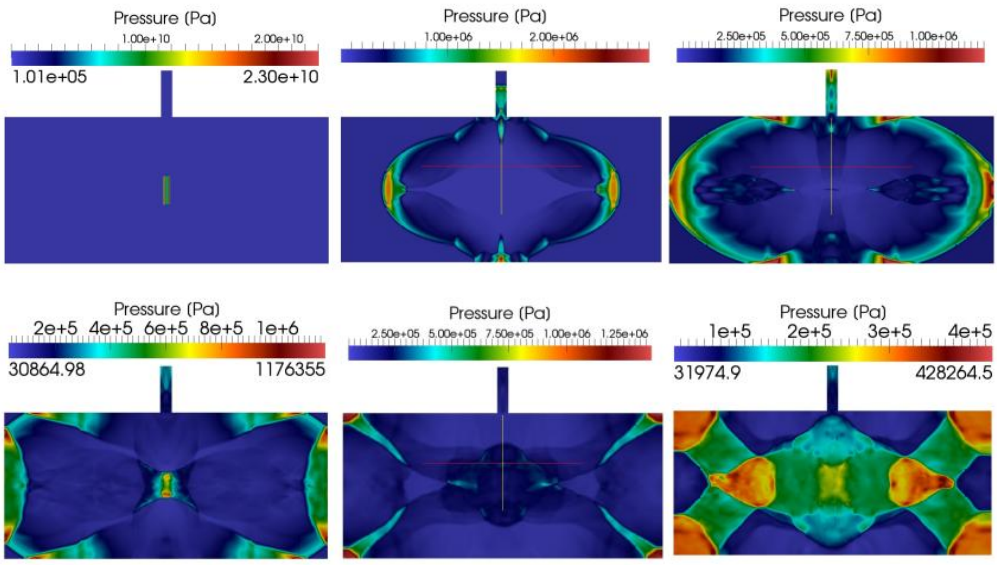

Figure 5.26: Instantaneous pressure field snapshot for Room 3 configuration as viewed from te side at 0, 1, 1.87, 2.74, 3.77 and 4.87 milliseconds

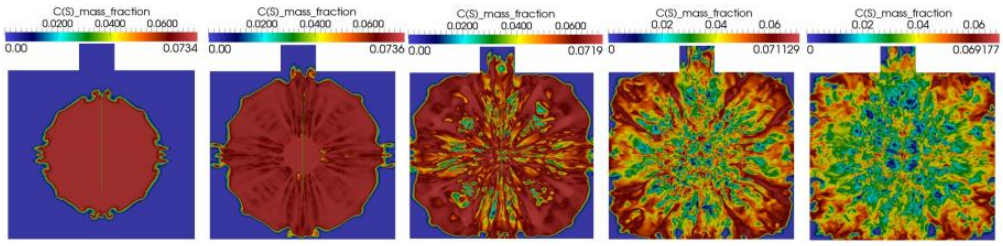

Figure 5.27: Instantaneous mass fraction of soot field for Room 3 configuration as viewed from the top and side at 1, 1.87, 2.74, 3.77 and 4.87 milliseconds

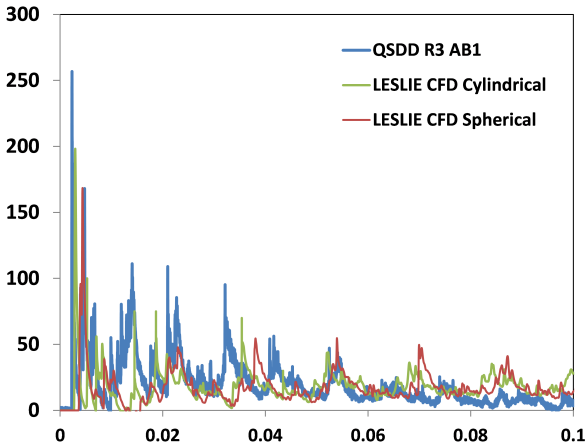

Figure 5.28: Comparison between experimental and simulation pressure history for QSDD AB1 sensor for C4 cylindrical vs. spherical charge

characteristics of the initial pressure pulses (till 50 milliseconds) seem to be quite different, however, as time progresses the signals become similar. Figure 5.29 shows instantaneous flow field of pressure for the spherical charge case for two different views side and top view. The pictures show multiple pressure wave coalescence phenomena which is happening intermittently inside the room.

Figure 5.30 shows instantaneous flow field of soot mass fraction for spherical charge. The overall flow features are similar to a cylindrical charge. More analysis is stull underway.

5.4.7 Effect of Charge Material

Figure 5.31 shows effect of charge material on the pressure pulse. C4 is a stronger charge compared to Nitro-methane. The peak pressure is 110 psi less for NM charge. The time of arrival of shocks is delayed for NM charge because of decrease in shock velocity.

Figure 5.32 shows instantaneous flow fields of pressure for two different sectional views. Similar flow features as compared to C4 charge are observed with Nitro-methane charge also.

Figure 5.33 shows the evolution of CO mass fraction as time progresses. The mushroom like structures caused by RM instability is present in the flow field. Visibly these structures are different for C4 and Nitro-methane charge.

5.4.8 Effect of After-Burning

Figure 5.34 shows effect of after burning on the pressure pulse. The computed results for reactive case match experimental data much better than the non-reactive case. The peak shock values and shock arrival time are in better accordance with that of the experiments. This clearly shows after-burning has huge impact on the flow dynamics of a confined spaced environment.

The result shows higher value of pressure after 60 milliseconds compared to experiments which might be due to the fact that this domain is limited to the single room configuration.

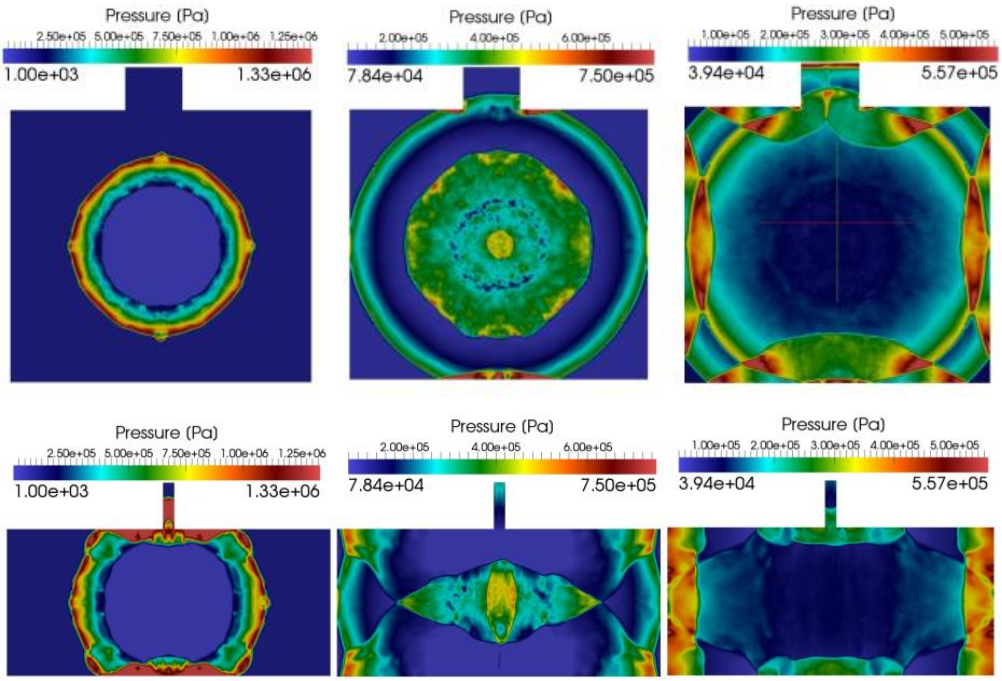

Figure 5.29: Instantaneous pressure field for Room 3 configuration as viewed from the top and side at 1, 2.92 and 4.67 milliseconds

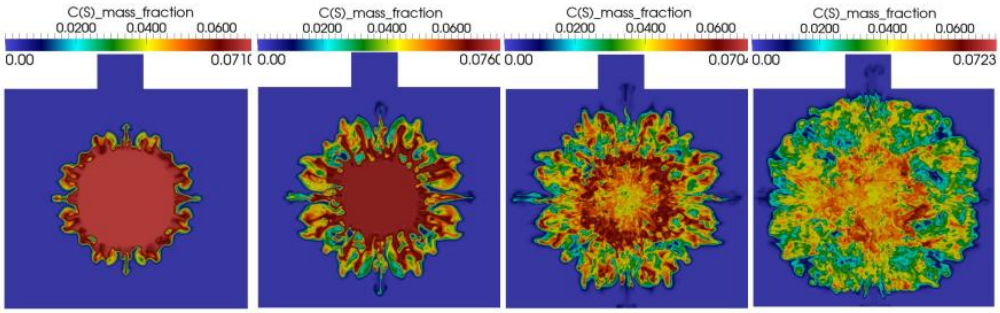

Figure 5.30: Instantaneous mass fraction of soot field for Room 3 configuration as viewed from the top and side at 1, 1.63, 2.92 and 4.67 milliseconds

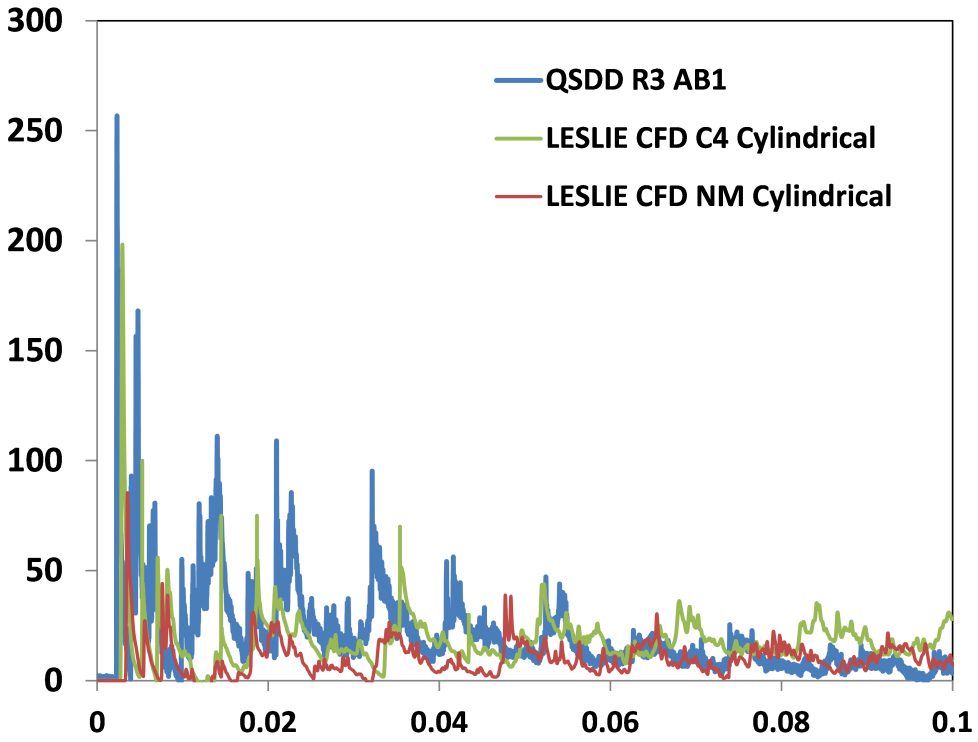

Figure 5.31: Comparison between experimental and simulation pressure history for QSDD AB1 sensor for C4 vs. NM cylindrical charges

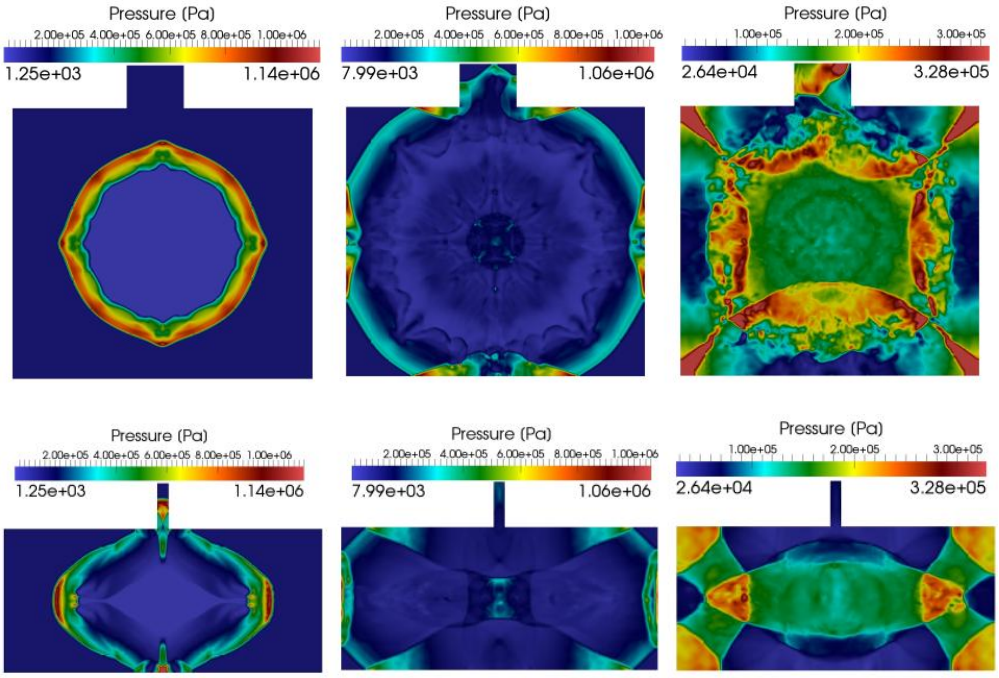

Figure 5.32: Instantaneous pressure field for Room 3 configuration as viewed from the top and side at 1.2, 3.0 and 5.26 milliseconds

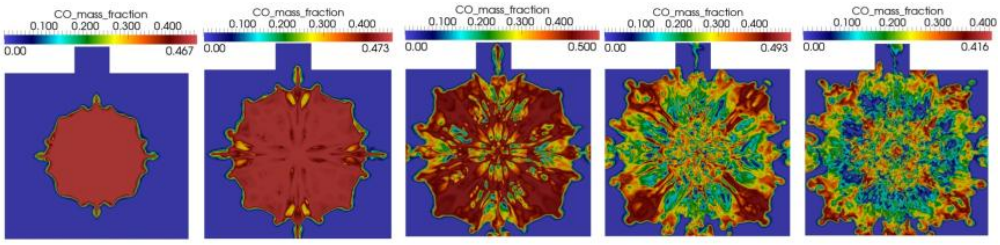

Figure 5.33: Instantaneous CO mass fraction for Room 3 configuration as viewed from the top and side at 1.2, 3.0 and 5.26 milliseconds

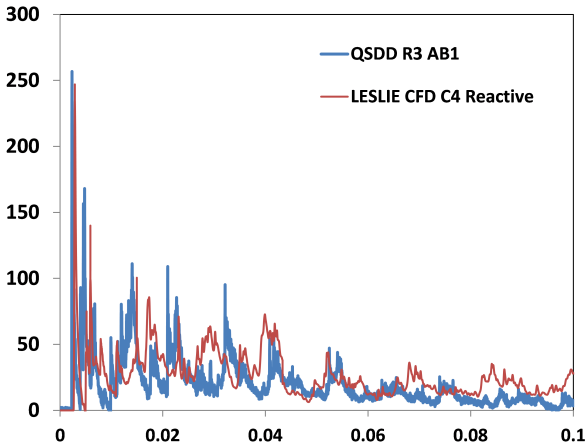

Figure 5.34: Comparison between experimental and simulation pressure history for QSDD AB1 sensor for C4 reactive and non-reactive simulations

A full domain simulation is planned with detailed chemistry in future.

5.4.9 Eulerian-Lagrangian Results

As noted earlier, all the simulations have been performed assuming soot in the gaseous phase, which is obviously erroneous. In an ideal world, the soot combustion should be modeled assuming it to be present in the solid phase. LESLIE code uses E-L methodology to track the particles. Soot particles are typically of 3-3.5 micron in diameter. Density of the soot is 2200 kg/m3. A simple calculation will show that to achieve soot mass fraction present in te C4 charge for a 20 lb. charge, number of soot particles to be tracked is 2 X 10^{13} (yes a billion is just 10^9)! To track these many particles is beyond the hardware capability. Parcel method where every parcel contains identical number of particles with same properties might be useful in this case. In this study, an assumption has been made as to after the detonation soot particles tend to agglomerate and the diameter of the particles increase. A total of 600000 parcels are used with 100 particles per parcel. With these parameters the mass of soot that can be in dispersed phase has been calculated and remaining amount of soot is kept in the gaseous phase as previously. This is the dilute phase condition in E-L scenario. A preliminary run has been setup with the above mentioned parameters. A detailed parametric study is planned in future. Figure 5.35 shows the particle evolution snapshot with time. Initial distribution of the particles is uniform, however as time progresses the distribution becomes highly anisotropic. Effort is going on to calculate the particle source terms information to quantify this anisotropic behavior.

Figure 5.36 shows 3D view of the particle evolution snapshot with time. The particle field shows the jetting pattern seen in unconfined studies. Further studies are underway to determine how the post shock flow field instabilities such as Richtmyer-Meshkov instability and the mixing layer growth is making these wavy and streaky patterns.

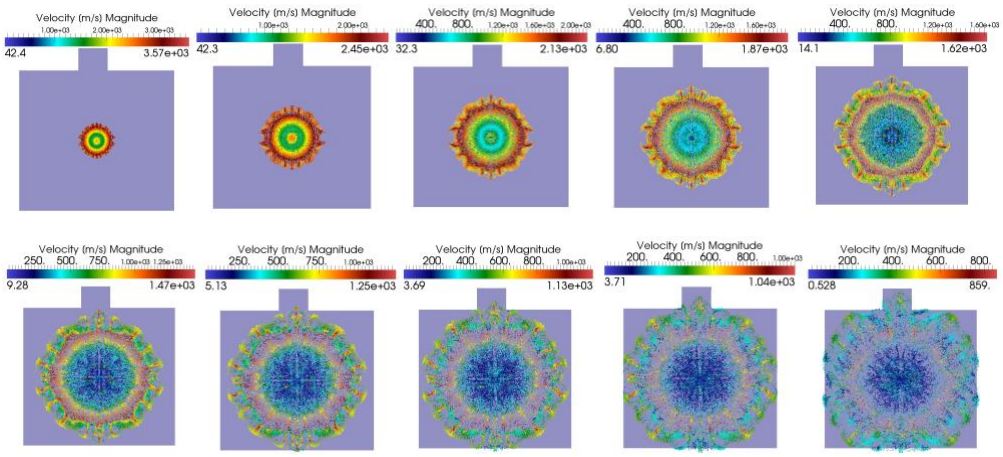

Figure 5.35: Instantaneous Soot particle trace colored by velocity for Room 3 configuration as viewed from the top at 0.15, 0.40, 0.65, 0.95, 1.25, 1.5, 1.85, 2.15, 2.75 and 3.0 milliseconds

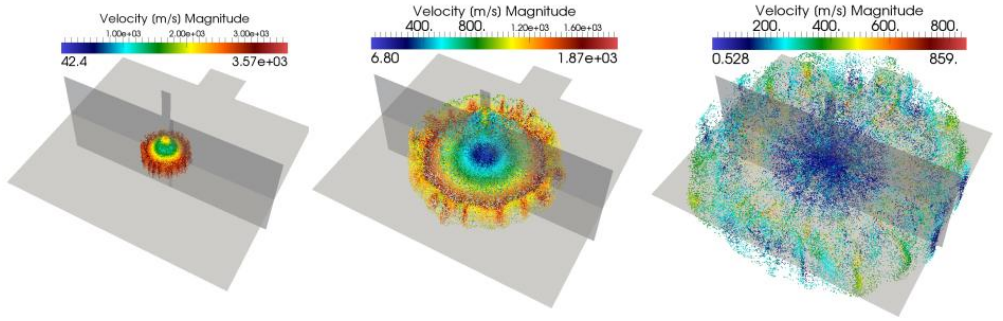

Figure 5.36: Instantaneous Soot particle trace colored by velocity for Room 3 configuration at 0.15, 0.95 and 3.0 milliseconds

5.4.10 Spore Aerosol Modeling

In the current study, droplets of a spore-laden aqueous solution are introduced into the domain of interest, i.e., re-shock zone of shock tube or in the ambiance of a detonated explosive charge. The spores are considered to be of the Bacillus species. Although most spores of this species are elliptical, here, spores are assumed to be spherical with radius, 0.4 micron [14]. The spore aerosol considered has a particular droplet size distribution, concentration of spores in the initial solution and the concentration of spores in the domain. These parameters are set based on past experimental studies [15] so that the current results can be compared with the results available in the literature.

When the spore aerosol interacts with hot gases in either post-shock or post-detonation flow, the water enveloping the spores evaporates and exposes the spores to the heat. Based on the aerosol droplet radius there could be multiple spores in a given droplet. These spores after the evaporation of water can stay clustered or disperse. As the temperature of the spores increases, based on the quantity of heat received by each spore, the spore kill can occur due to heating or mechanical rupture. When spore-laden aerosol is nebulized, the droplets of aerosol are distributed in the domain of interest with each droplet having an initial radius r_p^0. In general, r_p^0 can be specified based on a distribution function. However, as the exact distribution of the droplet size is not known, r_p^0 (microns), based on a Gaussian distribution, is specified as $r_p^0 = min(\eta, \mu_\eta)$, where η is Gaussian random variable with mean μ_η and standard deviation σ_η. As the values of μ_η and σ_η are not available, a range of values are used initially for the shock tube simulations and the values which provide good agreement with experimental results are then used in cases with explosive charges. Also, the initial atomization is assumed to reduce all droplets to size less than μ_η. Further, number of spores per droplet n_p^s is set based on the concentration of the spores in the initial aqueous solution. In the current study, for initial spore concentration of 10^10 spores/ml, n_p^s varies from 1 to 5. Also, the concentration of the spores in the domain, μ_η is kept at 1000 spores/cc. Due to the heat transfer to the droplets in the post-shock region, the water encapsulating the spores evaporates and this rate of mass transfer is given as [16]

$$\dot{m} = 2\pi\rho D r_p Sh(1 + B_M) \tag{5.4}$$

Here D is the diffusivity of the gas. The expressions for Nusselt number (Nu), Sherwood number (Sh) and the Spalding mass transfer number (B_M) for droplets are available elsewhere [16]. After the water evaporates, no mass transfer is considered from individual spores or spore clusters. Hence, these expressions for $\dot{m}$ and Nu are used until the radius of the droplet reduces to the effective radius of the spore cluster (or radius of the spore) present inside the droplet, i.e. $r_p > r_S^C$. Here, the effective radius of the spore cluster is determined as :

$$r_s^C = \frac{{n_p^S}^{\frac{1}{3}}}{f_p} \tag{5.5}$$

Here f_p is the packing fraction and is taken to be 1 when $n_p^S = 1$ and 0.74 otherwise, i.e., close packing assumption. The expression for Nu used when is provided elsewhere [19]. When the spores are exposed to HTGE, the temperature of the spores increase to a critical value (T_C). Past calculations of thermo-structural response of individual spores show that

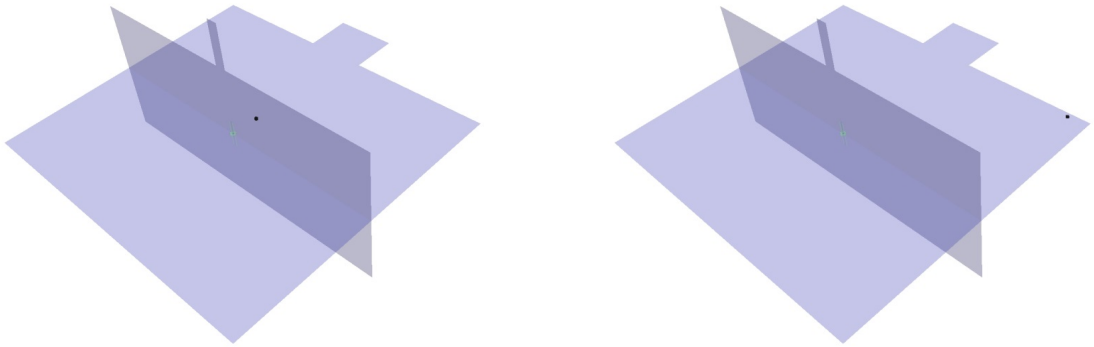

Figure 5.37: Initial Spore Cloud location (marked by black dot) for Room 3 configuration, Case A: Spore cloud located on the top of the charge at an angle 45 degree, Case B: Spore cloud located at an angle 45 degree from the charge in the horizontal plane

this critical temperature should result in spore membrane rupture and/or heating of spore core leading to spore kill [17]. Experimental studies suggest that the loss of spore viability and structural damage occurs at gas temperatures of about 750K and above [18]. However, for the cases considered here, the exact quantity of heat needed to kill a spore or to reach T_C is not available. Hence, T_C is assumed as a variable parameter and a range of values are used in each case to obtain the percentage of spores killed. In cases presented here, any spore whose temperature exceeds T_C is assumed to be neutralized. In this study, spore clouds are put at different locations of the room with different orientation from the charge and thereafter spore dispersion has been calculated. Figure 5.37 shows the initial spore cloud location for these various cases. Two different cases have been chosen for the preliminary study Case: A has the spore cloud located on the top of the charge at 45 degree angle, Case: B has the spore cloud near to the wall but at a 45 degree angle.

Figure 5.38 shows the spore dispersion for Case A with time.

For initial 5 milliseconds the spore cloud is not affected by the detonation as shock wave does not hit it. Once the shock passes through the cloud, the cloud starts to disperse and at the same time gains temperature after interacting with the shock. Dispersion of the spore cloud increases with time leading to a variation in the spore temperature as the spores mix in the post detonation environment. Further studies of spore transport and the entrainment into the turbulent mixing layers are needed to understand the dynamics but such studies requires extensive data processing and these tools are being created for this purpose.

Figure 5.39 shows the spore survival rate as a function of time for the two different cases mentioned above. Clearly being close to the charge helps in increasing post detonation spore kill but in general there are other issues to consider. Preliminary analysis also shows that this is also related to the entrainment in the mixing layers behind the detonation front.

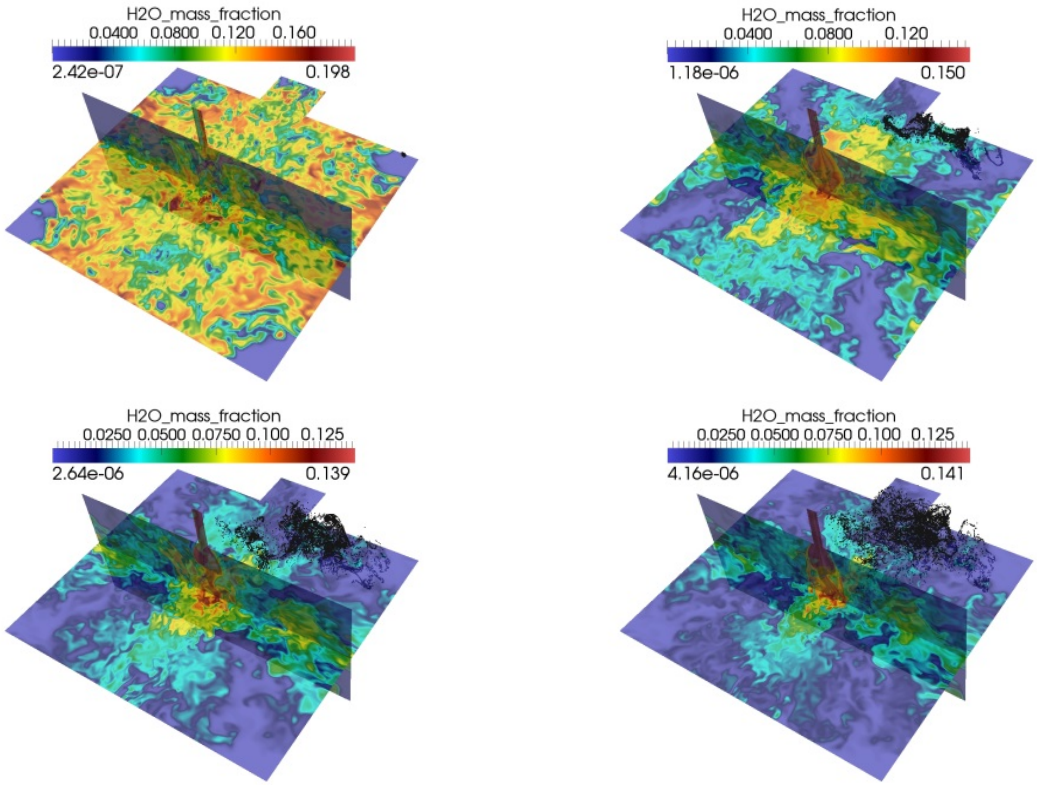

Figure 5.38: Evolution of Spore Cloud (marked by black dots) for Room 3 configuration, for Case A at 6, 16.5, 20.6 and 24.5 milliseconds

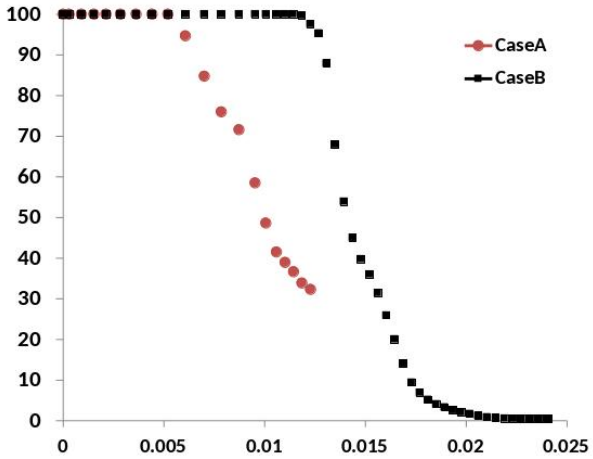

Figure 5.39: Percentage of spores left intact as a function of time for Case A and Case B

5.5 Detonation in a Two Room Configuration

5.5.1 Simulation Setup

To investigate the interaction of spores with hot detonation product gases in a confined environment, a two room configuration, shown in Fig. 5.40 is used. The two room configuration comprises of a inner room enclosed by an outer room. The rooms are connected by a vent hole of diameter 0.1 m. The length and the width of the inner room are 3 m each, and the height is 1 m. The outer room is 9 m in width and length, and 5 m in height. The rooms are separated by a wall of 0.5 m thickness. The vent hole is located at the center of roof of the inner room. All the walls are assumed to be adiabatic free-slip walls. A cylindrical explosive is placed on floor of the inner room directly below the vent hole. The explosive charge is 22.86 cm in height and 2.286 cm in radius. Small perturbations are introduced on the initial charge surface to mimic the natural surface imperfections and induce hydrodynamic instabilities. The two-room configuration is discretized using 44 million computational cells. The minimum size of the computational cell is set to 0.6 mm and the cells are distributed in the domain to resolve all the relevant flow features.

The explosive material composed of HMX with inert metal particles. The number of metal particles in the charge is 0.5 million, and the radius of each particle is 20 micrometers. Therefore, the volume fraction of charge is about 4.46×10^{-5}. In addition, the 0.1 million spore particles are placed at the corner of the inner room. They are also treated as inert particles. The radius of each spore is 30 micrometers.

Unlike the procedure developed earlier [73, 74], the initial blast wave is not modeled based on the one-dimensional detonation profile but is generated by the full three-dimensional detonation propagation through the condensed phase charge. To achieve this, a high pressure zone is placed at the center of the explosive charge and a detonation is allowed to propagate in axial direction of the charge. The detonation is is expected to reach the top and the bottom of the charge. Thus, the simulation accounts for a wide range of length and time scales from the detonation (small scale) to the blast wave propagation (large scale).

An Eulerian-Lagrangian method is used to solve the governing equations [73, 75]. A combination of Mie Gruneisen, Jones-Wilkins-Lee (JWL), and thermally perfect gas equations of state (EOS) are employed; the Mie Gruneisen EOS is applied in the regions with condensed phase charge, while Jones-Milkins-Lee EOS and thermally perfect EOS are used for gas phase detonation products and ambient air.

5.5.2 Results and Discussion

The chronology of evolution of the blast wave and the post-detonation mixing zone are shown in Fig. 5.41. The detonation of the initial charge, at t = 0.0, generates a high pressure and a high temperature zone at the center of the charge. The region of high temperature spreads in the axial direction behind the detonation. The hot gaseous products formed vent out in the radial direction out of the charge. Also, the particles in the charge are ejected but remain within the hot gases. At this stage, the particles acquire momentum and energy from the detonation product gases but due to inertia are slower than the detonation products.

At about $20\mu s$, the condensed phase explosive is completely consumed, resulting in the formation of the primary blast wave. The blast wave propagating towards the ground, reflects

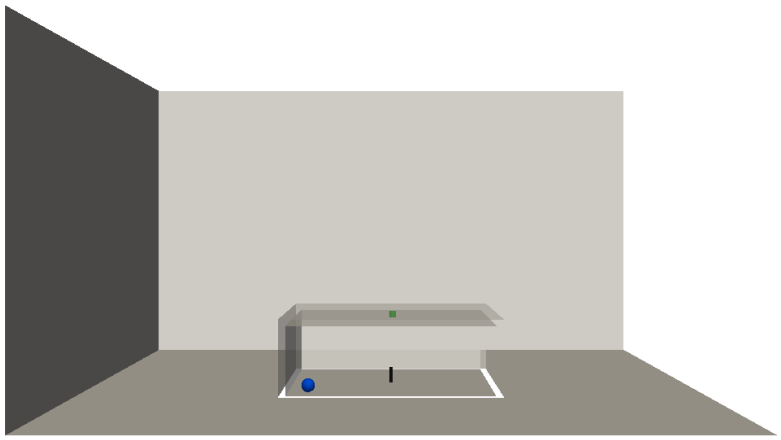

(a) Full view of the two rooms

(b) Enlarged view of the inner room

Figure 5.40: Geometry used for this simulation. Black cylinder: explosives, blue sphere: Spore particle, green cylinder: Vent hole connecting inner room and outer room

from the floor, and produces a wrinkled fireball near the floor (Fig.5.41 (c)). In addition, the particles penetrate the contact surface between the detonation products and the ambient air. As the particles overtake the contact, the particles induce additional perturbations i.e., in addition to that introduced by the imperfections on the initial charge surface. They are not significant in this phase, but affect the hydrodynamic instabilities, as is observed, at later stages.

At t = 0.3 ms, the blast wave eventually reaches the ceiling of the inner room and enters the outer room through the vent hole (Fig.5.41 (e)). The particles entrained into the mixing zone are also ejected into the outer room. The blast wave and the gaseous detonation products exhausted from the vent hole form a mushroom shaped structure(Fig.5.41 (f)). The constriction by the vent hole and the strength of the initial blast do not permit the fireball to expand into the outer room beyond the confines of the vent hole. In inner room, the temperature increases from 0.3 to 0.9 ms due to the compression wave generated to recover the over-expanded region at center of the inner room. Also, during this phase, the small perturbations that is introduced initially or added by penetrations of particles develop and add significant asymmetric to the shape of the fireball. They are especially significant at the upper portion of the blast wave and the fireball.

Around 0.9 ms, the primary blast wave hits and reflects from side wall/ceiling. The reflected blast waves interacts with the detonation products and form complex hydrodynamic structures. In particular, the hydrodynamic instabilities due to RMI and RTI occur at the location at which the reflected shock wave encounters the surface of detonation products. When the blast wave contacts to the spore particles, spore particle cloud is deformed along the contact surface of the shock. The spores are driven towards the wall, and pushed onto the corner of the inner room (Fig.5.41 (h)) with relatively higher gaseous temperature.

5.6 Multi-Blast Wave Interactions

Interaction of multiple blast waves can be used to direct energy toward a target while simultaneously reducing collateral damage away from the target area. In [3], authors simulate multiple point source explosives and the resulting shock interaction and coalescence behavior were explored. Different munitions were placed concentrically around the target. Different patterns are found and particularly, a strong linear behaviour is observed.

5.6.1 Two Blast Wave Sources

To study the interaction of two blast waves, we mimic the set up from [3]. In this study, researchers used a parrallel finite difference solver on overlapping grids to solve the Euler equations with shock capturing second order Godunov Scheme. They use adaptative mesh refinement method to reduce the CPU cost of the simulations. Taylor similarity laws [76] for pressure, density and velocity are used to initialize the blast spot. Different setups are presented to show interaction of blast waves in a 2D domain. In particular, the study focused on the interaction af blast waves placed around a target point, when all the munitions detonate initially at the same time. In the present study, the similar simulations are going to be compared to these reference cases.

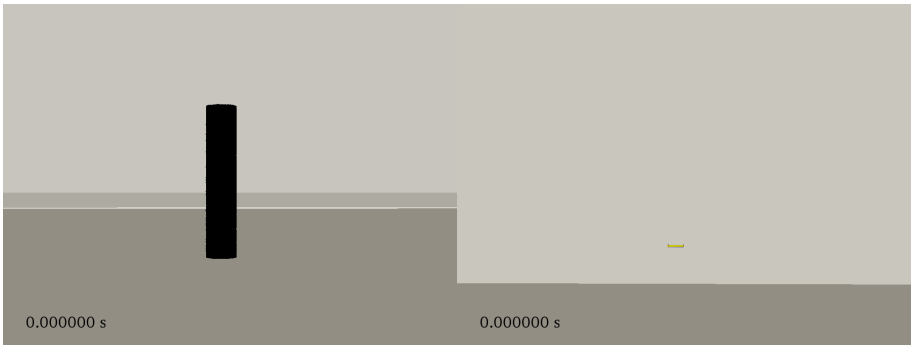

(a) $t = 0\mu s$

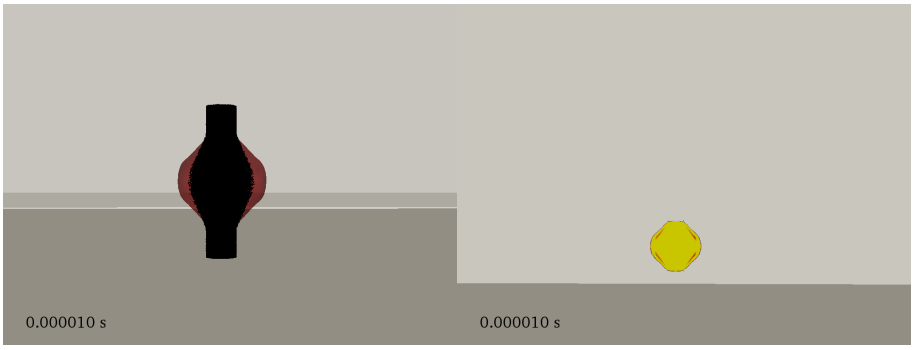

(b) $t = 10\mu s$

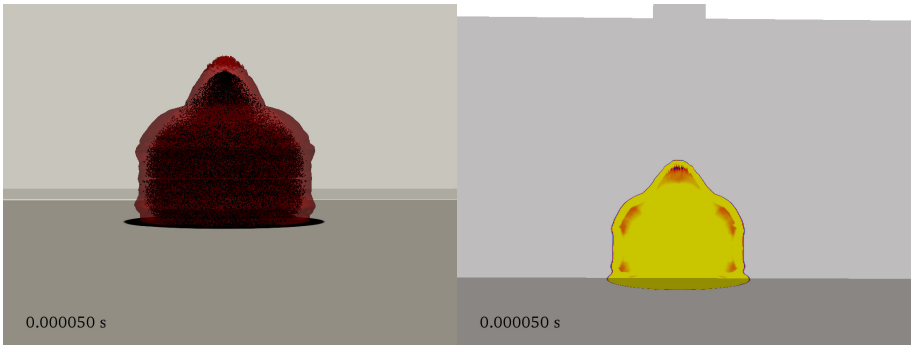

(c) $t = 50\mu s$

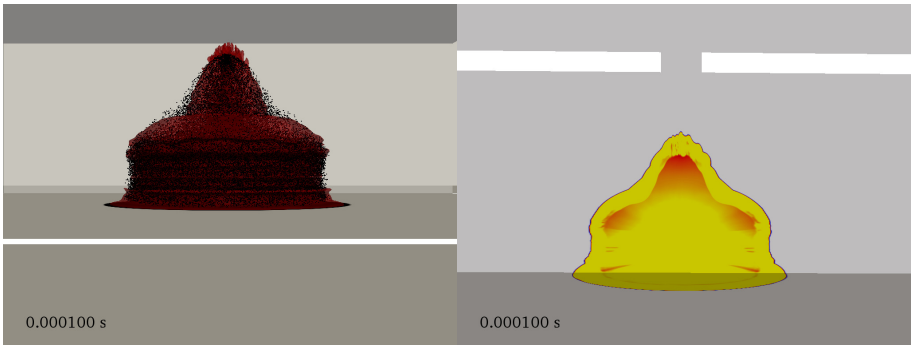

(d) $t = 0.1ms$

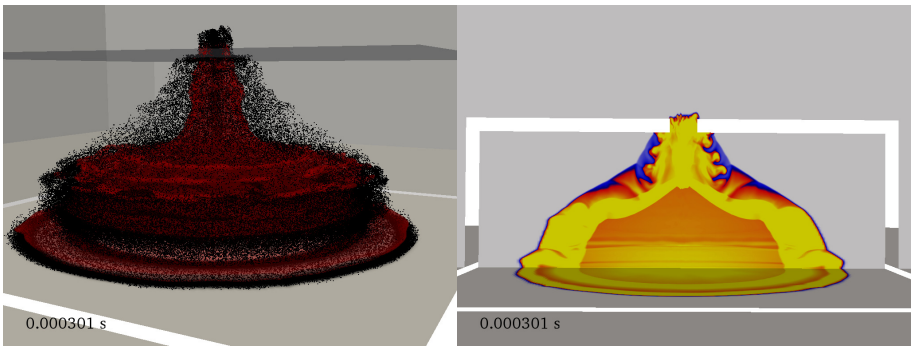

(e) $t = 0.3ms$

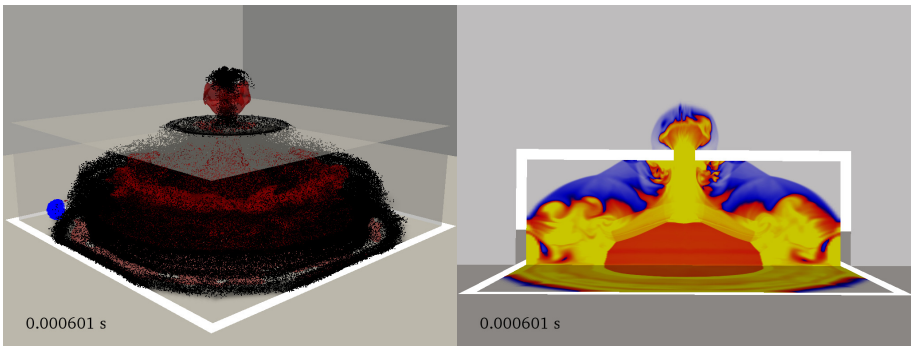

(f) $t = 0.6ms$

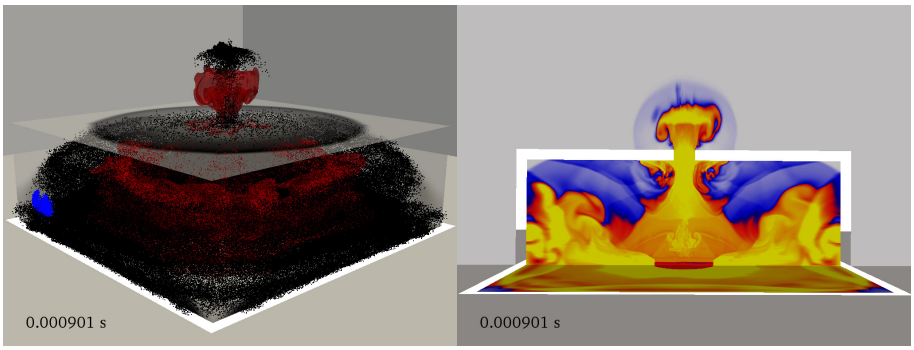

(g) $t = 0.9ms$

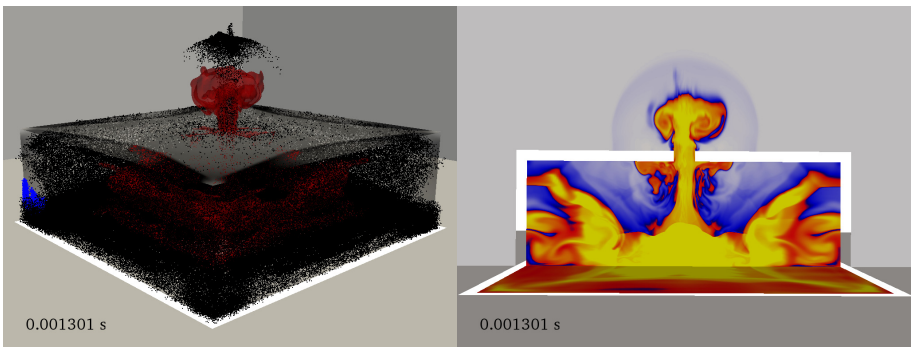

(h) $t = 1.3ms$

Figure 5.41: Formation and Evolution of blast wave. Left: Particles dispersion with iso-surface of detonation products. Right: Temperature profiles(min: 300 K, max: 2100 K.)

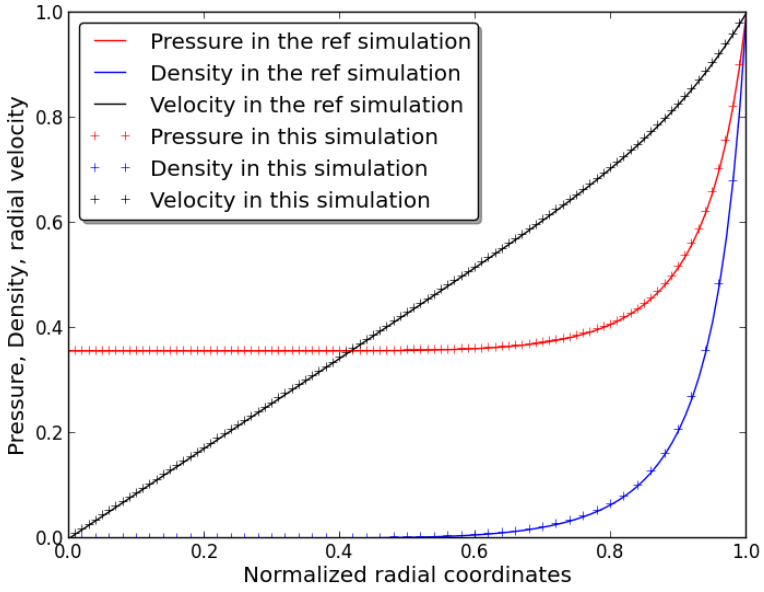

Figure 5.42: Taylor profiles for pressure, density and velocity : our current simulation initialization is similar with the reference one

The Taylor similarity laws are used to initialize the profiles of pressure, density and velocity inside the blast wave initially. A comparison of the profiles used in the reference simulations by [3] and the current simulations are shown in Fig. 5.42. While the velocity behaves quasi linearly inside the blob, density and pressure have an exponential trend, with maximum value at the external edge of the blast wave. Note that our current simulations use a similar initialization compared to the reference ones.

The evolution of two blast waves is necessarily the same for both waves until both pressure front interact. If the shock is weak, the interaction is pretty straightforward, and can be schematised with Fig. 5.43 a). Indeed, in this case, both waves behave like they do not see each other. Note that this no interaction case has been simulated in the present work, but the results are not shown. If the pressure front is strong enough, non linear interaction occurs (Fig. 5.43 b)). At this point, the spherical shape of the blast waves is lost. This result has been reproduced in the current simulation in Fig. 5.43 c). In this case, the oval interaction zone is not present, and a similar diamond shape appeared.

5.6.2 Blast wave inside a box

The outflow conditions that were used to avoid reflections at the boundaries are now removed, and no slip walls are used. The goal is to see the reflection of the blast wave at the boundary. The initialisation is exactly the same in the case: pressure, density and velocity profiles are specified inside a 1.5 mm blob inside the 2D domain. Pressure fields at different times are presented in Fig.5.45. Note that as the pressure amplitude is decreasing with time, each pressure field has been rescaled to see the pressure front.

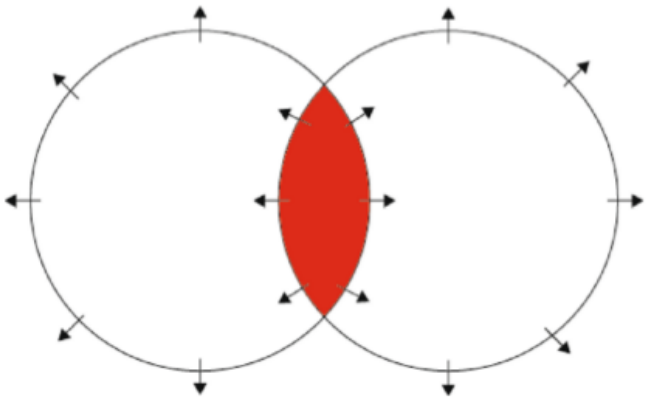

(a) Schematic from [3]

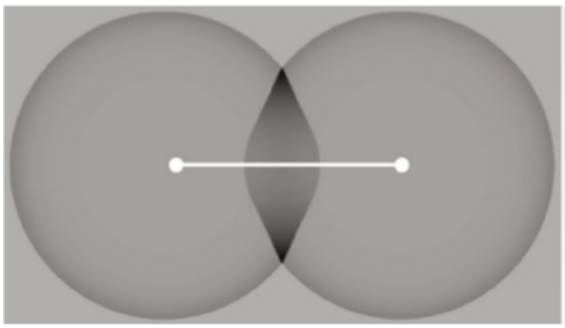

(b) Simulation from [3]

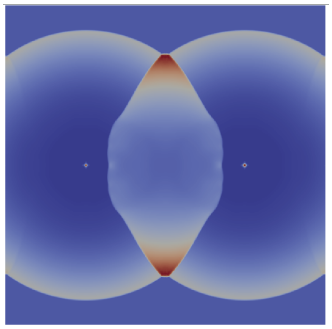

(c) Current simulation

Figure 5.43: Qualitative comparison of two blast waves interaction : Schematic of 2 blasts wave interaction, comparison between the simulation from [3] and our simulation : our work is able to capture a non linear behaviour

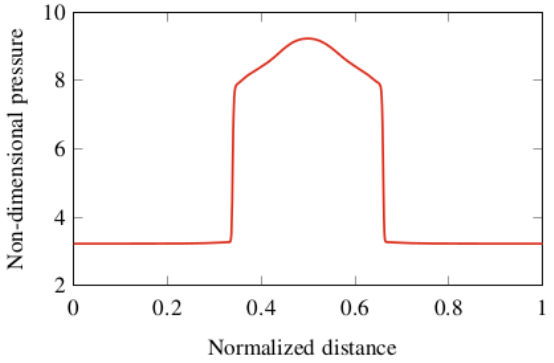

(a) From [3]

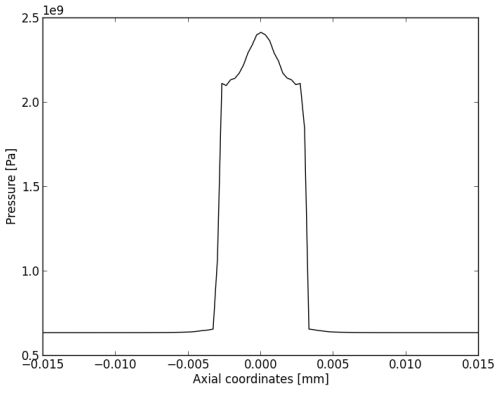

(b) Actual profiles

Figure 5.44: Pressure profile from the blast wave origins

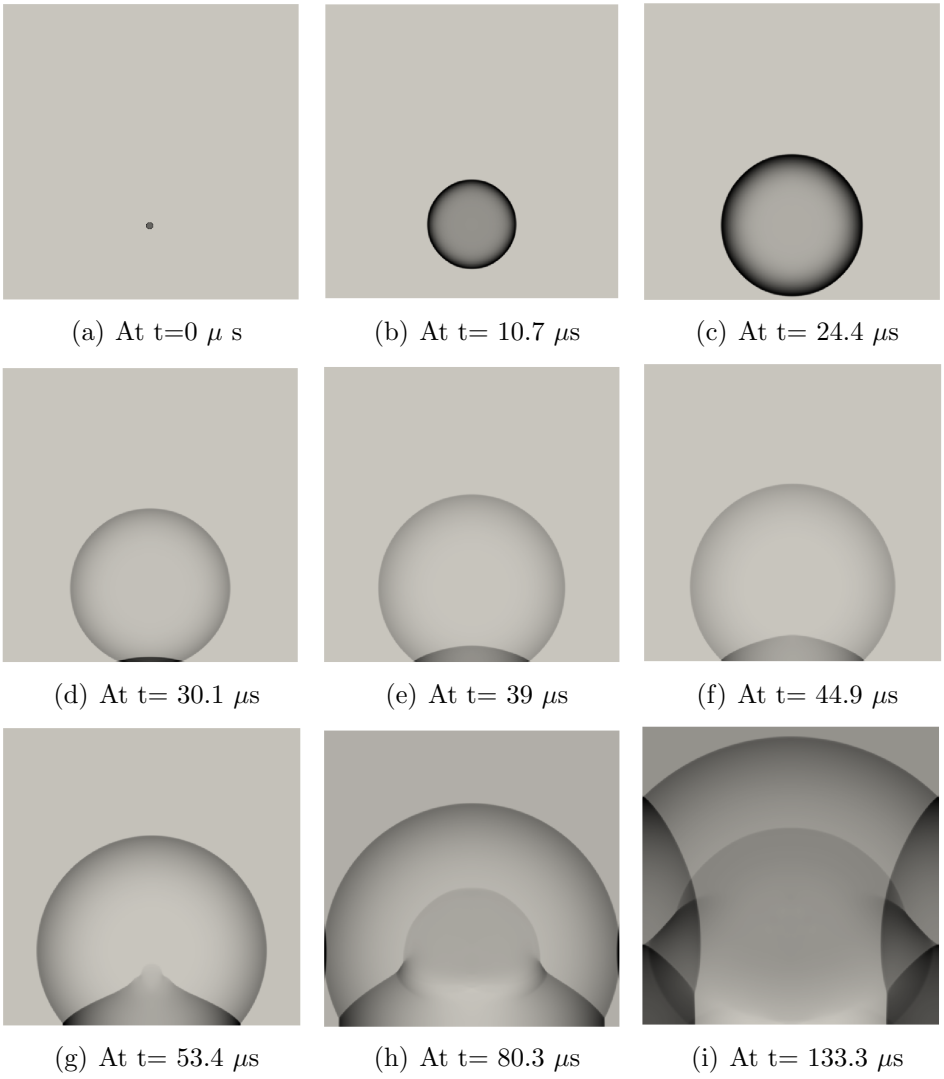

(a) At t=0 μ s (b) At t= 10.7 μs (c) At t= 24.4 μs

(d) At t= 30.1 μs (e) At t= 39 μs (f) At t= 44.9 μs

(g) At t= 53.4 μs (h) At t= 80.3 μs (i) At t= 133.3 μs

Figure 5.45: Pressure fields with time : the blast wave evolves with a spherical shape until it reaches a wall. At this point, reflection occurs, and interaction happens

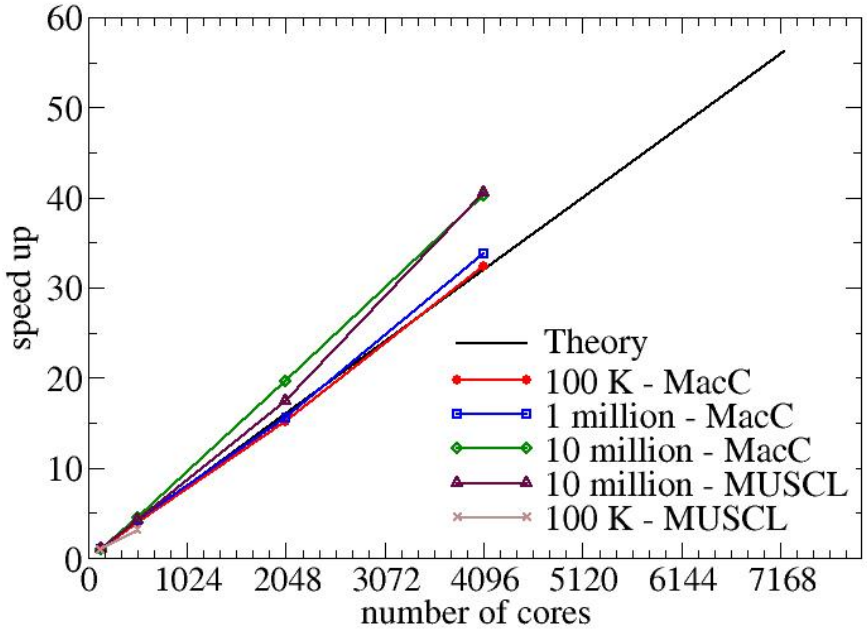

Figure 5.46: Speed up for the LESLIE Solver

From Fig.5.45 a) to c), the evolution of the blast wave is very classical : the blast wave evolves with a spherical shape. Then a part of the pressure contour reaches the boundary, which reflects the blast wave inside the domain in Fig.5.45 d) and e). At this point, the shape of the shock front is still spherical. Then, a non linear behaviour occurs : the spherical shape of the blast wave disappeared, and a cusp point appeared at the center (Fig.5.45 f) and g)). This modified blast wave interacts then with a secondary blast wave (Fig. 5.45 h)). Finally, the primary blast wave interacts with the other walls and corners to create a much more complex shape.

5.7 Performance and Scaling Analysis

As explained earlier in this report, the Lagrangian simulation for dense clouds can be very expensive in terms of CPU cost because of the high number of particles it needs to solves. That is why the use of an Eulerian solver for the dense phase coupled with the Lagrangian Solver for the dilute phase is crucial for a big range of mass loading. For the Lagrangian Solver, Fig.5.46 shows the speed up properties of the code for different numerical schemes and different number of particles. Performance drops when the number of particles increases. Note that Mac means MacCormack scheme.

5.8 Multi-scale Modeling of Condensed Phase Detonation

Blast waves are typically initialized using well-known one-dimensional detonation profiles that have been validated against experimental observations. While this assumption is valid for cases of one-dimensional nature, for example the explosion of a spherical homogeneous charge, it does not account for properties pertaining to the condensed phase energetic material. The shape of the explosive, as well as its structural and chemical composition, can have significant implications on the characteristics of the formed blast wave, including its speed, dispersion, and level of instability. For example, a randomly packed energetic material develop turbulent breakdown early in the process due to the seemingly perturbed energy depositions. Variations at the stage of the transition to detonation can develop and grow to produce outcomes that would otherwise be unexpected. Recent advancements in the field enable such simulations to be initialized with the unburnt condensed phase material to better predict the blast wave[77, 78]. The procedure introduces the advantage of quantifying uncertainties in terms of the explosive content, binder material, and granularity. By doing so, the approach better predicts blast wave characteristics, thus isolating the uncertainty quantification of the numerical models while taking into account the stochastic nature of the physical problem.

In summary, it is necessary to address this multi-scale problem starting with the unburnt condensed phase explosive for the following 3 main reasons:

1. The simulation better predicts the blast wave characteristics, such as speed, shape, and dispersion, based on the explosive's properties.

2. The perturbations at the micro-scale develop early turbulent breakdown and mixing that may have significant implications on the outcome.

3. The results are based on the stochastic nature of the condensed phase enabling a better quantification of the uncertainties arising from the numerical modeling.

5.8.1 Formulation of the Equation of State

The Mie-Grüneisen equation of state (EOS) is generally accepted to perform well with solid energetic materials [79, 80]. Its validity extends beyond the detonation wave front and reaction zone to the point where the expanding products reach a lower density at which the Mie-Grüneisen EOS starts to deteriorate [79]. At this point, another equation of state, which is introduced in a later section, is needed for the proper resolution of the evolution of the gaseous products. The Mie-Grüneisen EOS is expressed as:

$$e\left(P,\nu\right)=\frac{\nu}{\mathcal{G}}\left[P-f\left(\nu\right)\right]+e_0 \tag{5.6}$$

where

$$
\begin{aligned}
f(\nu) &= P_{\mathcal{H}}\left[1-\frac{\mathcal{G}}{2\nu}(\nu_0-\nu)\right]-\frac{\mathcal{G}}{2\nu}P_0(\nu_0-\nu)\\
P_{\mathcal{H}} &= P_0+\frac{\rho_0 c_0 \eta}{(1-s\eta)^2};\\
\eta &= 1-\frac{\nu}{\nu_0}
\end{aligned}
\tag{5.7}
$$

The specific volume and the pressure along the Hugoniot are herein represented by ν and $P_{\mathcal{H}}$, and s is defined as the slope in the relationship between the shock speed and the particle velocity, where $U_s = c_0 + s\,U_p$.

To allow for the formation of a blast wave, the detonation front propagates the entire condensed domain and gets released into a gaseous surrounding atmosphere, Air. One of the challenges facing the complete simulation of such problems is the proper handling of the thermodynamic properties. On one hand, the Mie-Grüneisen equation of state is successfully used to handle the high density phase of the domain. On the other hand, it rapidly deteriorates as the density of the expanding detonation products falls below the reference density used, ρ_0. For the surrounding air at atmospheric conditions, it can be treated using the ideal gas equations. As for the stage in between, the Jones-Wilkins-Lee (JWL) equation of state seems to be adequate as it has been developed for such purposes. The JWL equation of state has been used in numerous studies to calculate the thermodynamic properties of detonation product. It is expressed as:

$$
P(e,\rho) = A\left(1-\frac{\omega\rho}{R_1\,\rho_0}\right)\exp\left[\frac{-R_1\,\rho_0}{\rho}\right]+B\left(1-\frac{\omega\rho}{R_1\,\rho_0}\right)\exp\left[\frac{-R_2\,\rho_0}{\rho}\right]+\omega\rho\,(e-e_0) \tag{5.8}
$$

The complete simulation of the shock to detonation transition until after the formation of a blast wave requires the use of all three equations of state. The combination of the equations of state is implemented in terms of the density of the products, where density limits are specified to denote the regions of transition. For expanding products with densities higher than the upper limit of the condensed phase ρ_{CU}, the Mie-Gruneisen equation of state is used, whereas JWL is used when it drops below the lower limit ρ_{CL}. A smoothing function is used for the range in between. A similar procedure is used for the transition between JWL and ideal gas equations using upper and lower density limits ρ_{GU} and ρ_{GL}. The resulting expression takes the following form:

$$
x = \begin{cases}
x_{\mathrm{MG}} & \rho \geq \rho_{CU}\\
(x_{\mathrm{MG}} - x_{\mathrm{JWL}})\,\dfrac{\rho-\rho_{CL}}{\rho_{CU}-\rho_{CL}} & \rho_{CL} \leq \rho < \rho_{CU}\\
x_{\mathrm{JWL}} & \rho_{GU} \leq \rho < \rho_{CL}\\
(x_{\mathrm{JWL}} - x_{\mathrm{IG}})\,\dfrac{\rho-\rho_{GL}}{\rho_{GU}-\rho_{GL}} & \rho_{GL} \leq \rho < \rho_{GU}\\
x_{\mathrm{IG}} & \rho < \rho_{GU}
\end{cases}
\tag{5.9}
$$

where x represents thermodynamic variables. Figure 5.47 compares $P-\nu$ plots for the three equations of state alongside the combined equation for HMX at 5000 K. The density limits are chosen in such a way to smoothen the transition. For this case, ρ_{CU}, ρ_{CL}, ρ_{GU}, and ρ_{GL} are

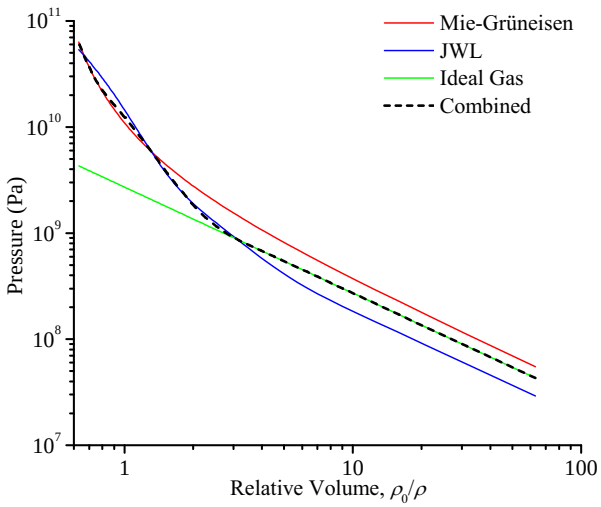

Figure 5.47: $P - \nu$ plot for the combined equation of state with respect to the Mie-Grüneisen, JWL and ideal gas equations of state.

2500 kg/m^3, 1000 kg/m^3, 1000 kg/m^3, and 500 kg/m^3, respectively. The transition from the condensed phase to the expanded blast wave products is very rapid, and therefore, variations in the density limits have negligible effects on the resulting blast wave characteristics. Figure 5.47 shows a smoothened transition from the MG to IG through the JWL equation of state.

5.8.2 Simulations Setup

The purpose of this study is to investigate the effects of the micro-structure of the condensed phase explosive on the resulting blast wave. The simulations consider modifications in the condensed phase that are typically ignored in blast wave studies. Three cases are addressed using charges in the shape of a flat plate. The shape introduces two-dimensionality effects that can change the dynamics of the blast wave, as seen in experiments [81]. The first case consists of a homogeneous HMX charge being initiated with a strong cylindrical shock through its middle section, as shown in Fig. 5.48(a). The shock represents an initiation similar to that produced by a detonator. The yellow color denotes the energetic material and the blue part is air. The red half-circle shows the location of the initiating shock. In Fig. 5.48(b), the second case uses the same setup but using a Polymer-Bonded Explosive (PBX) with randomly packed HMX crystals in an Estane binder. Being more realistic, the case includes the natural perturbations in the energetic material to study their effects on the blast wave formation. The last case also makes use of the same PBX, however, the initiating shock is located on the top portion of the charge at a part in contact with air. Moreover, the shock strength is tremendously reduced, and uses a hot spot to aid in the ignition, and it is referred to as the weak-shock case.

5.8.3 Results and Discussion

Figure 5.49 shows the velocity contour plots at 3.6 μs. At this point, detonation waves form and propagate through the energetic material. When comparing the 3 cases, the detonation

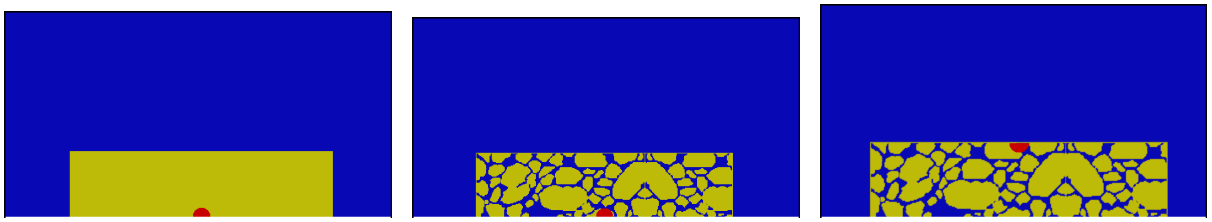

(a) Homogeneous HMX (b) PBX-Strong shock (c) PBX-Weak shock

Figure 5.48: Diagrams of the initial setup. The HMX material is represented by the yellow color and Air is in blue. In the cases with PBX, the HMX cystals are embedded in Estane as the binder.

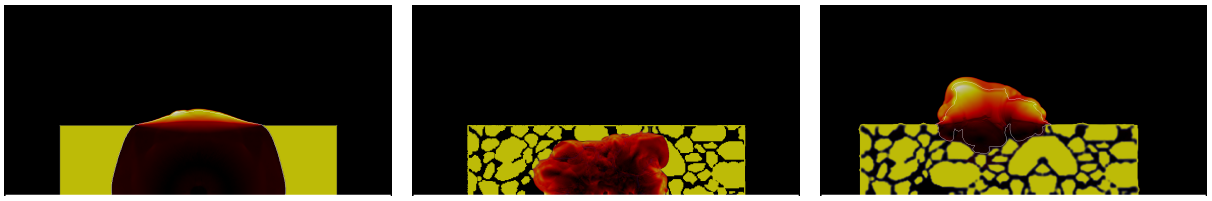

(a) Homogeneous HMX (b) PBX-Strong shock (c) PBX-Weak shock

Figure 5.49: Shape of the detonation waves at 3.6 μs. The PBX cases show more perturbations in the wave due to the irregularities in the HMX crystals packing.

wave in the homogeneous case has traveled a bigger portion of the charge. It has made its way out of the material at the middle top part where the blast wave starts forming. The overall shape of the wave assumes a smooth edge all around. Looking at the PBX case in Fig. 5.49(b), the detonation front is irregular, and has yet to travel the height of the charge. As for the weak-shock case, the blast wave starts forming as the products eject into air while the detonation wave burns through the charge. When compared to the other cases, the amount of the burnt part of the slab is noticeably less.

The velocity contour plots for the 3 cases are shown in Fig. 5.50 at 46 μs at which time the material is completely burnt. The wave front of the homogeneous HMX has progressed more than the other cases. This is expected since the binder not only occupies room in the slab thus reducing the total amount of HMX, but its reaction is also endothermic, which draws energy from the reacted energetic material . Figure 5.50(a) also shows a smooth symmetrical structure of the propagation. While for the PBX cases, an irregular and asymmetric behavior forms.

Looking at the progress of the fireball in Fig. 5.51, the expansion of products fall behind the blast wave front. The homogeneous case demonstrates a symmetric expansion, similar to what is routinely used in the simulation of blast waves. However, when examining the PBX cases, an asymmetric random structure emerges. The front of the product expansion exhibits finger-like instabilities as seen in experiments. Its justification stems from the initial random distribution of crystals at the micro-structure. It is interesting to note that although the weak-shock case is the first to develop a blast wave due to the location of the initiating shock, its progress is the most retarded. The tardiness of the PBX cases is better justified when examining the degree of mixing and CO_2 generation in a later discussion.

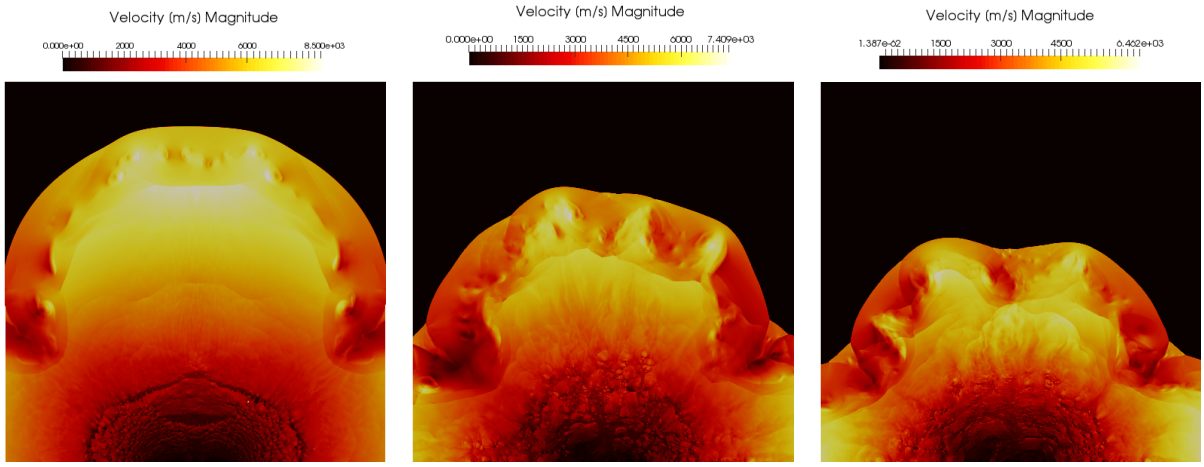

(a) Homogeneous HMX (b) PBX-Strong shock (c) PBX-Weak shock

Figure 5.50: Shape of the blast waves at 46 μs. The blast from the homogeneous case is at a more advanced stage while the PBX cases show more irregular shapes.

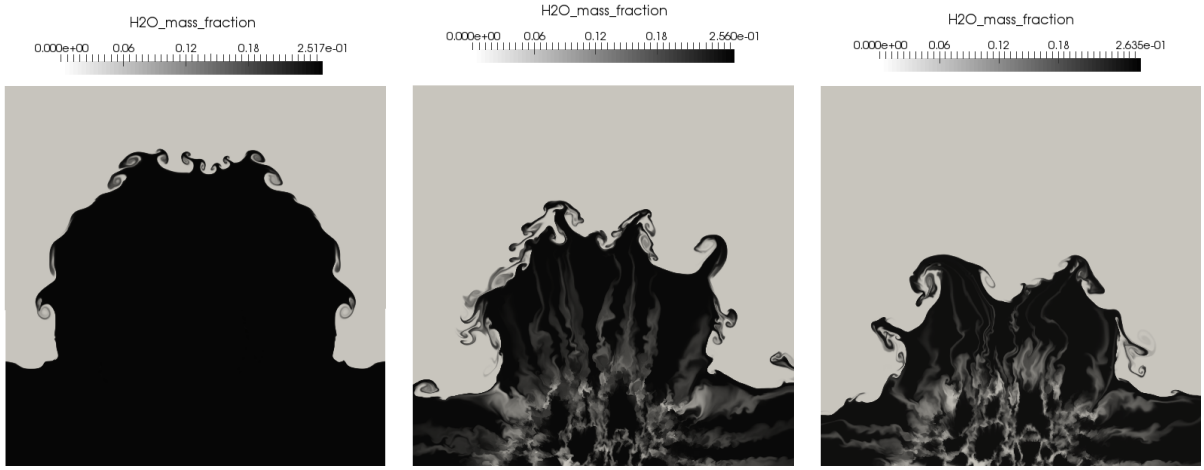

(a) Homogeneous HMX (b) PBX-Strong shock (c) PBX-Weak shock

Figure 5.51: Dispersion of products at 46 μs. The PBX cases show more prominent instability structures due to the irregularities in the initial packing at the micro-scale.

(a) Homogeneous HMX (b) PBX-Strong shock (c) PBX-Weak shock

Figure 5.52: CO_2 mass fraction at 46 μs. Although the homogeneous case is at a more advanced stage, the higher generation of CO_2 in the PBX cases is indicative of the higher rate of mixing.

Two-dimensional plots of the CO_2 mass fraction are provided in Fig. 5.52. The generation of carbon dioxide is the result of the afterburn, such that:

$$2CO + O_2 \rightarrow 2CO_2$$

Since its generation is the outcome of the interaction of the reaction products with air, the CO_2 mass fraction can be a good indicative of the level of mixing and turbulence of the expanding cloud. The initial perturbations in the PBX cases stir the flow to develop more mixing and therefore generate more CO_2. The after-burn takes place at the front of the expanding products which can be the reason behind the name "fireball".

The degree of mixing is a good measure of the level of turbulence and mixing of the reaction products with the surrounding air. For this simulation, the degree of mixing can be defined by:

$$\text{Degree of Mixing} = \frac{V_{\text{mixed products}}}{V_{\text{fireball}}} = \frac{\int \left(Y_{H_2O}\right)\left(Y_{O_2} + Y_{CO_2}\right)\ dV}{\int Y_{H_2O}\ dV} \tag{5.10}$$

Figure 5.53(a) compares the time evolution of the degree of mixing of the 3 cases. In the initial phases, it may seem that the weak-shock case has the most mixing, however, this is because of the location of the initiating shock giving the ejecta a head start over the other cases. While the PBX with strong shock is the latest to start mixing with air, the higher speeds along with the initial perturbations develop stronger mixing.

Another aspect of interest is a length-scale that compares the progress of the blast wave to that of the expanding products. This length-scale is a measure of the distance between the blast wave front and products front and is labeled here as the blast wave thickness. One way to compute it, and to work around the asymmetric behavior, is to compute the volume covered by the blast wave and subtract the volume covered by the reaction products. Plotted in Fig. 5.53(b), the higher thickness signifies a faster progress of the blast wave over

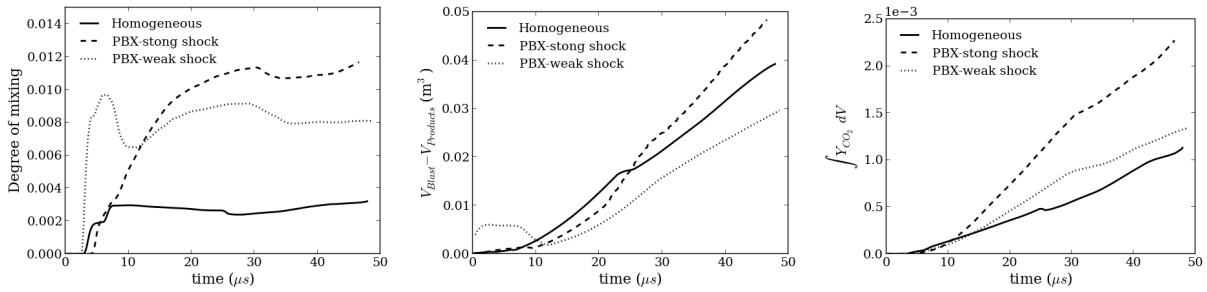

(a) Degree of Mixing (b) Blast wave thickness (c) Generation of CO2

Figure 5.53: Comparison of the evolution of a) Degree of mixing, b) blast wave thickness, and c) CO_2 generation with time between the homogeneous HMX, PBX with strong shock, and PBX with weak shock initiation.

the products. The comparison shows that the case with PBX and strong shock initiation has the largest thickness as the flow progresses. This is attributed to the larger degree of mixing seen by these products which contributes to a slower expansion. As for the PBX with weak-shock initiation, the initial jump is the progress of a shock rather than a blast wave which has yet to reach the hot spot and ignite. However, after ignition, the progress of the product expansion is closer to the blast wave front, when compared to the other cases, possibly due to the lower speeds that this case is undergoing.

Lastly, a comparison of the time evolution of the CO_2 generation is plotted in Fig. 5.53(c). The second case shows a significantly higher rate of carbon dioxide generation. Also related to the higher levels of mixing, the initial random packing, along with the strong shock, develop a turbulent breakdown earlier in the simulation. Although the homogeneous HMX case has progressed the most at this time, it has the least amount of instabilities and therefore CO_2 generated.

CHAPTER VI

CONCLUSIONS AND METRICS

6.1 Conclusions

Under this project a new multi-scale simulation capability was developed and demonstrated for varied applications of DTRA's interest. It is noted that this effort required leveraging other funding and man power funded under Basic Rsearch 6.1 programs of DTRA and ONR but the combined effort has established a new simulation tool that can be deployed for many complex problems. Preliminary validation of the two-phase solver and its ability are reported in this final report. Additionally, some of the subgrid models were transitioned to our collaborators under this FRBAA (CRAFT Tech) and they have successfully applied their code to problems of specific interest to DTRA. A detailed report summarizing their effort has already been submitted to DTRA in early 2016.

The multi-scale simulation capability developed in this effort is being further applied to other applications of related interest. The predictive capability of this solver still requires further investigation by applying it to new problems and such studies will be considered in the near future.

6.2 Metrics

6.2.1 Publications

The following publications were supported

1. Menon, S. and Gottiparthi, K. C., "Detonation in Multi-room Structure," Video provided to DTRA for presentation, Aug 2015.

2. Fedina, K, Gotiparthi, K. C., Fureby, C, and Menon, S., "Combustion in Afterburning Behind Explosive Blasts," in Coarse Grained Turbulent Mixing (Fernando, E., Ed.), Cambridge University Press, 2016 (in press).

3. Gottiparthi, K. C., Schulz, J. C., and Menon, S., "On the Neutralization of Bacterial Spores in Post Detonation Flows," Shock Waves, Vol. 24, pp. 455-466, 2014.

4. Gottiparthi, K. C., Schulz, J. C., and Menon, S., "Uncertainty Quantification of Bacterial Aerosol Neutralization in Shock Heated Gases," Shock Waves, Vol. 25, pp. pp. 77-90, 2015.

5. Menon, S., "Turbulent Mixing and Afternburn in Post-Detonation Flow with Dense Particle Clouds." Invited Paper, 19th Biennial Conference of the APS Topical Group on Shock Compression of Condensed Matter, June 2015 (to appear, 2016).

6.2.2 Students and Staff

During the course of this project the following people were supported in Georgia Tech during the period June 2011 - June 2016:

1. Post Doctoral Fellows: 2 (partial support over 2-3 years)
    - Dr. Michel Akiki
    - Dr. Gregory Hannebique
2. Ph.D. Students: 2 (co-shared with another DTRA project)
    - Joseph Schulz, 2015: A Study of Magnetohydrodynamic effects in turbulent supersonic flows with application to detonation and explosion
    - Kalyana Gottiparthi, 2015: A Study of Dispersion and Combustion of Particle Clouds in Post Detonation Flows
3. M.S. Students (without thesis): 1
    - Yusuke Nagaoke, July 2015
4. Undergraduate Student Special Topic: 2

Bibliography

[1] V. M. Boiko, V. P. Kiselev, S. P. Keselev, A. P. Papyrin, S. V. Poplavsky, and V. M. Fomin. Shock wave interaction with a cloud of particles. *Shock Waves*, 7:275–285, 1997.

[2] X. Rouge, G. Rodriguez, J. F. Haas, and R. Saurel. Experimental and numerical investigation of the shock-induced fluidization of a particle bed. *Shock Waves*, 8:29–45, 1998.

[3] S Qiu and Eliasson V. Interaction and coalesence of multiple simultaneous and non-simulatenaous blast waves. *Shock Waves*, 2015.

[4] S. Pascaud, M. Boileau, B. Cuenot, and T. Poinsot. Large eddy simulation of turbulent spray combustion in aeronautical gas turbines. In *ECCOMAS Thematic Conference on computational combustion*, pages 149–167, 2005.

[5] Y. Renardy. Effect of startup conditions on drop breakup under shear with inertia. *Int. J. of Multiphase Flow*, 34:1185–1189, 2008.

[6] M. Boileau, S. Pascaud, E. Riber, B. Cuenot, L. Gicquel, and T. Poinsot. Investigation of two-fluid methods for large eddy simulation of spray combustion in gas turbines. *Flow Turbulence Combust.*, 80:351–373, 2008.

[7] R. Lebas, T. Menard, P. A. Beau, A. Berlemont, and F. X. Demoulin. Numerical simulation of primary break-up and atomization: DNS and modelling study. *Int. J. of Multiphase Flow*, 35:247–260, 2009.

[8] E. Riber, V. Moureau, M. García, T. Poinsot, and O. Simonin. Evaluation of numerical strategies for large eddy simulation of particulate two-phase reacting flows. *J. Comp. Phys.*, 228:539–564, 2009.

[9] J. M. Desantes, J. V. Pastor, J. M. Garciá-Oliver, and J. V. Pastor. A 1D model for the description of mixing-controlled reacting diesel sprays. *Combust. Flame*, 156:234–249, 2009.

[10] J. M. Senoner, M. Sanjosé, T. Lederlin, F. Jaegle, M. Garćia, E. Riber, N. Cuenot, L. Gicquel, H. Pitsch, and T. Poinsot. Eulerian and lagrangian large-eddy simulations of an evaporating two-phase flow. *C. R. Mecanique*, 337:458–468, 2009.

[11] M. Sanjosé, E. Riber, L. Gicquel, B. Cuenot, and T. Poinsot. Large eddy simulation of a two-phase reacting flow in an experimental burner. In *Direct and Large-Eddy Simulation VII*, pages 345–351. Springer, 2010.

[12] S. Hank, R. Saurel, and O. L. Metayer. A hyperbolic Eulerian model for dilute two-phase suspensions. *J. Modern Phys.*, 2:997–1011, 2011.

[13] W. Kollmann and I. M. Kennedy. Les model for the particulate phase in sprays. *AIAA 97-0369*, pages 1–11, 1997.

[14] D. Caraeni, C. Bergström, and L. Fuchs. Modeling of liquid fuel injection, evaporation and mixing in a gas turbine burner using large eddy simulations. *Flow Turbulence Combust.*, 65:223–244, 2000.

[15] V. Sankaran and S. Menon. Vorticity-scalar alignments and small-scale structures in swirling spray combustion. *Proc. Combust. Inst.*, 29:577–584, 2002.

[16] S. James, J. Zhu, and M. S. Anand. Large-eddy simulation as a design tool for gas turbine combustion systems. *AIAA J.*, 44:674–686, 2006.

[17] S. Menon and N. Patel. Subgrid modeling for simulation of spray combustion in large-scale combustors. *AIAA Journal*, 44:709–723, 2006.

[18] M. Kirtas, N. Patel, V. Sankaran, and S. Menon. Large-Eddy Simulation of a Swirl-Stabilized, Lean-Direct Injection Spray Combustor. *Proceedings of ASME GT2006 (Barcelona, Spain)*, GT 2006-91310, 2006.

[19] S. B. Kuang, A. B. Yu, and Z. S. Zou. A new point-locating algorithm under three-dimensional hybrid meshes. *Int. J. of Multiphase Flow*, 34:1023–1030, 2008.

[20] Y.-W. Yan, J.-X. Zhao, J.-Z. Zhang, and Y. Liu. Large-eddy simulation of two-phase spray combustion for gas turbine combustors. *Applied Thermal Engineering*, 28(11):1365–1374, 2008.

[21] T. Lederlin and H. Pitsch. Large-eddy simulation of an evaporating and reacting spray. In *Center for Turbulence Research: Annual Research Briefs*, pages 479–490, 2008.

[22] K. Luo, H. Pitsch, and M. G. Pai. Direct numerical simulation of three-dimensional swirling n-heptane spray flames. In *Center of Turbulence Research Annual Research Briefs*, pages 171–183, 2009.

[23] J. Pozorski and S. V. Apte. Filtered particle tracking in isotropic turbulence and stochastic modeling of subgrid-scale dispersion. *International Journal of Multiphase Flow*, 35:118–128, 2009.

[24] K. Luo, H. Pitsch, M. G. Pai, and O. Desjardins. Direct numerical simulations and analysis of three-dimensional n-heptane spray flames in a model swirl combustor. *Proc. Combust. Inst.*, 33:2143–2152, 2011.

[25] S. Srinivasan, A. G. Smith, and S. Menon. Accuracy, reliability and performance of spray combustion models in LES. In *Quality and Reliability of Large-Eddy Simulations II*, pages 211–220. Springer, 2011.

[26] K. Li and L. X. Zhou. Studies of the effect of spray inlet conditions on the flow and flame structures of ethanol-spray combustion by large-eddy simulation. *Numerical Heat Transfer, Part A: Applications*, 62(1):44–59, 2012.

[27] B. Franzelli, Vié A., B. Fiorina, and N. Darabiha. Large eddy simulation of swirling kerosene/air spray flame using tabulated chemistry. *Proceedings of the ASME Turbo Exposition*, GT2006-90974:1–10, 2013.

[28] M. Chrigui, A. R. Masri, A. Sadiki, and J. Janicka. Large eddy simulation of a polydisperse ethanol spray flame. *Flow Turbulence Combust.*, 90:813–832, 2013.

[29] W. P. Jones, A. J. Marquis, and K. Vogiatzaki. Large-eddy simulation of spray combustion in a gas turbine combustor. *Combust. Flame*, 161:222–239, 2014.

[30] M. Arienti, X. Li, M. C. Soteriou, C. A. Eckett, and R. Jensen. Coupled level-set/volume-of-fluid method for the simulation of liquid atomization in propulsion device injectors. *AIAA 2010-7136*, pages 1–10, 2010.

[31] X. Li, M. Arienti, M. C. Soteriou, and M. M. Sussman. Towards an efficient, high-fidelity methodology for liquid jet atomization computations. *AIAA 2010-210*, pages 1–16, 2010.

[32] M. Mortensen and R. W. Bilger. Derivation of the conditional moment closure equations for spray combustion. *Combust. Flame*, 156:62–72, 2009.

[33] C. Laurent, G. Lavergne, and P. Villedieu. Quadrature method of moments for modeling multi-component spray vaporization. *Int. J. of Multiphase Flow*, 36:51–59, 2010.

[34] W. P. Jones, S. Lyra, and S. Navarro-Martinez. Large eddy simulation of a swirl stabilized spray flame. *Proc. Combust. Inst.*, 33:2153–2160, 2011.

[35] W. P. Jones, S. Lyra, and S. Navarro-Martinez. Numerical investigation of swirling kerosene spray flames using large eddy simulation. *Combust. Flame*, 159:1539–1561, 2012.

[36] A. Vié, S. Jay, B. Cuenot, and M. Massot. Accounting for polydispersion in the Eulerian large eddy simulation of the two-phase flow in an aeronautical-type burner. *Flow Turbulence Combust.*, 90:545–581, 2013.

[37] S. Elghobashi. On predicting particle-laden turbulent flows. *Appl. Sci. Res.*, 52:309–329, 1994.

[38] E. Loth. Numerical approaches for motion of dispersed particles, droplets and bubbles. *Prog Energy Combust Sci*, 26:161–223, 2000.

[39] S. Balachandar and J. K. Eaton. Turbulent dispersed multiphase flow. *Annual Review of Fluid Mechanics*, 42:111–133, 2010.

[40] O. A. Druzhinin and S. Elghobashi. Direct numerical simulations of bubble-laden turbulent flows using the two-fluid formulation. *Phys. Fluids*, 10:685–697, 1998.

[41] O. A. Druzhinin and S. Elghobashi. On the decay rate of isotropic turbulence laden with microparticles. *Phys. Fluids*, 11:602–610, 1999.

[42] J Réveillon, M Massot, and C Péra. Analysis and modeling of the dispersion of vaporizing polydispersed sprays in turbulent flows. In *Proceedings of the summer program*, pages 393–404, 2002.

[43] J. J. Riley and G. S. Patterson. Diffusion experiments with numerically integrated isotropic turbulence. *Phys. Fluids*, 17:292–297, 1974.

[44] K. Dukowicz, J. A particle-fluid numerical model for liquid sprays. *J. Comp. Phys.*, 35:229–253, 1980.

[45] M. R. Maxey. The gravitational settling of aerosol particles in homogeneous turbulence and random flow fields. *J. Fluid Mech.*, 174:441–465, 1987.

[46] S. Elghobashi. Particle-laden turbulent flows: direct simulation and closure models. *Appl. Sci. Res.*, 48:301–314, 1991.

[47] KC Gottiparthi and S Menon. A study of interaction of clouds of inert particles with detonation in gases. *Combust. Sci. Technol.*, 184(3):406–433, 2012.

[48] K. Balakrishnan and S. Menon. On the role of ambient reactive particles in the mixing and afterburn behind explosive blast waves. *Combustion Science and Technology*, 182(2):186–214, 2010.

[49] Clayton T Crowe, John D Schwarzkopf, Martin Sommerfeld, and Yutaka Tsuji. *Multiphase flows with droplets and particles*. CRC press, 2011.

[50] K. Balakrishnan and S. Menon. Characterization of the mixing layer resulting from the detonation of heterogeneous explosive charges. *Flow Turbululence and Combustion*, 87(4):639–671, 2011.

[51] M. R. Baer and J. W. Nunziato. A two-phase mixture theory for the deflagration-to-detonation transition (DDT) in reactive granular materials. *International Journal of Multiphase Flow*, 12(6):861–889, 1986.

[52] N. Patel and S. Menon. Simulation of spray-turbulence-flame interactions in a lean direct injection combustor. *Combust. Flame*, 153:228–257, 2008.

[53] M Bini and WP Jones. Particle acceleration in turbulent flows: A class of nonlinear stochastic models for intermittency. *Phys. Fluids*, 19:035104, 2007.

[54] S. Menon and N. Patel. Subgrid modeling for LES of spray combustion in large-scale combustors. *AIAA Journal*, 44(4):709–723, 2006.

[55] Franklin Génin and Suresh Menon. Studies of shock/turbulent shear layer interaction using large-eddy simulation. *Computers & Fluids*, 39(5):800–819, 2010.

[56] J. Smagorinsky. General circulation experiments with the primitive equations. *Monthly Weather Review*, 91(3):99–164, 1993.

[57] M. Germano, U. Piomelli, P. Moin, and W. H. Cabot. A dynamic subgrid-scale eddy viscosity model. *Physics of Fluids A*, 3(11):1760–1765, 1991.

[58] S. Menon and W.-W. Kim. High reynolds number flow simulations using the localized dynamic subgrid-scale model. *AIAA-96-0425*, 1996.

[59] W.-W. Kim and S. Menon. A new incompressible solver for large-eddy simulations. *International Journal of Numerical Fluid Mechanics*, 31:983–1017, 1999.

[60] W.-W. Kim, S. Menon, and H. C. Mongia. Large-eddy simulation of a gas turbine combustor flow. *Combustion Science and Technology*, 143:25–62, 1999.

[61] G. M. Faeth. Mixing, transport and combustion in sprays. *Progress in Energy and Combustion Science*, 13:293–345, 1987.

[62] S. Menon and S. Pannala. Subgrid modeling of unsteady two-phase turbulent flows. *AIAA Paper No. 97-3113*, 1997.

[63] Christer Fureby and S-I Möller. Large eddy simulation of reacting flows applied to bluff body stabilized flames. *AIAA J.*, 33(12):2339–2347, 1995.

[64] C. T. Crowe, M. Sommerfeld, and Y. Tsuji. *Multiphase Flows with Droplets and Particles*. CRC Press, Boca Raton, 1998.

[65] Kevin W Brinckman, William H Calhoon Jr, Stephen Mattick, Jeremy Tomes, and Sanford M Dash. Scalar variance model validation for high-speed variable composition flows. *AIAA Paper*, 715:2006, 2006.

[66] Srinivasan Arunajatesan and Neeraj Sinha. Hybrid rans-les modeling for cavity aeroacoutics predictions. *International Journal of Aeroacoustics*, 2(1):65–93, 2003.

[67] F Bataille and JP Bertoglio. Spectral study of weakly compressible turbulence. In *Australasian Fluid Mechanics Conference, 11 th, Univ. of Tasmania, Hobart, Australia*, pages 961–964, 1992.

[68] B. F. Magnussen and B. H. Hjertager. On mathematical modeling of turbulent combustion with special emphasis on soot formation and combustion. *Sixteenth Symposium (International) on Combustion*, pages 719–729, 1976.

[69] S. Byggstoyl and B. F. Magnussen. Model for flame extinction in turbulent flow. In *Turbulent Shear Flows 4*, pages 381–395. Springer-Verlag, 1988.

[70] Inge R Gran and Bjørn F Magnussen. A numerical study of a bluff-body stabilized diffusion flame. part 2. influence of combustion modeling and finite-rate chemistry. *Combustion Science and Technology*, 119(1-6):191–217, 1996.

[71] J Janicka and W Kollmann. A two-variables formalism for the treatment of chemical reactions in turbulent h2?air diffusion flames. In *Symposium (International) on Combustion*, volume 17, pages 421–430. Elsevier, 1979.

[72] William H Calhoon Jr, Kevin W Brinckman, Jeremy Tomes, Stephen Mattick, and Sanford M Dash. Scalar fluctuation and transport modeling for application to high speed reacting flows. In *AIAA Paper No. AIAA-2006-1452, 44th Aerospace Sciences Meeting and Exhibit, Reno, NV*, 2006.

[73] K. C. Gottiparthi, J. C. Schulz, and S. Menon. On the neutralization of bacterial spores in post-detonation flows. *Shock Waves*, 24:455–466, 2014.

[74] K. Balakrishman, F. Genin, D. V. Nance, and S. Menon. Numerical study of blase characteristics from detonation of homogeneous explosives. *Shock Wave*, 20:147–162, 2010.

[75] K. C. Gottiparthi and S. Menon. A study of interaction of clouds of inert particles with detonation in gases. *Combustion Science and Technology*, 184:406–433, 2012.

[76] The formation of a blast wave by a very intense explosion. I. Theoretical discussion. Taylor. g. *Proceedings of the Royal Society of London. Series A Mathematical and Physical Sciences*, pages 159–174, 1950.

[77] Matthew a. Price, Vinh-Tan Nguyen, Oubay Hassan, and Ken Morgan. A method for compressible multimaterial flows with condensed phase explosive detonation and airblast on unstructured grids. *Computers & Fluids*, 111:76–90, 2015.

[78] Michel Akiki and Suresh Menon. A model for hot spot formation in shocked energetic materials. *Combustion and Flame*, 162(5):1759–1771, 2015.

[79] M. Arienti, E. Morano, and J. E. Shepherd. Shock and detonation modeling with the mie-grneisen equation of state. *Graduate Aeronautical Laboratories Report FM99-8, California Institute of Technology, Pasadena, CA*, 2004.

[80] J. Zhang, T. L. Jackson, J. Busckmaster, and J. Freund. Numerical modeling of shock-to-detonation transition in energetic material. *Combustion and Flame*, 159:1769–1778, 2012.

[81] J Mespoulet, F Plassard, P Hereil, and A Lefrançois. Influence of HE shape on blast profile. In *8th European LS-DYNA Users Conference, Strasbourg*, pages 2–12, 2011.

Final Report

Combining Advanced Turbulent Mixing and Combustion Models with an Advanced Multi-Phase CFD Code to Simulate Detonation and Post Detonation Bio-Agent Mixing and Destruction

Final Report C496

PERIOD 01 June 2011 to 31 December 2015

Prepared by
Combustion Research and Flow Technology, Inc.
6210 Keller's Church Rd.
Pipersville, PA 18947
Attn: A. Zambon & N. Sinha
Phone: 215-766-1520
E-mail: azambon@craft-tech.com & sinha@craft-tech.com

28 March 2016

Prepared for
Dr. Suresh Menon
School of Aerospace Engineering
Georgia Institute of Technology
Atlanta, GA 30332-0150
Attn: Suresh Menon
Phone: 404-894-9196
E-mail: suresh.menon@ae.gatech.edu

Prepared under
Prime Contract No. HDTRA-11-0053
Subcontract Number: RB944S1
Period of Performance: 01 July 2011 to 31 December 2015

1.0 YEAR 1 SUMMARY

1.1 Project Major Goals

The primary goals for the Year 1 work period under this subcontract effort were as follows:

1 Assemble a database of BW agent neutralization models.
2 Develop a particle – turbulence interaction model for application to the spore neutralization model.

1.2 Accomplishments

During the Year 1 work period, efforts focused on Tasks 1.2, 1.4 and 1.5. Under Task 1.2, a literature review of current state-of-the-art biological warfare neutralization models was completed. This survey identified the form of the neutralization model and identified the model correlation coefficients for various neutralization scenarios. Under Task 1.4, a particle – turbulence interaction model was developed for application to the spore neutralization model identified under Task 1.2. Additionally, in coordination with Georgia Tech, the spore neutralization model was being coupled with a particulate combustion model for afterburning munitions. Under Task 1.5, implementation of the modeling formulation developed under Task 1.4 into the CRAFT CFD® flow solver was initiated.

1.3 Opportunities for Training and Professional Development

Nothing to report.

1.4 Results Dissemination to Communities of Interest

Modeling capabilities of the CRAFT CFD® code with respect to biological AD turbulent rate enhancement developed under the Basic Research program were highlighted in various review meetings of other DTRA programs in which CRAFT Tech was involved.

2.0 YEAR 2 SUMMARY

2.1 Project Major Goals

The primary goals for the Year 2 work period under this subcontract effort were as follows:

1. Develop and implement a turbulence model extension to account for turbulent – particle interactions on heterogeneous combustion of afterburning explosives (ABX) with a particular focus on aluminized charges. This modeling effort focused on developing a tractable, production level capability that may be applied within the context of routine, large scale analysis.

2. Integrate modeling formulations for spore – turbulence interactions, turbulence - particle interactions for heterogeneous combustion, and hybrid *Reynolds averaged Navier-Stokes/large eddy simulation* (RANS/LES) turbulence modeling for momentum and heat transport within a unified computational framework. This unified framework supports a production level simulation tool specialized for blast applications. This software tool will provide analyst with the capability to accurately and efficiently assess spore neutralization scenarios that employ ABX charges. This capability is specialized for computational efficiency within the context of routine, large scale applications.

3. Develop and implement turbulence model extensions to address turbulence – chemistry interaction for gas phase combustion within the context of production level applications. This includes a two phase approach to upgrade the computational framework developed under this subcontract. The first phase focuses on implementation of a first order modeling formulation that is generally applicable to account for the primary effect of turbulent combustion on gas phase chemical production. The second phase of this approach focuses on investigating the application of a more advanced modeling formulation under development at Georgia Tech within production level applications. For this second phase effort to be successful, an alternative approach must be found to apply this modeling formulation in a more efficient and computationally tractable manner.

2.2 Accomplishments

During the Year 2 work period, efforts focused on Tasks 1.5, 2.3 and 2.4. Under Task 1.5, the development and implementation of a particle – turbulence interaction model for spore neutralization was completed. This formulation was implemented into the production version of the CRAFT CFD® flow solver that has been developed for application to blast and biological warfare (BW) neutralization predictions. Under Task 2.3, a unified modeling formulation was developed and implemented to fully integrate and couple the modeling formulations developed under the previous work period's efforts. This effort consisted of integrating the spore interaction model of Task 1.4, a turbulence – particle interaction model for particulate combustion, and a hybrid *Reynolds averaged Navier-Stokes/large eddy simulation* (RANS/LES) subgrid model. With this unified formulation, spore neutralization strategies may be assessed for afterburning munitions within the context of production or engineering level evaluations. Testing of this unified formulation for a multi-room blast/neutralization problem was also carried out. A key finding of this model evaluation effort was that under certain conditions turbulence –

particle interactions significantly reduce spore neutralization rates. This model prediction has important implications for the assessment of prospective neutralization strategies. Neglecting the effect of turbulent fluctuations on the spore destruction rate could significantly *over estimate* the effectiveness of a neutralization strategy. As a result, it is important to include the effect of these fluctuations on any predictive assessment to provide a more conservative estimate of neutralization effectiveness.

Under Task 2.4, extensions of this modeling formulation for gas-phase turbulence chemistry interactions were initiated. The Eddy Dissipation Concept (EDC) formulation for turbulence – chemistry interactions was implemented within CRAFT CFD®. Also, efforts were initiated to investigate a more advanced combustion modeling formulation based on the linear-eddy model (LEM) in coordination with Georgia Tech. Application of the LEM within the context of large scale blast applications focused on development of a tractable formulation based of stochastic model parameterization. Within such an approach, closure statistic generated by the LEM are parameterized in terms of a reduced set of variables and stored within a model database. This database may then be deployed within a flow solver to account for turbulence – chemistry interaction based on the advanced formulation of the LEM, but at a small fraction of the computational cost.

2.3 Opportunities for Training and Professional Development

Nothing to report.

2.4 Results Dissemination to Communities of Interest

Modeling capabilities of the CRAFT CFD® code with respect to biological AD turbulent rate enhancement developed under the Basic Research program were highlighted in various review meetings of other DTRA programs in which CRAFT Tech is involved as well as at a C-WMD workshop attended by the broader C-WMD community directly supporting DTRA. Awareness on the potential enhancing/inhibiting effects of turbulent mixing on a number of finite-rate physical/chemical processes was raised, including for chemical AD.

3.0 YEAR 3 SUMMARY

3.1 Project Major Goals

Under this subcontract effort, the primary goal for the Year 3 work period was to perform verification and validation (V&V) of the predictive capabilities of the CRAFT CFD® code with respect to realistic blast event/agent defeat (AD) scenarios. Specifically, driven by DTRA's requirement to obtain greater confidence in the accuracy of computational simulations involving advanced high energy explosives in closed compartments/structures and agent defeat simulations with lower energy release and dispersion for neutralizers, the overarching technical objective was to assess the maturity of the CRAFT CFD® code in capturing the effects of turbulent mixing, disparate time-scales, multi-phase physics and scenario input uncertainty on AD in a complex geometry.

3.2 Accomplishments

During the Year 3 work period, efforts focused on Tasks 3.3 and 3.4 pertaining to the verification and validation (V&V) of the modeling capabilities of the CRAFT CFD® code with respect to agent dispersion and AD predictions, respectively. In coordination with DTRA, a specific AD test configuration of interest to DTRA was selected. Time accurate simulations were conducted of a realistic AD event in support of large scale test activities. As part of this analysis, comparison against measured test data and quantification of AD effectiveness of an enhanced high-energy explosive formulation (compared to a baseline formulation) were carried out. *Details of this analysis were provided directly to DTRA in a separate technical document.*

3.3 Opportunities for Training and Professional Development

Nothing to report.

3.4 Results Dissemination to Communities of Interest

Modeling capabilities of the CRAFT CFD® code with respect to AD turbulent rate enhancement developed under the Basic Research program have been highlighted in various review meetings of other DTRA programs in which CRAFT Tech is involved. Moreover, awareness on the potential enhancing/inhibiting effects of turbulent mixing on a number of finite-rate physical/chemical processes was raised to DTRA and the broader C-WMD community. With the enhanced fidelity upgrades and V&V of the CRAFT CFD® code for AD scenarios in place, improved predictive capabilities are available to the C-WMD community to address current threats and challenges, and design enhanced explosive formulations. Last, opportunities were identified for transitioning high-fidelity prediction results to C-WMD engineering tools.

4.0 YEAR 4 SUMMARY

4.1 Project Major Goals

Driven by DTRA's requirement to obtain greater confidence in the accuracy of computational simulations involving advanced high energy explosives in closed compartments/structures to support agent defeat (AD) with lower energy release and dispersion for neutralizers, the overarching technical objective for Year 4 of this program was to assess the maturity of CRAFT Tech's high-fidelity CRAFT CFD® code in capturing the effects of turbulent mixing, disparate time-scales and multi-phase physics characteristic of the AD problem. In Year 4 of this subcontract, the verification and validation (V&V) activities of the CRAFT CFD® code initiated in Year 3 continued. Particular emphasis was placed on supporting and complementing DTRA-funded AD testing programs and also in addressing AD diagnostics and safety requirements for AD tests to be planned.

4.2 Accomplishments

During the Year 4 work period, efforts continued to focus on Tasks 3.3 and 3.4 pertaining to V&V of the modeling capabilities of the CRAFT CFD® code with respect to AD predictions. In coordination with DTRA and leveraging on CRAFT Tech's active involvement in the AD Modeling and Simulation (M&S) community, test configurations of interest to DTRA were evaluated with respect to V&V as well as with respect to the design of new AD tests. Specifically:

- In preparation of chemical AD tests with simulants in the small-scale two-chamber test configuration at a Navy facility, a parametric study of the relevant design variables (e.g., amounts of HE, additives, simulant, etc.) was carried out to narrow down the parameter ranges to ensure safety and attain a representative AD scenario at the laboratory-scale. Based on these findings and on discussions with Navy personnel, a preliminary test design was identified, for which a high-fidelity simulation with the CRAFT CFD® code was carried out. Key aspects of interest in this simulations were (i) the characterization of chemical agent simulant neutralization and quantification of amounts released from the blast chamber into the exhaust chamber, and (ii) characterization of pressure and temperature levels in both chambers. Numerical results have been delivered to the Navy for comparison with their experimental data. *Details of this high-fidelity CFD analysis were documented and were provided directly to DTRA in a separate technical document.*
- As a member of the AD M&S community, CRAFT Tech is involved in high-fidelity V&V activities and AD test planning support. For a geometry of interest, additional side calculations were performed to exercise features or capabilities of the CRAFT CFD® code pertinent to turbulent mixing and AD effectiveness:
    - Since the temperature sensed by the agent as it is dispersed by turbulent mixing is a critical AD parameter, a diagnostic approach under development and stemming from DTRA Basic Research program is represented by micron-sized thermometers. As a demonstration of the ability of high-fidelity modeling to provide AD test planning support in estimating the temperature history experienced by these micro-thermometers and helping with the interpretation of the micro-thermometer measurement data, a computational particle tracking

exercise was performed in a post-detonation environment subject to turbulent mixing to provide time-resolved temperature histories and particle trajectories of selected tracers.

- A second computational exercise was performed with regard to deploying a simple, computationally-tractable turbulent combustion model like the Eddy Dissipation Concept (EDC - refer to Year 2 activities) in the same geometry to highlight agent neutralization rate sensitivities.

4.3 Opportunities for Training and Professional Development

Nothing to report.

4.4 Results Dissemination to Communities of Interest

Modeling capabilities of the CRAFT CFD® code with respect to AD turbulent rate enhancement developed under the Basic Research program have been highlighted in various review meetings of other DTRA programs in which CRAFT Tech is involved. Moreover, awareness on the potential enhancing/inhibiting effects of turbulent mixing on a number of finite-rate physical/chemical processes was raised to DTRA and the broader C-WMD community. With the enhanced fidelity upgrades and V&V of the CRAFT CFD® code for AD scenarios in place, improved predictive capabilities are available to the C-WMD community to address current threats and challenges, and design enhanced explosive formulations. Also, opportunities were identified for transitioning high-fidelity prediction results to C-WMD engineering tools. Last, CRAFT Tech has actively participated in the December 2015 Simulant Chemistry Workshop organized by DTRA. This was an excellent opportunity to further strengthen the link between DTRA's Basic Research portfolio and the applications side of DTRA's activities.

5.0 YEAR 1 ACTIVITIES

5.1 Task 1.2: Database Generation of BW Agent Neutralization Models

5.1.1 Overview

In this task, a survey of the state-of-the-art in biological warfare (BW) agent defeat (AD) modeling was performed. Relevant BW agent defeat models for thermal and/or chemical neutralization were selected and included in a spore kill database for use within CRAFT Tech's high-fidelity multi-phase interaction framework. It was found that for large-scale simulations of blast events, global models that rely on empirical correlations are suitable. The spore kill database targets primarily neutralization of *Bacillus anthracis* (*B.a.*) and *Bacillus Thuringiensis* (*B.t.*) exposed to a high temperature gas environment (HTGE). Experimental measurements on their rate of demise are generally performed under controlled conditions, uniform in space and constant in time, and data is then correlated in the form of an Arrhenius-like neutralization rate by assuming zero-order or first-order kinetics, as done in chemical kinetics modeling. During agent defeat events, e.g., a HE blast within a hardened target, conditions are highly variable. Therefore, within a modeling framework, the form of the neutralization rate should be sufficiently generalized to account for dependency on various parameters, e.g., humidity level, through a global representation. Rate data can be adjusted for specific conditions or replaced as new data or improved models become available.

5.1.2 Formulation

HTGE or a corrosive agent impact spore viability, i.e., their ability to form colonies. Spore neutralization is generally quantified in terms of log 10 reduction in viability. For instance, if n_0 is the initial spore number density number and n is the spore number density after exposure to HGTE, the viability ratio is defined as:

$$n/n_0 = 10^{-r} \tag{1}$$

While a five-decade viability reduction is generally accepted (r = 5), a kill effectiveness of r = 9 is desirable. Assuming a first-order global representation of neutralization, the evolution in time of the viability ratio is governed by the ordinary differential equation:

$$\frac{d\,(n/n_0)}{dt} = -k\left(n/n_0\right) \tag{2}$$

where the neutralization rate k is expressed in an Arrhenius-like form:

$$k = \alpha T^m e^{-\frac{\beta}{T}} \tag{3}$$

The rate parameters α, corresponding to a collision frequency, β, corresponding to an activation energy, and, m, representing a temperature exponent are determined from experiments.

5.1.3 Literature Survey

Past measurements of spore thermal inactivation have focused on relatively long exposure times, spanning from minutes to several hours, in moderate HGTE. Starting from the early work of Fernelius on *B.a.* and *Bacillus Subtilis* (*B.s.*) [1] to the more recent comprehensive survey of Spotts Whitney at CDC on *B.a.* [2], the temperature range considered remains low. Table 1 summarizes the data collected for moist heat (90 C – 120 C) and for dry heat (140 C – 200 C).

Table 1. Summary of data surveyed by Spott Whitney [2].

Temperature	Time	Inoculum size
Boiling		
100° C	10 min	3×10^6
	5 min	7.5×10^8
Moist heat		
90° C	20 min	1.2×10^6
90° C to 91° C	60 min	3×10^8
100° C	10 min	1.2×10^6
100° C to 101° C	17 min	1×10^5
105° C	10 min	3×10^6
120° C	15 min	2.4×10^8

Temperature	Time	Inoculum size
Dry heat		
140° C	>90 min	6×10^3 to 1.2×10^4
150° C	10 min	6×10^3 to 1.2×10^4
160° C	10 min	6×10^3 to 1.2×10^4
180° C	2 min	6×10^3 to 1.2×10^4
190° C	1 min	6×10^3 to 1.2×10^4
200° C	30 sec	6×10^3 to 1.2×10^4

For HGTE applications generated by a HE blast, e.g., munitions explosion, characteristic spore exposure time scales are less than 1 s and the peak temperatures reached span from several hundreds to more than a thousand degrees K. Figure 1 illustrates the distribution of HGTE temperatures and heating times encountered in HE applications and in long duration events (from Burggraf at the Air Force Institute of Technology (AFIT) [3][4]). Research programs at AFIT have focused on short duration thermal inactivation, both experimental characterization and numerical modeling accounting for the spore structure [3][4]. Particular emphasis was given to hydrolysis reactions and effects on the spore DNA.

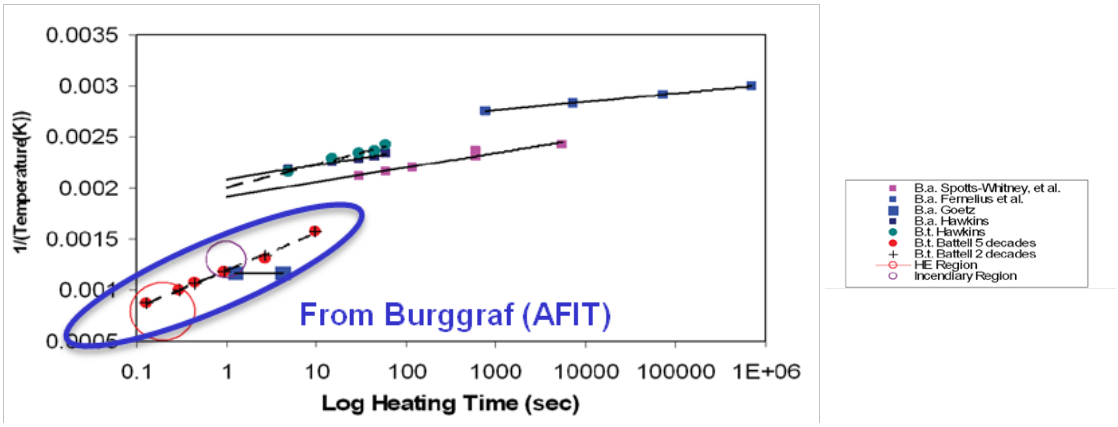

Figure 1: Summary of distribution of temperature and thermal exposure duration (from Burggraf, AFIT).

Similarly, Levin *et al.* conducted detailed modeling of *B.a.* spores in HGTE to support the interpretation of experimental findings [5]. Specifically, CFD and DSMC simulations were carried out to analyze the transient heat transfer to an individual spore based on the estimation of the heat transfer coefficient. Disagreement between gas-surface heat conduction results and experiments (the latter indicated a much longer deactivation time scale) prompted to speculate the effect of internal pressure exerted on the spore walls due to heating or the clumping of the spores, thereby providing a shielding effect and reducing the heat transfer rate to the spore. Although such detailed modeling analysis accounting for the spore structure and clump configuration are generally not usable directly in large-scale simulations of blast events, they are very valuable in the development of reduced-order models. In the future, these reduced-order models, consistent with a generalized neutralization rate formulation, can be integrated into CRAFT Tech's modeling framework.

Empirical correlations for B.t. demise have been formulated in the 423 K – 1210 K temperature range at Battelle [6][7]. Assuming a five decade viability reduction for neutralization, the residence time τ in HTGE required as a function of the air temperature T was derived. Similarly, correlations for the concurrent effect of HTGE and corrosive gases have been defined in terms of a single Arrhenius kinetics relations [8]. The primary argument is that HTGE directly attacks the spores and at the same time the high temperature accelerates the chemical attack of the corrosive agents. Under these conditions with biocidal material, reaction orders may not be purely zero-th or first order. A combined neutralization rate formula for Thiokol TP-H1246 propellant was derived.

More recently, SwRI has performed extensive experimental work in support of further development of the Empirical Lethality Methodology (ELM) [35]. The Air Force Nuclear Weapons Center, Capabilities and Integration Directorate (AFNWC/XR) maintains an agent defeat database addressing thermal, chemical and radiative neutralization. Testing was performed on *Bt* var. *kurstaki*, with particular emphasis on thermal neutralization and on effect of spores in hydrated form, for instance moist spores or spores in a suspension. A test matrix was constructed targeting environment temperatures of 200 C, 300 C and 400 C, and relative humidity (RH) levels of 27%, 48%, 82% and 96%. A substantial amount of data was collected based on repeated testing attempting to correlate key variables, namely (i) environment temperature T, (ii) RH and (iii) residence time τ of the spores in the HTGE to the viability ratio r, characterized in terms of Blood Agar Plate (BAP) log 10 kill. The raw data was processed into an apparent Arrhenius-like rate assuming a first-order reaction rate order for the rate of spore demise:

$$\ln k_{RH} = -\beta \frac{1}{T} + \ln \alpha \tag{4}$$

Specifically, a linear trend is expected between the inverse of the environment temperature and the logarithm of the neutralization rate. Here, the neutralization rate k_{RH} is computed from the exposure time τ and viability ratio r based on the analytical solution to the neutralization equation:

$$k_{RH}(T) = \frac{r \ln 10}{\tau} \tag{5}$$

Despite the significant scatter observed, several sets of Arrhenius-like rate parameters were identified at various levels of RH. This rate data for k_{RH} in terms of α and β can be deployed

directly into CRAFT Tech's high-fidelity modeling framework and has been incorporated into the spore kill database.

5.1.4 Additional Sensitive Sources for Spore Neutralization Rates

Additional data is potentially available from Government-generated agent defeat databases. For instance, these may include the Empirical Lethality Methodology (ELM) database [35], the US Army's Edgewood Chemical Biological Center (ECBC) Agent/Simulant Knowledge (ASK) database [10], and the data generated from an SBIR program with Air Force in 2003-2004 [11]. Although this data was not evaluated as part of the present task, it is expected to be compatible with the generalized spore neutralization form adopted in CRAFT Tech's modeling framework.

5.1.5 Additional Physico-Chemical Properties

Moreover, additional physico-chemical properties beyond neutralization rates are required for an accurate characterization of spore behavior within a high-fidelity modeling framework. For instance, these properties entail spore density, specific heat, size distribution, specific volume. For B.a. spores, Levin *et al.* have estimated density at about 1300.0 kg/m^3 and specific heat capacity at 2500.0 J/kg/K [5]. The U.S. Army's ECBC has characterized the size distribution of various strains of B.a. spores as well as several other spores, including, *B.t.*, *Bacillus subtilis*, *Bacillus cereus*, etc. [12]. For each strain and spore, they provide mean length, diameter, aspect ratio and volume as well as the range of variability. On average, a B.a. spore has a length of slightly above 1 μm and a diameter of above 0.8 μm.

5.2 Task 1.4: Turbulence Model Extensions for Biological Agent Neutralization

5.2.1 Particle – Turbulence Interaction Modeling for BW Agent Neutralization

In cooperation with Georgia Tech, CRAFT Tech has been focused on developing a particle – turbulence interaction model for biological agent neutralization for application to large scale problems of interest to DTRA. One primary requirement for this formulation is that it be tractable for routine application to realist, large scale problems. With this requirement in mind, a parameterized approach was chosen for the development of the formulation. Within this approach, the statistics from the physical models, such as those under development at Georgia Tech, are parameterized into an efficient database. In this manner, a large scale computation will access the model database to obtain the required statistics in an efficient and cost effective manner. This approach is in contrast to directly employing the physical model within the computation, which will be intractable for large scale problems of DTRA interest.

Within this overall approach, the modeling efforts thus far have focused on two aspects of particle – turbulence interactions. First, a parameterized model for spore neutralization has been developed to account for turbulence flow fluctuations on the neutralization rate. Second, following parallel efforts at Georgia Tech, a separate particle – turbulence interaction model has been developed for aluminum particle combustion for application to afterburning munitions that could be used for spore neutralization. These two modeling formulations will be coupled together to extend the applicability of the neutralization modeling for application to afterburning munitions.

The following subsections of this report summarize the modeling formulations for both the spore neutralization and the aluminum combustion.

5.2.2 Spore Particle Interaction Modeling

As discussed earlier, correlations for the rate of spore neutralization may be specified in the general form,

$$w_L = -\rho Y_L \alpha T^m \exp(-\beta / T) \tag{6}$$

where ρ is the gas phase density, Y_L is the live spore mass concentration, T is the gas phase temperature, and m, α and β are coefficients specified from experimental correlations. In this equation, the spore temperature is assumed to be in equilibrium with the gas phase so that the gas phase temperature appears in Eqn. (24). Application of Eqn. (24) to turbulent flow requires characterizing the effects of spore concentration and gas phase property fluctuations on the mean neutralization rate which may be written as,

$$\overline{w_L} = -\iiint \rho Y_L \alpha T^m \exp(-\beta / T) P(\rho, Y_L, T) d\rho dY_L dT \tag{7}$$

where P is the joint probability density function of the gas phase density and temperature, and the live spore mass concentration. Given P, the Eqn. (25) may be evaluated to characterize the effect of turbulent fluctuations on the mean neutralization rate.

The pdf in Eqn. (25) may be specified by either direct evaluation or a parameterization strategy. The direct evaluation approach seeks to predict the shape of the pdf through the solution of a transport equation for P based on fundamental principles. This approach is comprehensive, but intractable for all but a limited range of simplified problems. Alternatively, the effect of turbulent fluctuations within Eqn. (25) may be characterized through a parameterization of P in terms of a reduced set of variables. Through such an approach, a tractable modeling formulation may be developed that may be applied to large scale problems of interest. This type of parameterization approach was chosen to characterize the effect of turbulent fluctuations on the spore neutralization rate.

This work period, a parameterized modeling approach was developed to model Eqn. (25). Within this approach, the pdf P was parameterized using an assumed pdf formulation [19] assuming statistical independence between the density, temperature and spore concentration. With this assumption, the pdf in Eqn. (25) may be written as,

$$P(\rho, T, Y_L) \approx P_\rho(\rho - \overline{\rho}) P_T(T - \overline{T}) P_Y(Y_L - \overline{Y_L}) \tag{8}$$

where P_ρ, P_T, and P_Y are the marginal pdfs the density, temperature and spore concentration. These marginal pdfs are then specified as follows. For density, a delta function is specified for P_ρ [19]. For P_T and P_Y, a beta function [19] is used which is parameterized in terms of it first two moments. For example, using a beta function, P_Y may be expressed as,

$$P_Y(Y_L) = \frac{Y_L^{\beta_1 - 1}(1 - Y_L)^{\beta_2 - 1}}{\Gamma(\beta_1)\Gamma(\beta_2)} \Gamma(\beta_1 + \beta_2) \tag{9}$$

with,

$$\beta_1 = \overline{Y_L}\left[\frac{\overline{Y_L}(1-\overline{Y_L})}{\overline{Y_L'^2}} - 1\right], \quad \beta_2 = (1-\overline{Y_L})\left[\frac{\overline{Y_L}(1-\overline{Y_L})}{\overline{Y_L'^2}} - 1\right] \tag{10}$$

where $\Gamma(x)$ is the gamma function. As seen in these equations, the beta function for Y_L has been parameterized in terms of the mean spore concentration ($\overline{Y_L}$) and its variance ($\overline{Y_L'^2}$). A similar expression may be developed for P_T that is parameterized in terms of the mean temperature and temperature variance.

With this parameterization of Eqn. (26), the mean spore neutralization rate in Eqn. (25) may be evaluated. With this formulation, a pdf table generator code was developed this work period to generate a database for the mean spore rate as a function of the mean temperature, temperature variance, mean spore concentration, and spore concentration variance. This database may then be used to specify the mean spore rate (Eqn. (25)) in the spore transport equation.

This parameterized formulation additionally requires the specification of the temperature and spore concentration variances that appears in the beta representations of P_T and P_Y. These quantities are specified from addition transport equations. For the temperature variance, a variable turbulent Prandtl number model [20] that is applicable to reacting flows is used. For the spore fluctuations, a spore concentration variance equation was developed that is similar to the species concentration variance methodology of Gaffney, et al. [21]. This equation includes an additional term of the form $\overline{Y_L w_L}$, which is also modeling using the assumed pdf methodology of Eqn. (26). The parameterized model of this term is also stored within the model database that is generated by the pdf table generator that was developed this work period.

The development of the pdf table generator for the mean spore rate was completed this work period. Also, this work period, the implementation of the mean spore concentration and concentration variance equations into the CRAFT CFD® code was initiated under Task 1.5. This formulation is being implemented into the version of the CRAFT CFD® that includes the aluminum combustion model for afterburning munitions. This modeling formulation is described in the next subsection.

5.2.3 Particle - Turbulence Interaction Modeling for Aluminum Particulates

For turbulent flow, velocity and composition fluctuations will influence the burning rate of solid aluminum particulates within afterburning munitions that may be used for spore neutralization. To account for these fluctuations, two approaches may be considered. The first is a *microscopic* approach that seeks to model the direct interaction of the flow with the flame structure surrounding the particles from a first principles perspective. The second is a *macroscopic* approach that seeks to account for flowfield fluctuations on the *modeled* laminar burning rate. The microscopic approach is more fundamental, but intractable from the perspective of applying it routinely to problems of practical interest. The macroscopic approach is more pragmatic and empirical, but provides a viable alternative to develop a tractable formulation. As a

consequence, modeling efforts focused on the development of a macroscopic particle – turbulence interaction model that may be routinely applied to problems of interest.

For the macroscopic approach, the model sought to account for the effects of turbulent fluctuations on the modeled laminar particle burning rate. Within CRAFT Tech's Eulerian dispersed phase particle combustion modeling formulation, the *laminar* aluminum particle mass density consumption rate is expressed as,

$$m_p = -2\pi r_p^2 N \rho_m \frac{\partial d_p}{\partial t} \tag{11}$$

where ρ_p is the particle mass density, ρ_m is the material density, N is the particle number density, and r_p and d_p are the particle radius and diameter, respectively. The time derivative in Eqn. (30) is also expressed as,

$$\frac{\partial d_p}{\partial t} = \frac{1}{n d_p^{n-1} A_n + m d_p^{m-1} A_m} \tag{12}$$

with,

$$A_n = \frac{1}{A_1 \exp(-E_b / RT_p) X_{eff}} \frac{1}{1-\varepsilon^n} \tag{13}$$

$$A_m = \frac{A_2}{T^{0.2} P^{0.1} X_{eff}} \frac{1}{1-\varepsilon^n} \tag{14}$$

where n = 0.3, m = 1.8, $A_1 = 5.5x10^4$, $A_2 = 7.35x10^{-6}$, ε = 0.05, E_b = 73.6 kJ/mol, R is the gas constant, T_p is the particle surface temperature, P is the pressure, T is the gas temperature. The variable X_{eff} is the sum of gas phase mole fractions of O_2, H_2O and CO_2 as given by,

$$X_{eff} = X_{O_2} + 0.6 X_{H_2O} + 0.22 X_{CO_2} \tag{15}$$

Eqns. (30) – (34) were developed from the Yetter's hybrid combustion model [22] for aluminum particle burning. This model formulation accounts for both the diffusion-controlled and kinetically-controlled burning limits, and a transition between the two. With this formulation, the particle mass density consumption rate in Eqn. (30) may be written as a function of the particle and gas phase properties as,

$$m_p = f(r_p, T_p, P, T, X_k) \tag{16}$$

where X_k are the species mole fractions. This equation is a representation of the laminar burning rate model within CRAFT Tech's dispersed phase combustion model for aluminum particles.

With the laminar rate model given by Eqn. (35), a macroscopic level model for the effect of turbulent fluctuations on the rate expression could be represented by,

$$\overline{m_p} = \int pdf(r_p, T_p, P, T, X_k) f(r_p, T_p, P, T, X_k) dr_p dT_p dP dT dX_k \tag{17}$$

where $pdf(r_p, T_p, P, T, X_k)$ is the joint probability density function of the particle and gas phase properties and the overbar represents Reynolds averaging. With Eqn. (36), a *parameterized*

model for this mean rate expression has been developed. As discussed earlier, a parameterized modeling formulation seeks to represent the model statistics in terms of a reduced set of variables. These model statistics may then be stored within a database. A flow solver may then retrieve the model statistics from the database in a fast and efficient manner.

To develop a parameterized model for Eqn. (36), it should first be recognized that the particle and gas phase properties for dispersed phase combustion are effectively uncorrelated. That is, specific gas phase properties do not necessary correspond to specific particle phase properties. For example, high instantaneous values of gas phase temperature, T, do not necessarily correspond to high instantaneous values of particle temperature, or specific values of particle radius. The particle and gas phase properties will only be strongly correlated when the two phases are in equilibrium. As a result, the particle and gas phase properties may be assumed to be statistically independent. With this assumption, the joint pdf in Eqn. (36) may be expressed as a combination of the marginal pdfs of these variables as,

$$pdf(r_p, T_p, P, T, X_k) = pdf(r_p, T_p)\, pdf(P, T, X_k) \tag{18}$$

With this representation of the joint pdf, an assumed pdf model [19] may be used to develop an approximation for the RHS of Eqn. (37). To develop a first order model, the pdf of the particle properties is assumed to be composed of delta functions at the mean particle values. For the gas phase pdf, the pressure is also assumed to be statistically independent of the temperature and species. These assumptions are reasonable for the present application because the particle and gas phase properties are effectively uncorrelated as discuss earlier. With these assumptions, Eqn. (37) may be rewritten as,

$$pdf(r_p, T_p, P, T, X_k) \approx \delta(r_p - \overline{r_p})\delta(T_p - \overline{T_p})\, pdf(P)\, pdf(T, X_k) \tag{19}$$

For the gas phase pdfs, assumed pdf methods typically employ a delta function for the marginal pdf of pressure. The task then becomes to develop a parameterized model for $pdf(T, X_k)$. For afterburning munitions, particle – turbulence interactions will primarily occur in the shear layer region between the ambient fluid and the blast constituents where mixing and combustion may occur. Under these conditions, the mixture gas phase properties could be parameterized in terms of mixture fraction (Z) and scalar dissipation (χ), similar to the parameterization used by Sankaran, et al. [23] for gas phase combustion and for flamelet models [19]. Consequently, the local temperature and species within the shear layer may be written as $T = T(Z, \chi, P)$ and $X_k = X_k(Z, \chi, P)$, with the pressure being included due to compressibility effects within the flow. This parameterization of the gas phase properties may be accomplished using a flamelet model [19] given representative thermodynamic properties of the flow (i.e., fuel and oxidizer composition, and pressure range). With this representation, and the aforementioned assumption regarding the statistical independence of the pressure and temperature and species, Eqn. (38) then becomes,

$$pdf(r_p, T_p, P, T, X_k) \approx \delta(r_p - \overline{r_p})\delta(T_p - \overline{T_p})\delta(P - \overline{P})\delta(\chi - \overline{\chi})\, pdf(Z) \tag{20}$$

where the typical assumptions regarding scalar dissipation from assumed pdf methods have been employed [19].

Within Eqn. (39), the pdf of mixture fraction may be approximated using a beta function [19]. The mean particle density consumption rate in Eqn. (39) may be evaluated as a function of the mean flow and particle properties as,

$$\overline{m_p} = g(\overline{r_p}, \overline{T_p}) h(\overline{P}, \overline{\chi}, \overline{Z}, \overline{Z'^2}) \tag{21}$$

where the functions *g* and *h* are independent due to the previous assumption that the particle and flow properties are uncorrelated. Alternatively, a function *F* may be defined as the ratio of turbulent-to-laminar burning rate as,

$$F(\overline{r_p}, \overline{T_p}, \overline{P}, \overline{\chi}, \overline{Z}, \overline{Z'^2}, \overline{T}) = \frac{\overline{m_p}}{m_{p,lam}} \tag{22}$$

where $m_{p,lam}$ is the consumption rate defined by Eqn. (35) evaluated based on *mean* flow quantities only. The term $m_{p,lam}$ is the value of the consumption rate that neglects all turbulent fluctuations, or that is the effective laminar rate.

With Eqns. (39)-(41), a database for the function *F* may be evaluated given the representative thermodynamics conditions of the problem. This database may then be deployed within a CFD flow solver so that the mean particle density consumption rate may be evaluated as,

$$\overline{m_p} \approx m_{p,lam} F(\overline{r_p}, \overline{T_p}, \overline{P}, \overline{\chi}, \overline{Z}, \overline{Z'^2}, \overline{T}) \tag{23}$$

By defining the mean consumption rate in this manner, the first order effect of turbulent flowfield fluctuations may be included. To apply this model, the CFD flow solver must additionally solve standard transport equations for $\overline{Z}$ and $\overline{Z'^2}$. These transport equation may be specified using the compressible flow, variable turbulent Schmidt number formulation of Brinckman, et al. [24].

With this modeling formulation, the CFD flow solver is only required to include just two additional transport equations. The multiplying function *F* is also retrieved from a database in a fast and efficient manner. As a result, this first order turbulence – particle interaction model is computationally inexpensive to employ for large scale applications. The effects of this modeling formulation on aluminum particle combustion may be seen, for example, in Figure 2 for an unsteady, high speed shear layer. This figure presents the reaction enhancement factor *F* in Eqn. (41). This figure shows contours of this function in the ignition region of the aluminum particulates.

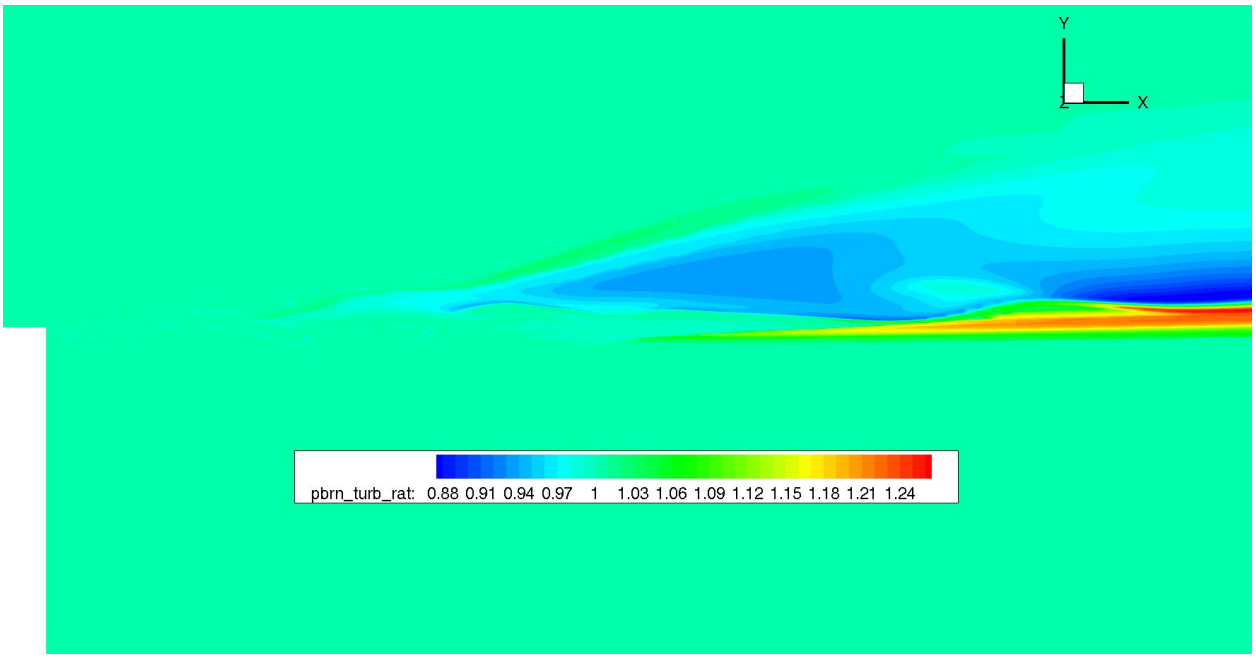

Figure 2: Instantaneous particle reaction enhancement factor contours for the unsteady particle burning a P = 1 atm, T_{fuel} = 2000 K and 1 micron particles

This aluminum combustion modeling formulation is currently being coupled with the spore combustion model described in the previous subsection under Task 1.5.

5.3 Task 1.5: Combined Effort for Model Integration in CRAFT Tech Codes

Under this task, efforts were initiated to integrate the aforementioned spore neutralization model into CRAFT CFD®. The spore modeling formulation is being integrated within the aluminum combustion model that has been developed for afterburning munitions. With the completion of the modeling formulation and the model database generator under Task 1.4, implementation of the spore transport and spore concentration variance equations into CRAFT CFD® was initiated. With the completion of this implementation, testing, evaluation and validation of the formulation will be carried in Year 2.

5.4 References

[1] Fernelius, A.L., "A probit method to interpret thermal inactivation of bacterial spores," *J. of Bacteriology,* 75(3), 1957.

[2] Spotts Whitney *et al.,* "Inactivation of Bacillus anthracis Spores", *Emerging Infectious Deseases*, Volume 9, Number 6, June 2003.

[3] Knight, E.A., *Modeling thermal inactivation of bacillus spores*, Master of Science Thesis, Air Force Institute of Technology, March 2009.

[4] Goetz, K.M., *Lethality of bacillus anthracis spores due to short duration heating measured using infrared spectroscopy*, Master of Science Thesis, Air Force Institute of Technology, March 2005.

[5] Rakesh, K., Samarth, S., Titov, E.V., Levin, D.A., Long, R.F., Neely, W.C., and Setlow, P., "Thermo-structural studies of spores subjected to high temperature gas environments," *International Journal of Heat and Mass Transfer* 54 (2011) 755–765.

[6] Toton, E., Kim, K., DeBell, R., Bradley, S., Anderson, R., Hookham, P., Matthews, M., Zavitsanos, P. and Pierce, P., *"High Temperature Incendiary Technologies to Counter Facilities for Biological and Chemical Weapons of Mass Destruction*", DSWA Report No. DSWA-TR-98-60, August 1998.

[7] Alexander, C.A., Ogden, J.S., LeVere, M.A., Dye, C.F. and Kohler, D.F., "Thermal Deactivation of Aerosolized Bacteria," Battelle Report for Defense Threat Reduction Agency, Contract No. DNA001-95-C-0031, November 1998.

[8] Kim, K., Gresham, M.K., Toton, E., Pallotta, B., Pierce, T., Rogers, S., and Stock, M., *Prompt Agent Defeat – A Program to Counter Facilities for Biological Weapons of Mass Destruction*, Defense Threat Reduction Agency, 2004.

[9] Gauger *et al*., *Empirical Lethality Methodology (ELM): Thermal neutralization of hydrated spore stocks: Final hydrated spores neutralization report*, SwRI, October, 2011.

[10] Ashman, W.P., Jablonski, R.E., and Harrah, M., CHEMICAL BIOLOGICAL AGENT SIMULANT KNOWLEDGE (ASK) V2.0 DATABASE, US Army Edgewood Chemical Biological Center Chemical Biological, July 2003.

[11] Agent Defeat Short Term Neutralization Data Collection and Modeling, Air Force SBIR, F08630-03-C-0018, 2003.

[12] Carrera, M., Zandomeni, R.O, Fitzgibbon, J. and Sagripanti, J.-L., Difference between the spore sizes of Bacillus anthracis and other Bacillus species, *Journal of Applied Microbiology* 102 (2007) 303–312.

[13] Peters, N., Turbulent Combustion, Cambridge University Press, Cambridge, UK, 2000.

[14] Calhoon, W.H., Jr., Brinckman, K.W., Tomes, J., Mattick, S. and Dash, S.M.., "Scalar Fluctuation and Transport Modeling for Application to High Speed Reacting Flows" AIAA Paper No. AIAA-2006-1452, 44th Aerospace Sciences Meeting and Exhibit, Reno, NV, Jan. 9-12, 2006.

[15] Gaffney, R.L., Jr., White, J.A., Girimaji, S.S. and Drummond, J.P., "Modeling Turbulent and Species Fluctuations in Turbulent, Reacting Flow, " *Computing Systems in Engineering*, Vol. 5, No. 2, pp. 117–133, 1994.

[16] Yetter, R., Private Communications, Penn State University, August, 2007.

[17] Sankaran, V., Drozda, T.G., and Oefelein, J.C., "A Tabulated Closure for Turbulent Non-premixed Combustion Based on the Linear Eddy Model," *Proceedings of the Combustion Institute*, Vol. 32, pp. 1571 – 1578, 2009.

[18] Brinckman, K.W., Calhoon, W.H., Jr., Mattick, S.J., Tomes, J., and Dash, S.M., "Scalar Variance Model Validation for High-Speed Variable Composition Flows," *44th AIAA Aerospace Sciences Meeting and Exhibit*, Reno, NV, AIAA Paper 2006-0715, January 9–12, 2006.

6.0 YEAR 2 ACTIVITIES

6.1 Task 1.5: Combined Effort for Model Integration in CRAFT Tech Codes

Under this task, the development and implementation of the particle – turbulence interaction model for spore neutralization that was developed in Year 1 under Task 1.4 was completed. This formulation characterizes the influence of turbulent flow scalar fluctuations on the evolution of spore particulates and the spore neutralization rate. This model employs the neutralization rate formulation identified under Task 1.2. The effect of turbulent flow fluctuations on the evolution of the spores is included within a computationally tractable *parameterization* approach. Within such an approach, the effects of scalar fluctuations on the mean or subgrid averaged spore neutralization rate is included by parameterizing spore rate fluctuation statistics from a computational sub-model. These statistics are then organized within a database which is used for a run-time calculation. In such a manner, the model statistics required by the CFD flow solver are obtained from the model database and are not computed "on the fly". As such, this formulation is computationally tractable for large scale, production level applications because the computational cost of accessing the database is much less than the direct application of the sub-model at run-time. This spore particle – turbulence interaction modeling formulation is summarized in a following sub-section of this report.

During the Year 2 work period, the development and implementation of this modeling formulation was completed. This included the development of the computational sub-model and the model statistics processing and database generation software. This formulation was implemented within the production version of the CRAFT CFD® flow solver that has been developed for application to blast and biological warfare (BW) neutralization predictions. Testing and application of this formulation will be described in a following sub-section.

6.2 Task 2.3: Turbulence Model Extensions for Dispersed Phase Combustion

Under this task, a unified modeling formulation was developed and implemented to fully integrate the modeling formulation developed under the previous work period's efforts with additional models to address particulate combustion and transport modeling. This effort consisted of integrating: 1) the spore particle - turbulence interaction model of Task 1.4, 2) a particle – turbulence interaction model for particulate combustion, and 3) a hybrid RANS/LES subgrid model. This development effort was in parallel to work at Georgia Tech to address neutralization strategies within the context of aluminized afterburning munitions. However, efforts under this task focused on large scale, production level applications that may be applied for routine analysis needs. With this unified formulation, the effects of turbulent flow fluctuations on the spore neutralization and particulate combustion may be captured. Also, this modeling formulation was extended to include a compressible flow hybrid RANS/LES modeling formulation for turbulent momentum and heat transport. This hybrid formulation allows for a tractable, but advanced, treatment of turbulent transport phenomena within a large scale computation. Within this approach, an unsteady RANS modeling formulation is employed within regions of the flow where turbulent flow structures may not be resolved in a tractable manner. These regions include, for example, boundary layer flows along the walls of a multi-room blast calculations. Turbulent fluctuations within these regions may not be tractably resolved and may be accurately modeled with an unsteady RANS formulation. However, away from these fine scale regions, the flow model transitions to LES in regions where large scale

turbulent structure may be resolved. Resolving these large scale structures in regions of shear and mixing will provide for a more accurate representation of the flowfield. Under this task an advanced hybrid RANS/LES formulation was coupled with the spore and particulate combustion models. This hybrid model has also been extended for application to highly compressible flows that are characteristic of BW neutralization applications.

The following sub-section first presents a brief description of the spore, particulate combustion, and hybrid RANS/LES models. This is followed by an illustration of the behavior of the spore model for a compressible shear layer case, and a description of the preliminary application of the modeling approach to a BW neutralization case.

6.2.1 Spore Particle – Turbulence Interaction Modeling

As identified under Task 1.2 from the Year 1 work efforts, correlations for the rate of spore neutralization may be specified in the general form,

$$w_L = -\rho Y_L^{\theta} \alpha T^m \exp(-\beta / T) \tag{24}$$

where ρ is the gas phase density, Y_L is the live spore mass concentration, T is the gas phase temperature, and m, α, θ, and β are coefficients specified from experimental correlations. In this equation, the spore temperature is assumed to be in equilibrium with the gas phase so that the gas phase temperature appears in Eqn. (24). Application of Eqn. (24) to turbulent flow requires characterizing the effects of spore concentration and gas phase property fluctuations on the mean neutralization rate which may be written as,

$$\overline{w_L} = -\iiint \rho Y_L \alpha T^m \exp(-\beta / T) P(\rho, Y_L, T) d\rho dY_L dT \tag{25}$$

where P is the joint probability density function of the gas phase density and temperature, and the live spore mass concentration. Given P, Eqn. (25) may be evaluated to characterize the effect of turbulent fluctuations on the mean neutralization rate.

The pdf in Eqn. (25) may be specified by either direct evaluation or a parameterization strategy. The direct evaluation approach seeks to predict the shape of the pdf through the solution of a transport equation for P based on fundamental principles. This approach is comprehensive, but intractable for all but a limited range of simplified problems. Alternatively, the effect of turbulent fluctuations within Eqn. (25) may be characterized through a parameterization of P in terms of a reduced set of variables. Through such an approach, a tractable modeling formulation may be developed that may be applied to large scale problems of interest. This type of parameterization approach was chosen to characterize the effect of turbulent fluctuations on the spore neutralization rate.

A parameterized modeling approach has been developed to model Eqn. (25) so that the pdf P is parameterized using an assumed pdf formulation [19] assuming statistical independence between the density, temperature and spore concentration. With this assumption, the pdf in Eqn. (25) may be written as,

$$P(\rho, T, Y_L) \approx P_\rho(\rho - \overline{\rho}) P_T(T - \langle T \rangle) P_Y(Y_L - \langle Y_L \rangle) \tag{26}$$

where P_ρ, P_T, and P_Y are the marginal pdfs the density, temperature and spore concentration. In this equation, the overbar represents Reynolds averaging or filtering, while the brackets represent Favre averaging or filtering. These marginal pdfs are then specified as follows. For density, a delta function is specified for P_ρ [19]. For P_T and P_Y, a beta function [19] is used which is parameterized in terms of it first two moments. For example, using a beta function, P_Y may be expressed as,

$$P_Y(Y_L) = \frac{Y_L^{\beta_1 - 1}(1 - Y_L)^{\beta_2 - 1}}{\Gamma(\beta_1)\Gamma(\beta_2)}\Gamma(\beta_1 + \beta_2) \tag{27}$$

with,

$$\beta_1 = < Y_L > \left[\frac{< Y_L > (1 - < Y_L >)}{< Y_L''^2 >} - 1\right], \quad \beta_2 = (1 - < Y_L >)\left[\frac{< Y_L > (1 - < Y_L >)}{< Y_L''^2 >} - 1\right] \tag{28}$$

where $\Gamma(x)$ is the gamma function. As seen in these equations, the beta function for Y_L has been parameterized in terms of the mean spore concentration ($< Y_L >$) and its variance ($< Y_L''^2 >$). A similar expression may be developed for P_T that is parameterized in terms of the mean temperature and temperature variance.

With this parameterization of Eqn. (26), the mean spore neutralization rate in Eqn. (25) may be evaluated. With this formulation, a pdf table generator code was developed to generate a database for the mean spore rate as a function of the mean temperature, temperature variance, mean spore concentration, and spore concentration variance. This database may then be used to specify the mean spore rate (Eqn. (25)) in the spore transport equation.

This parameterized formulation additionally requires the specification of the temperature and spore concentration variances that appears in the beta representations of P_T and P_Y. These quantities are specified from addition transport equations. For the temperature variance, a variable turbulent Prandtl number model [20] that is applicable to reacting flows and a hybrid RANS/LES formulation is used. For the spore fluctuations, a spore concentration variance equation was developed that is similar to the species concentration variance methodology of Gaffney, et al. [21]. This equation is given by,

$$\begin{aligned} &\frac{\partial \bar{\rho} < q >}{\partial t} + \frac{\partial \bar{\rho} < u_j >< q >}{\partial x_j} - \frac{\partial}{\partial x_j}\left[\bar{\rho}(D + D_T)\frac{\partial < q >}{\partial x_j}\right] = \\ &+2\bar{\rho}D_T\left(\frac{\partial < Y_L >}{\partial x_j}\right)^2 - 2\bar{\rho}\frac{< q >}{\tau_T} - 2 < Y_L > \overline{\omega_L} + 2\overline{Y_L\omega_L} \end{aligned} \tag{29}$$

where $< q >=< Y_L''^2 >$, and τ_T is the turbulent mixing time scale as specified from the hybrid RANS/LES model. The term $\overline{Y_L\omega_L}$ is also modeled using the assumed pdf methodology of Eqn. (26). The parameterized model of this term is also stored within the model database that is generated by the pdf table generator.

6.2.2 Particle - Turbulence Interaction Modeling for Aluminum Particulate Combustion

For turbulent flow, velocity and composition fluctuations will influence the burning rate of solid aluminum particulates within afterburning munitions that may be used for spore neutralization. To account for these fluctuations, two approaches may be considered. The first is a *microscopic* approach that seeks to model the direct interaction of the flow with the flame structure surrounding the particles from a first principles perspective. The second is a *macroscopic* approach that seeks to account for flowfield fluctuations on the *modeled* laminar burning rate. The microscopic approach is more fundamental, but intractable from the perspective of applying it routinely to problems of practical interest. The macroscopic approach is more pragmatic and empirical, but provides a viable alternative to develop a tractable formulation. As a consequence, modeling efforts focused on the development of a macroscopic particle – turbulence interaction model that may be routinely applied to problems of interest.

For the macroscopic approach, the model sought to account for the effects of turbulent fluctuations on the modeled laminar particle burning rate. Within CRAFT Tech's Eulerian dispersed phase particle combustion modeling formulation, the *laminar* aluminum particle mass density consumption rate is expressed as,

$$m_p = -2\pi r_p^2 N \rho_m \frac{\partial d_p}{\partial t} \tag{30}$$

where ρ_p is the particle mass density, ρ_m is the material density, N is the particle number density, and r_p and d_p are the particle radius and diameter, respectively. The time derivative in Eqn. (30) is also expressed as,

$$\frac{\partial d_p}{\partial t} = \frac{1}{n d_p^{n-1} A_n + m d_p^{m-1} A_m} \tag{31}$$

with,

$$A_n = \frac{1}{A_1 \exp(-E_b / RT_p) X_{eff}} \frac{1}{1-\varepsilon^n} \tag{32}$$

$$A_m = \frac{A_2}{T^{0.2} P^{0.1} X_{eff}} \frac{1}{1-\varepsilon^n} \tag{33}$$

where n = 0.3, m = 1.8, $A_1 = 5.5x10^4$, $A_2 = 7.35x10^{-6}$, ε = 0.05, E_b = 73.6 kJ/mol, R is the gas constant, T_p is the particle surface temperature, P is the pressure, T is the gas temperature. The variable X_{eff} is the sum of gas phase mole fractions of O_2, H_2O and CO_2 as given by,

$$X_{eff} = X_{O_2} + 0.6 X_{H_2O} + 0.22 X_{CO_2} \tag{34}$$

Eqns. (30) – (34) were developed from the Yetter's hybrid combustion model [22] for aluminum particle burning. This model formulation accounts for both the diffusion-controlled and kinetically-controlled burning limits, and a transition between the two. With this formulation,

the particle mass density consumption rate in Eqn. (30) may be written as a function of the particle and gas phase properties as,

$$m_p = f(r_p, T_p, P, T, X_k) \tag{35}$$

where X_k are the species mole fractions. This equation is a representation of the laminar burning rate model within CRAFT Tech's dispersed phase combustion model for aluminum particles.

With the laminar rate model given by Eqn. (35), a macroscopic level model for the effect of turbulent fluctuations on the rate expression could be represented by,

$$\overline{m_p} = \int pdf(r_p, T_p, P, T, X_k) f(r_p, T_p, P, T, X_k) dr_p dT_p dP dT dX_k \tag{36}$$

where $pdf(r_p, T_p, P, T, X_k)$ is the joint probability density function of the particle and gas phase properties and the overbar represents Reynolds averaging. With Eqn. (36), a *parameterized* model for this mean rate expression has been developed. As discussed earlier, a parameterized modeling formulation seeks to represent the model statistics in terms of a reduced set of variables. These model statistics may then be stored within a database. A flow solver may then retrieve the model statistics from the database in a fast and efficient manner.

To develop a parameterized model for Eqn. (36), it should first be recognized that the particle and gas phase properties for dispersed phase combustion are effectively uncorrelated. That is, specific gas phase properties do not necessary correspond to specific particle phase properties. For example, high instantaneous values of gas phase temperature, *T*, do not necessarily correspond to high instantaneous values of particle temperature, or specific values of particle radius. The particle and gas phase properties will only be strongly correlated when the two phases are in equilibrium. As a result, the particle and gas phase properties may be assumed to be statistically independent. With this assumption, the joint pdf in Eqn. (36) may be expressed as a combination of the marginal pdfs of these variables as,

$$pdf(r_p, T_p, P, T, X_k) = pdf(r_p, T_p) pdf(P, T, X_k) \tag{37}$$

With this representation of the joint pdf, an assumed pdf model [19] may be used to develop an approximation for the RHS of Eqn. (37). To develop a first order model, the pdf of the particle properties is assumed to be composed of delta functions at the mean particle values. For the gas phase pdf, the pressure is also assumed to be statistically independent of the temperature and species. These assumptions are reasonable for the present application because the particle and gas phase properties are effectively uncorrelated as discuss earlier. With these assumptions, Eqn. (37) may be rewritten as,

$$pdf(r_p, T_p, P, T, X_k) \approx \delta(r_p - \overline{r_p}) \delta(T_p - \overline{T_p}) pdf(P) pdf(T, X_k) \tag{38}$$

For the gas phase pdfs, assumed pdf methods typically employ a delta function for the marginal pdf of pressure. The task then becomes to develop a parameterized model for $pdf(T, X_k)$. For afterburning munitions, particle – turbulence interactions will primarily occur in the shear layer

region between the ambient fluid and the blast constituents where mixing and combustion may occur. Under these conditions, the mixture gas phase properties could be parameterized in terms of mixture fraction (Z) and scalar dissipation (χ), similar to the parameterization used by Sankaran, et al. [23] for gas phase combustion and for flamelet models [19]. Consequently, the local temperature and species within the shear layer may be written as $T = T(Z,\chi,P)$ and $X_k = X_k(Z,\chi,P)$, with the pressure being included due to compressibility effects within the flow. This parameterization of the gas phase properties may be accomplished using a flamelet model [19] given representative thermodynamic properties of the flow (i.e., fuel and oxidizer composition, and pressure range). With this representation, and the aforementioned assumption regarding the statistical independence of the pressure and temperature and species, Eqn. (38) then becomes,

$$pdf(r_p,T_p,P,T,X_k) \approx \delta(r_p - \overline{r_p})\delta(T_p - \overline{T_p})\delta(P - \overline{P})\delta(\chi - <\chi>)pdf(Z) \tag{39}$$

where the typical assumptions regarding scalar dissipation from assumed pdf methods have been employed [19].

Within Eqn. (39) , the pdf of mixture fraction may be approximated using a beta function [19] The mean particle density consumption rate in Eqn. (39) may be evaluated as a function of the mean flow and particle properties as,

$$\overline{m_p} = g(\overline{r_p},\overline{T_p})h(\overline{P},<\chi>,<Z>,<Z'^2>) \tag{40}$$

where the functions g and h are independent due to the previous assumption that the particle and flow properties are uncorrelated. Alternatively, a function F may be defined as the ratio of turbulent-to-laminar burning rate as,

$$F(\overline{r_p},\overline{T_p},\overline{P},<\chi>,<Z>,<Z'^2>,<T>) = \frac{\overline{m_p}}{m_{p,lam}} \tag{41}$$

where $m_{p,lam}$ is the consumption rate defined by Eqn. (35) evaluated based on *mean* flow quantities only. The term $m_{p,lam}$ is the value of the consumption rate that neglects all turbulent fluctuations, or that is the effective laminar rate.

With Eqns. (39)-(41), a database for the function F may be evaluated given the representative thermodynamics conditions of the problem. This database may then be deployed within a CFD flow solver so that the mean particle density consumption rate may be evaluated as,

$$\overline{m_p} \approx m_{p,lam}F(\overline{r_p},\overline{T_p},\overline{P},<\chi>,<Z>,<Z'^2>,<T>) \tag{42}$$

By defining the mean consumption rate in this manner, the first order effect of turbulent flowfield fluctuations may be included. To apply this model, the CFD flow solver must additionally solve standard transport equations for $<Z>$ and $<Z'^2>$. These transport equation may be specified using the compressible flow, variable turbulent Schmidt number formulation of Brinckman, et al. [24].

With this modeling formulation, the CFD flow solver is only required to include just two additional transport equations. The multiplying function F is also retrieved from a database in a fast and efficient manner. As a result, this first order turbulence – particle interaction model is computationally inexpensive to employ for large scale applications.

6.2.3 Hybrid RANS/LES Model for Momentum and Heat Transport

The hybrid RANS/LES (HRLES) model employs the standard k-ε equations of a typical RANS formulation. However, the eddy viscosity is suitably scaled down in LES regions based on an assessment of the local resolution levels and the local range of scales that this resolution would permit. This assessment is based on the RANS estimate for the turbulent kinetic energy, and an estimate of the range of turbulent scales that could be supported on the computational grid, assuming a pre-specified empirical form of the turbulent kinetic energy (TKE) spectrum. This formulation is based on the model of Arunajatesan and Sinha [25], which was developed assuming low speed flow. In this regard, the Karman-Pao energy spectrum model, which is widely used and well accepted as a good candidate for purely incompressible flows, was used to develop the original formulation [25]. However, this formulation has been upgraded to account for compressibility effects to extend its range of application to blast predictions.

Flow ccompressibility affects the TKE spectrum as illustrated in Figure 3 [26]. From this figure, note that both the slope of the spectrum in the inertial wavenumber regime, as well as the decay rate in the dissipation range are affected by compressibility. The non-dimensional compressibility parameter (used to characterize the magnitude of compressibility) that is widely used in the literature is that of the turbulent Mach number, $M_\tau = \sqrt{\frac{2k}{\gamma RT}}$, which is a ratio of the turbulent velocity scale to the acoustic speed.

To account for the effects of compressibility, the turbulent kinetic energy is decomposed into a solenoidal and a compressible component, written as:

$$E\left(k\right) = E_s\left(k\right) + E_c\left(k\right), \tag{43}$$

where,

$$E_s\left(k\right) = C_s k_e^{-5/3}\left(\frac{k}{k_e}\right)^4\left[1+\left(\frac{k}{k_e}\right)^2\right]^{-17/6}\exp\left(-\frac{3}{2}ak^{4/3}\right), \tag{44}$$

is the solenoidal component that is represented by the Karman-Pao empirical model, and,

$$E_c\left(k\right) = C_c f(k_e, M_\tau), \tag{45}$$

is the compressible part of the energy that scales with the square of turbulent Mach number, M_τ. Note that these equations are non-dimensionalized and use the non-dimensional wavenumber, $k = k\eta$, where $\eta = \left(\upsilon^3 / \varepsilon\right)^{1/4}$ is the Kolmogorov dissipation length scale. The function parameterizing the compressible component of the spectrum is curve-fit from data (as seen in Figure 4) in terms of M_τ and k_e. The ratio of the compressible energy to the solenoidal energy (see Figure 5) is also curve-fit as a function of M_τ and the Taylor-scale Reynolds number, given by

$$\mathrm{Re}_\lambda = \left(\frac{20}{3}\right)^{1/2} \frac{k^{RANS}}{\sqrt{\upsilon\varepsilon}} = \int_0^1 \hat{E}(\hat{k})d\hat{k}\,. \tag{46}$$

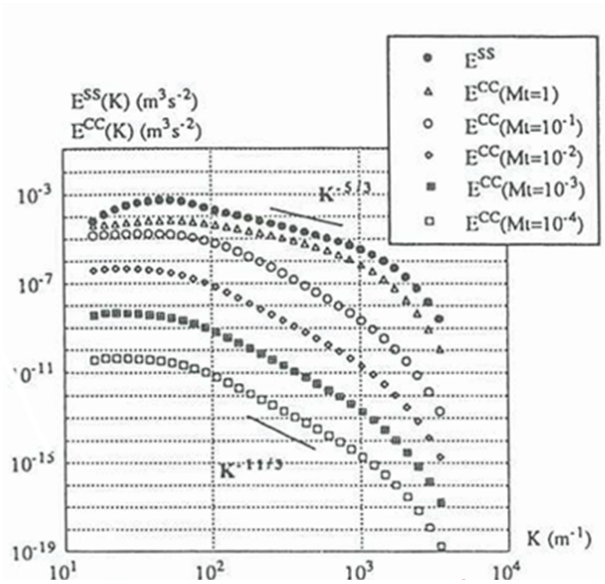

Figure 3. Turbulent Kinetic Energy Spectra [26]

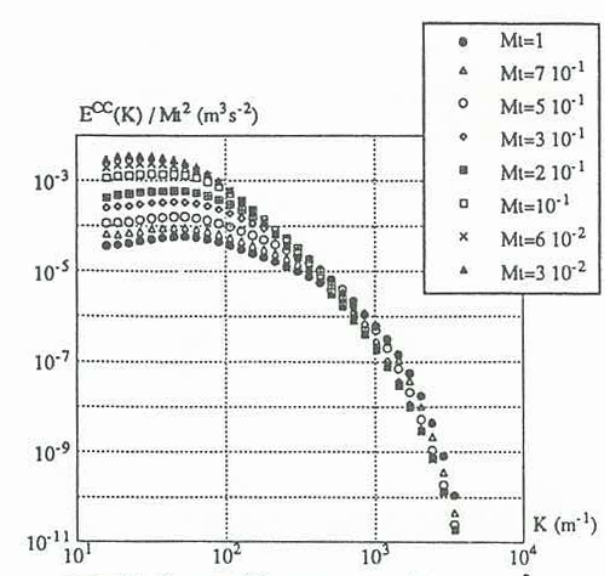

Figure 4. Compressible Energy Spectra Normalized by M_τ^2 [26]

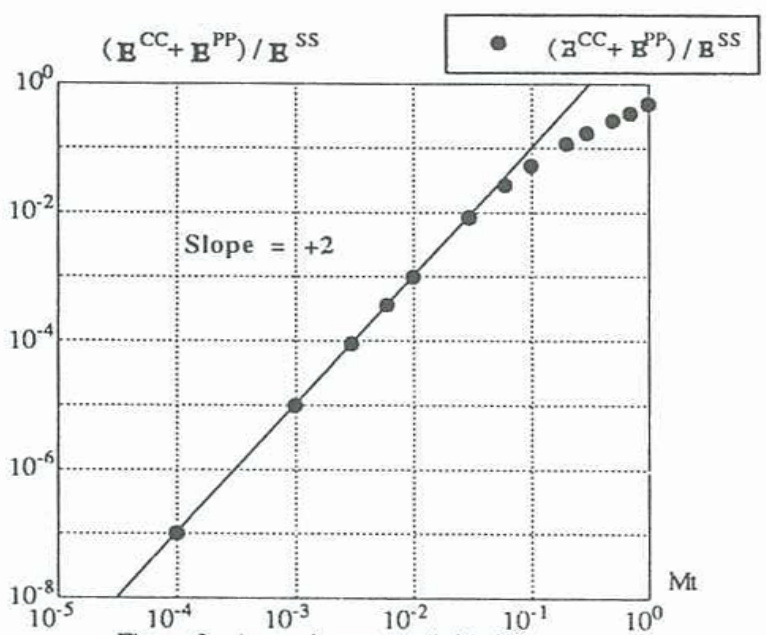

Figure 5. Acoustic Energy Divided by the Solenoidal Energy as a Function of M_τ [26]

Note that the model parameters C_s, C_c and k_e need to be determined in terms of the two independent variables Re_λ and M_τ. C_s and C_c are the constants multiplying the energy components E_s (solenoidal) and E_c (compressible) respectively, while k_e is the dominant energy carrying wavenumber (non-dimensional) in the spectrum. Just as in the original model formulation [25], the eddy-viscosity in the LES regions is damped by the f_{hybrid} function that is now a function of both Re_λ and M_τ.

$$\nu_{T,LES} = f_{hybrid}\nu_{T,RANS} = f_{hybrid} f_\mu C_\mu \frac{k_{rans}^2}{\varepsilon_{rans}}. \tag{47}$$

In order to determine the three model parameters C_s, C_c and k_e, the following set of equations (three) need to be solved:

$$\begin{aligned} \mathrm{Re}_\lambda &= \sqrt{\frac{20}{3}}\left[C_s E_s\left(k\right) + C_c M_\tau{}^2 E_c\left(k\right)\right] \\ 1 &= \left[C_s D_s\left(k\right) + C_c M_\tau{}^2 D_c\left(k\right)\right] \\ \frac{E_c\left(k\right)}{E_s\left(k\right)} &= g(\mathrm{Re}_\lambda, M_\tau). \end{aligned} \tag{48}$$

The first equation above is that the sum of the integrals of the two components of the energy (non-dimensional) which should equal Re_λ, while the second equation is that the sum of the integrals of two components of the dissipation of energy that is equal to the non-dimensional dissipation rate, $\varepsilon \equiv 1$. The last equation is a ratio of the compressible to the solenoidal energy. The above set of three equations is solved for the three model parameters for a range of values of

the independent variables Re_λ and M_τ. The surfaces of these model parameters are shown in Figure 6. Note that all the parameters asymptote to a constant value in the high Reynolds number limit. Once the three model parameters are determined, the entire energy spectrum is known. Then, for different values of the mesh-scale to the energy-carrying length scale, Δ / l_e the subgrid-scale eddy-viscosity, $\nu_{T,LES}$ is evaluated by integrating the energy and the dissipation spectrum from the mesh-length scale, Δ, to infinity (or the smallest scales, i.e., the Kolmogorov scale, $\eta = \left(\upsilon^3 / \varepsilon\right)^{1/4}$).

$$k^{sgs} = \int_{k\Delta}^{\infty} E(k)\,dk; \quad \varepsilon^{sgs} = \int_{k\Delta}^{\infty} D(k)\,dk$$

$$\nu_{T,LES} = f_\mu C_\mu \frac{k_{sgs}^2}{\varepsilon_{sgs}}, \tag{49}$$

$$\nu_{T,LES} = f_{hybrid}\nu_{T,RANS}$$

The surface of the f_{hybrid} function is also shown in Figure 6. These surface functions are curve-fit and explicitly defined in terms of the two independent variables Re_λ and M_τ. Hence, at any given point in the flow field, the determination of these quantities along with a definition of the local mesh-length scale can be used to evaluate the f_{hybrid} function. This essentially damps the eddy-viscosity contribution for the given mesh-length scale based on that portion of energy un-sustainable by the local mesh, and hence is the "unresolved" energy local to this point.

The compressibility corrected (c.c.) HRLES model was first tested on a hot, over-expanded Mach 1.5 jet. Figure 7 presents instantaneous Mach number plots comparing the incompressible HRLES model and the HRLES model with c.c. A limitation of the incompressible model was a general over-prediction of eddy viscosity in the initial shear layer of the jet. This eddy viscosity was calculated assuming the incompressible energy spectra and therefore the original model tended to smooth the shear layer and delayed the evolution of jet turbulence. As can be seen in the lower part of this figure, correcting the energy spectra for compressibility naturally reduces the amount of eddy viscosity and allows the jet shear layer to "trip" sooner (closer to the nozzle lip). The amount of eddy viscosity reduction can clearly be seen in Figure 8.

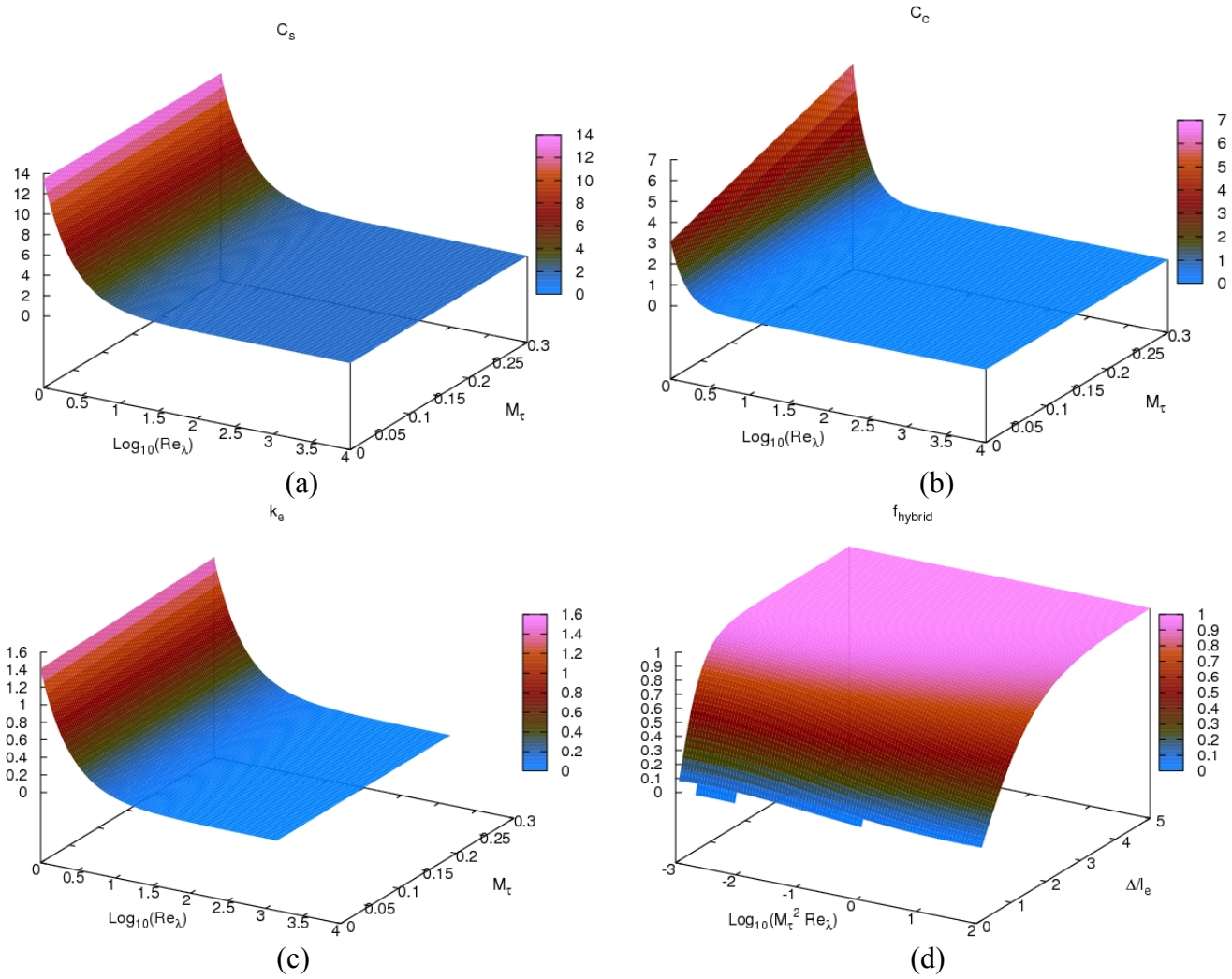

Figure 6. Surfaces of Model Parameters C_s, C_c, k_e and the f_{hybrid} Damping Function for the Eddy-viscosity in the HRLES c.c Model

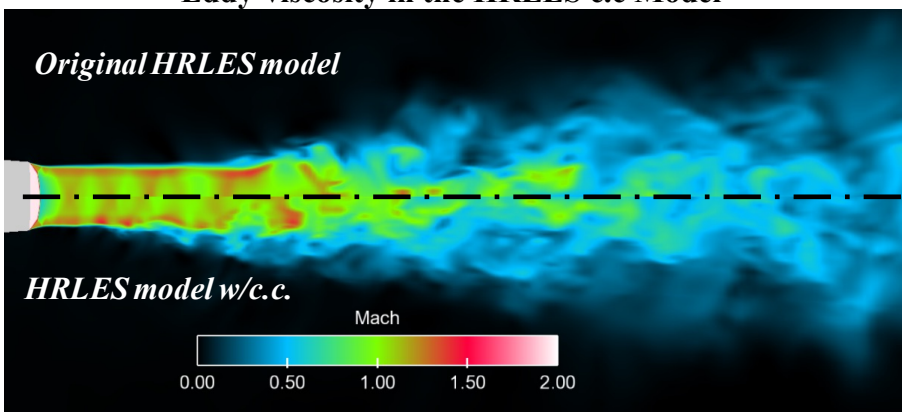

Figure 7. Mach Number Comparison of Incompressible HRLES Model with Compressibility Corrected HRLES Model

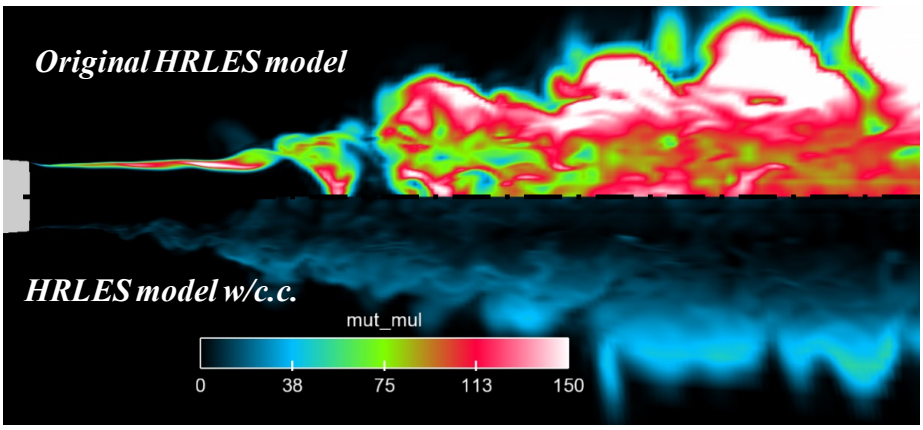

Figure 8. Eddy Viscosity Ratio Comparison of Incompressible HRLES Model with c.c. HRLES Model

6.2.4 Model Testing and Evaluation

As discussed earlier, this unified formulation was implemented within the production version of the CRAFT CFD® flow solver that has been developed for application to blast and biological warfare (BW) neutralization predictions. As an initial test of the formulation, a high speed shear layer configuration was considered to evaluate the effects of the turbulence modeling on live spore depletion or neutralization. This configuration was chosen for this initial test because spore neutralization within a blast configuration will primarily occur in turbulent shear regions between the ambient conditions (containing the spore constituents) and the blast flow. For this shear layer configuration, the low speed flow side consisted of air at 1 atm of pressure and an initial temperature of 300 K, and with a flow Mach number of 1.2. This low speed flow was also contaminated with spore constituents at a concentration of 10 ppm. The properties of these hypothetical spores with respect to the neutralization rate in Eqn. (24) were $\alpha = 100$, $\theta = 1$, $m = 0$, and $\beta = 350\,\mathrm{K}$. For the high speed side, the blast flow was modeled as reaction products with an excess of CO and H_2 in equal proportions at a pressure of 1 am and temperature of 2000 K, and with a flow Mach number of 2.5.

With these conditions, the spore model pre-processor developed under this program was used to generate the database for the spore particle – turbulent interaction model. This database includes model data for the mean or filtered live spore destruction rate, $\overline{\omega_L}$, and the source term $\overline{Y_L \omega_L}$ in the spore concentration variance equation given in Eqn. (29). These two terms are parameterized within the database as,

$$\left\{ \begin{matrix} \overline{\omega_L} \\ \overline{Y_L \omega_L} \end{matrix} \right\} = f(< Y_L >, < Y_L'^2 >, < T >, < T'^2 >) \qquad (50)$$

Figure 9 illustrates the effect of the pdf distribution used to model the temperature fluctuations on the mean spore destruction rate. This figure presents contours of the ratio of the turbulent spore destruction rate to the laminar destruction rate that neglects temperature fluctuations. These contours are plotted in the mean temperature – temperature variance plane. In this figure,

the upper boundary in temperature variance is nonlinear due to realizability constraints on the assumed pdf distribution for the temperature. As seen in the figure, the maximum realizable temperature variance is equal to zero at the minimum and maximum specified temperature range, and reaches a maximum value in between these limits at ~ 500 K. Over this realizable range, the effect of temperature fluctuations as seen in this figure is to *reduce* the mean spore destruction rate. As the temperature fluctuations become large, the mean destruction rate is seen to be reduced by ~ 50%. This model prediction has important implications for the assessment of prospective neutralization strategies. As the results in Figure 9 indicate, neglecting the effect of temperature fluctuations on the destruction rate could significantly *over estimate* the effectiveness of a neutralization strategy. As a result, it is important to include the effect of these fluctuations on any predictive assessment to provide a more conservative estimate of neutralization effectiveness.

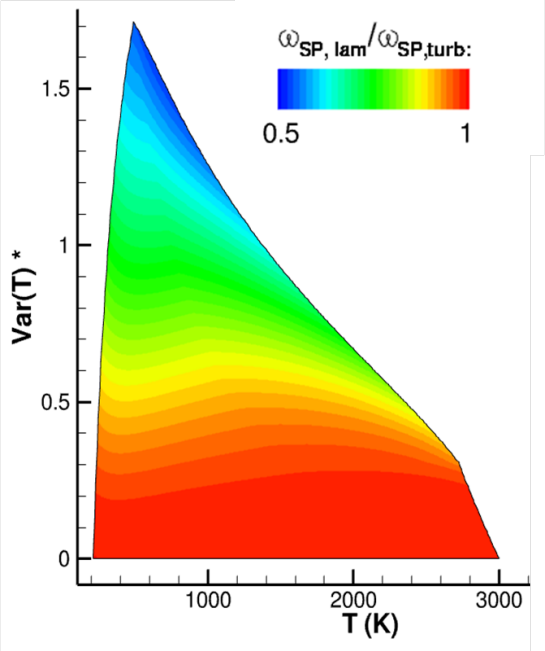

Figure 9. Contours of the ratio of the turbulent-to-laminar live spore destruction rate as a function of mean temperature and normalized temperature variance

Results for the application of the spore interaction model to the high speed shear layer case are presented in Figure 10. This figure presents contours of the normalized spore concentration within the shear layer for the laminar rate model and the HRLES – spore interaction model. In this figure, the low speed side of the shear layer with the spore contamination is on the top half, while the high speed blast flow is on the bottom half. For this case, the temperature variance for the spore interaction model case has been set to the maximum realizable value to illustrate the maximum possible effect of the model. Also, the streamwise scale of these contour plots has been dramatically scaled for clarity. From Figure 10, it is clear that under these conditions that spore destruction within the shear layer has been substantially reduced. The spore concentration in this figure is also seen to have not reached self-similarity within the shear layer, as indicated by the nonlinear nature of the contours. As a result, the laminar and turbulent rate model results will continue to diverge further downstream. The lack of self-similarity in this figure is a result of that fact that the chemical reactions within the shear layer have not reached self-similarity over the spatial domain of this figure. For this case, excess fuel in the blast flow is igniting along

the shear layer and the chemical reactions have not yet reached a steady state. Consequently, the results presented in Figure 10 also indicate that the spore interaction model is also sensitive to ignition phenomena occurring within the gas phase.

With this test of the spore interaction model completed, the model implementation within CRAFT CFD® was considered verified.

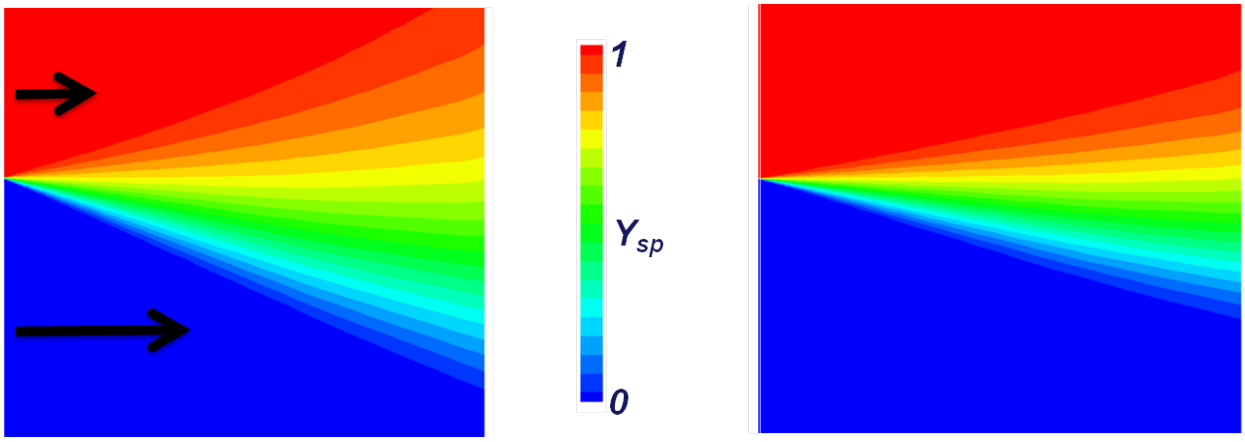

(a) Laminar spore destruction rate model (b) HRLES – spore interaction model

Figure 10. Contours of the normalized spore concentration within the reacting high speed shear layer

6.2.5 Biological AD Application

With the spore interaction model implementation now verified, the formulation was then applied to a high-fidelity blast event simulation of a *representative* aluminized high explosive (HE) charge in a *generic configuration* featuring an inner room within an outer room communicating through various openings. For this demonstration, the biological agent consisting of *b.T.* spores was assumed to be contained within 8 canisters distributed in a semi-circular pattern centered around the HE charge in the inner room. Due to the significant computational cost of time-accurate 3-D high-fidelity simulations of blast/AD scenarios, the biological agent release was intentionally localized close to the floor of the inner room, where turbulent fluctuations in temperature and the establishment of a high-temperature gas environment (HTGE) in direct contact with the spores are most likely to occur. This initialization is aimed at enhancing the effect of the turbulent HTGE on the spores in the very early stages of the post-detonation and therefore at reducing the required duration of the simulated overall event.

When the HE charge is first detonated, the resulting blast front propagates outwards in a complex three-dimensional pattern. Shocks are reflected off the floor and later from the walls. During this process, blast afterburning takes place as the detonation products mix with the air available in the inner room. As a result, the heat release from the blast afterburning further raises the temperature inside the inner room, thus providing a suitable HTGE for the spore demise. Due to the blast over-pressure, all vents and the door are at first choked and only outflow from the inner room takes place. As the simulation progresses, it is expected that, after reaching the peak pressure level in the inner room, the pressure starts dropping. As blast afterburning takes place, turbulent

mixing in a complex highly three-dimensional pattern controls and limits the rate of combustion. When pressure equilibration between the two rooms is reached, the vents and the doorway are no longer choked and flow reversal will take place. Fresh air from the outer room enters the inner room where reactants are still available at oxygen-lean conditions and hot products exit from the inner room in a pulsating flow pattern.

The *b.T.* spores are introduced into the inner room of the geometry during the HE charge post-detonation with a delay representative of the time required by HE charge casing fragments to hit and rupture the spore containers and release the clouds of biological agent. Based on representative empirical correlation for spores, the temperature dependence of the turbulent spore demise rate is illustrated in Figure 11. Specifically, Figure 11(a) presents a contour plot of the turbulent rate in temperature-temperature variance space, indicating a strong decay in the rate with decreasing temperature irrespective of the level of turbulent fluctuations. On the other hand, Figure 11(b) and Figure 11(c) show the ratio of laminar to turbulent spore demise rate on two different scales. This is intended to highlight the moderately inhibiting effect of turbulent fluctuations on the rate at high temperature (see Figure 11(b)) and the major enhancing effect in the lower temperature range. However, since the rate is small at low temperature, the overall effectiveness of the rate enhancement is mitigated. What these plots indicate is that a visible increase in the spore demise rate can be attained in the mid temperature range, if significant turbulence levels are present.

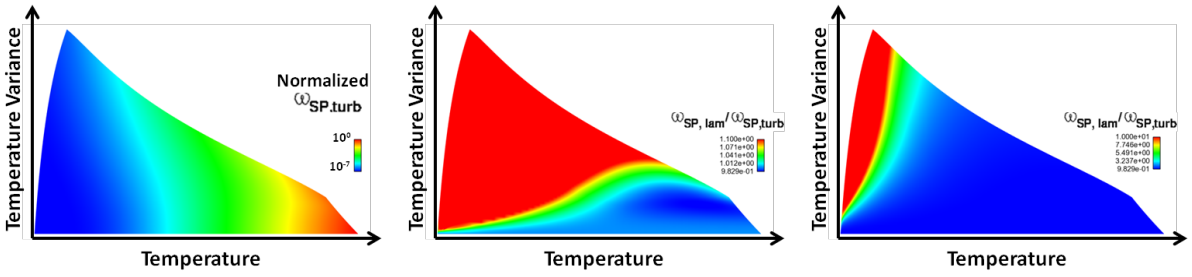

(a) (b) (c)

Figure 11. Contour plots in temperature - temperature variance space of (a) turbulent spore demise rate, and (b-c) ratio of laminar to turbulent spore demise rates using two different scales to emphasize enhancing/inhibiting effects.

A HRLES simulation on a moderately coarse grid based on half-plane symmetry and activating the spore particle-turbulence interaction model was carried out. Due to the significant computational cost, numerical stiffness and restrictive integration time steps, the early post-detonation dynamics of fireball expansion was simulated for a duration of 8 ms. The evolution in time of the volume-integrated normalized mass of alive spores is presented in Figure 12, indicating a rapid initial demise of the spores as the shock wave goes through the cloud of biological agent and a reduction in the rate as more uniform HTGE is established in its proximity.

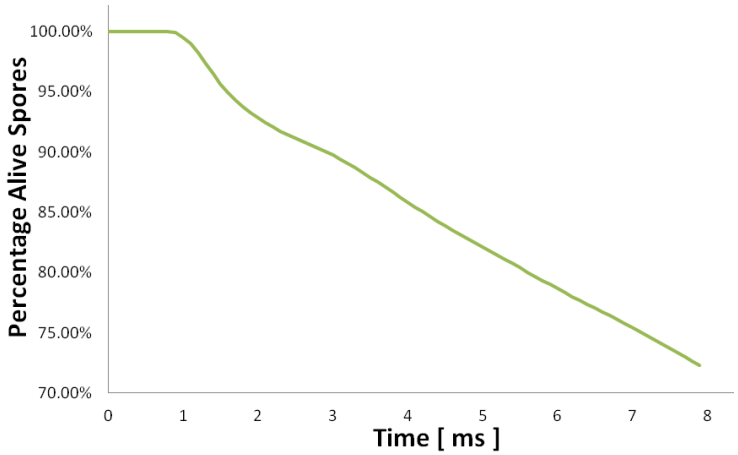

Figure 12. Volume-integrated normalized alive spore mass as a function of simulation time.

Selected snapshots of the pressure distribution inside the inner room are shown in Figure 13. The alive spore cloud is identified by iso-surfaces shown in yellow and the hot plume venting into the outer room from the ceiling vents and doorway by temperature iso-surfaces in orange. Similarly the temperature distribution corresponding to the same instants in time is presented in Figure 14. The deformation and destruction of the cloud of alive spores can be observed as the shock wave propagates through the cloud and gets reflected off the inner room walls and ceiling. Due to the way the HE charge was detonated, resulting in a predominantly downward-directed blast propagation, significant HTGE is established along the floor of the room, as indicated by the contours in Figure 14. While this simulation could potentially be carried out for hundreds of milliseconds to capture the entire dynamics of the blast/AD scenario, the present simulation of the early post-detonation stages serves as a demonstration of the upgraded modeling framework.

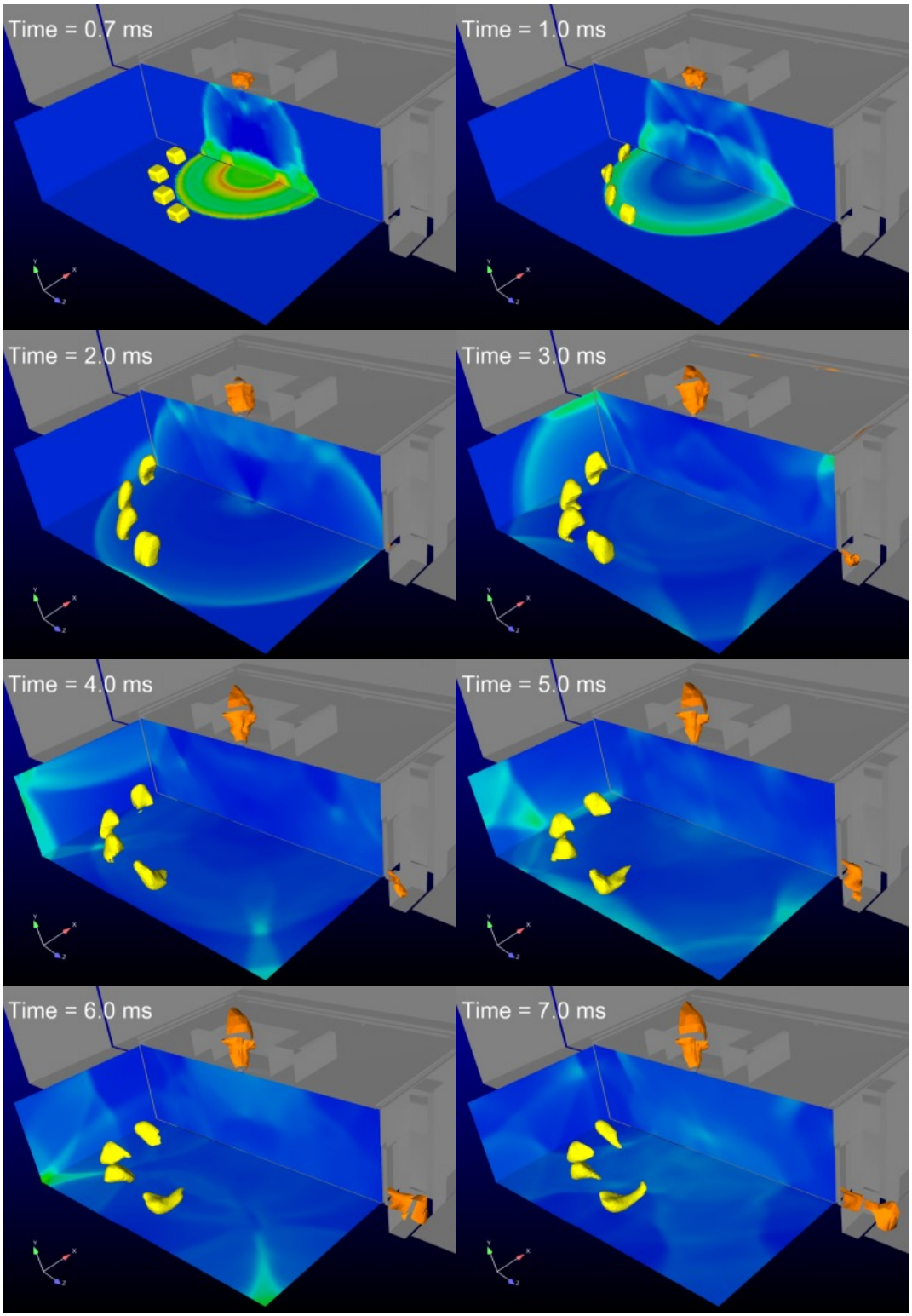

Figure 13. Pressure distribution in inner room for selected instants in time with alive spore iso-surface shown in yellow and temperature iso-surface shown in orange (outer room only).

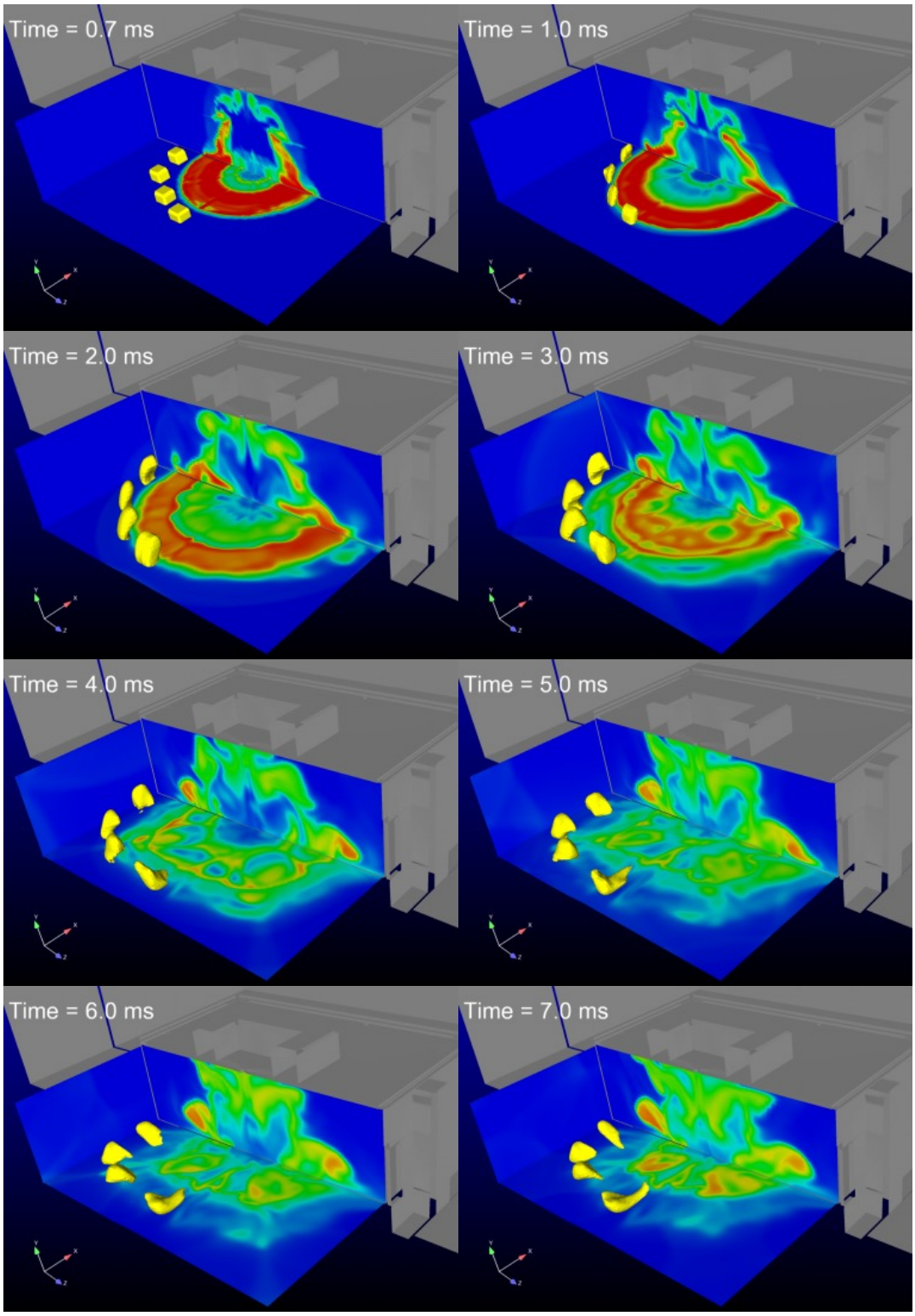

Figure 14. Temperature distribution in inner room for selected instants in time with alive spore iso-surface shown in yellow.

6.3 Task 2.4: Turbulence Model Extensions for the Continuum Phase Combustion

This task considers turbulence model extensions to include turbulence – chemistry interaction modeling for the gas phase combustion. The focus of this modeling effort is to develop and implement turbulent combustion models that are tractable for large scale, production level blast applications. As a result, the first phase of this task considers the implementation of a standard, generally applicable, first order turbulent combustion model. The second phase of this task considers extension of a more comprehensive modeling approach for blast applications. This work period, phase one of this task was completed and phase two was initiated as will be describe next.

For the first phase of this task, the Eddy Dissipation Concept (EDC) [27] model was implemented within CRAFT CFD®. This formulation was originally developed by Magnussen and Hjertager [27] to provide a first order effect of turbulent fluctuations on chemical reactions. The EDC model recognizes that combustion only occurs in molecularly mixed fine scale structures of the flow. These fine structures only comprise a small fraction of the total volume of the fluid. Geometrically, these structures have a thickness on the order of the Kolmogorov microscale and form broad sheets that are convoluted by large scale turbulence. This theory assumes these fine scale structures are thick compared with the Kolmogorov microscale and are therefore homogeneously mixed by small scale turbulence. These structures may then be modeled using a perfectly stirred reactor (PSR). When chemical kinetic rates are fast, combustion in the fine scale structures depends only on the mass transfer rate from the surrounding inert fluid to the fine structures. When chemical kinetic rates are slow, combustion within the fine structures will depend on the fine scale Damkohler number, Da^*, given by,

$$Da^* = \tau / t_{chem} \tag{51}$$

where τ is the fine structure time scale or small scale turbulent strain rate. For RANS applications, Byggstøyl and Magnussen [28] developed the following expression for τ based on turbulent scaling relations,

$$\tau = C_s \left(\frac{\nu}{\varepsilon} \right)^{1/2} \tag{52}$$

where ε is the turbulent kinetic energy dissipation rate, ν is the mean kinematic viscosity and C_s is a calibration coefficient typically take as $C_s = 0.411$. The volume fraction of the reacting fine scales, f_r, is also given by [29],

$$f = \frac{\gamma^2}{(1-\gamma^3)},\ \gamma = C_\gamma \left(\frac{\nu\varepsilon}{k^2} \right)^{1/4} \tag{53}$$

where k is the turbulent kinetic energy and C_γ is a calibration coefficient typically taken as $C_\gamma = 2.13$. With Eqn. (52) and (53), the EDC model may be implemented for finite rate chemistry using an stiff ordinary differential equation (ode) chemistry solver. In this context, the mean or filtered chemical chemical production rate for the kth species is given by,

$$\overline{\omega_k} = \bar{\rho} \frac{\int_0^{\tau} \omega_k dt}{\tau} \frac{\gamma^2}{(1-\gamma^3)} \tag{54}$$

The primary effect of the EDC model is to reduce chemical production when turbulent fluctuations are present. This typically has the effect of reducing flame temperatures and product formation. For example, Figure 15 presents radial temperature profiles for a low speed hydrogen – air jet diffusion flame [30] at an axial station of x/D = 22.5. Included in this plot are the EDC model results, laminar chemical rate results, and experimental data. As seen in this figure, the EDC model reduces the peak mean temperature to produce a slightly better prediction than when turbulent fluctuations are neglected within the chemical production rate formulation.

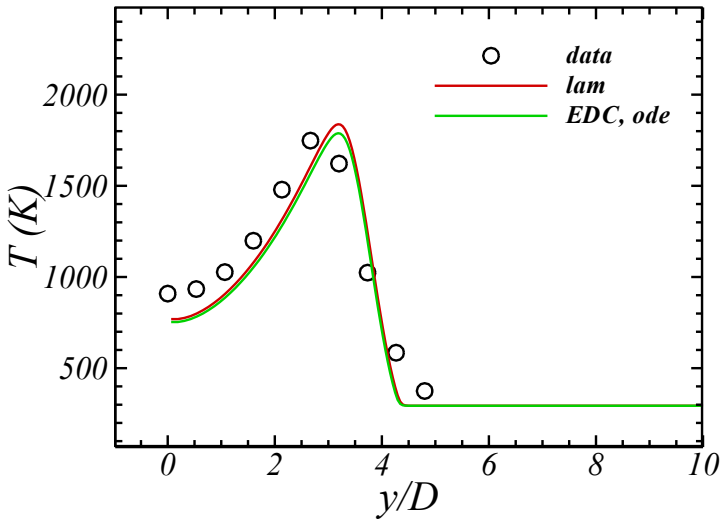

Figure 15. Favre mean temperature profile at x/D = 22.5.

As discussed earlier, the EDC model is generally applicable and computationally inexpensive, but it only provides for a first order accurate representation of turbulence – chemistry interactions within the flow. For phase two of this task, efforts were initiated this work period to enhance the accuracy of the turbulent combustion modeling while still maintaining a tractable formulation. In coordination with Georgia Tech, the focus of these efforts was on employing the linear-eddy model (LEM) [31][32] for turbulent combustion. The LEM is a comprehensive stochastic mixing model that separately treats molecular diffusion (with finite-rate kinetics) and small scale turbulent stirring. This modeling formulation has been the focus of Georgia Tech combustion modeling for many years due to the advanced nature of the model. The LEM has been implemented by Georgia Tech as an LES subgrid model [33]. This implementation includes a LEM stochastic simulation within each LES subgrid domain during a run-time simulation. Though very comprehensive and accurate, this implementation is intractable for large scale, production level blast applications due to the computational cost of the inline stochastic simulations. As an alternative, the LEM may be included through a procedure called *stochastic model parameterization* [34]. Using this procedure, statistics from the LEM are pre-

computed before a run-time simulation and parameterized in terms of a reduced set of variables to form a computationally inexpensive database of the model. This type of approach has been developed for nonpremixed, partially premixed [34], and premixed [35] flows in the context of the low speed flow regime. This type of approach has the advantage of computational efficiency and could be a viable modeling approach for BW neutralization predictions. However, to be feasible this formulation will require its extension to the compressible flow regime.

6.4 References

[19] Peters, N., Turbulent Combustion, Cambridge University Press, Cambridge, UK, 2000.

[20] Calhoon, W.H., Jr., Brinckman, K.W., Tomes, J., Mattick, S. and Dash, S.M.., "Scalar Fluctuation and Transport Modeling for Application to High Speed Reacting Flows" AIAA Paper No. AIAA-2006-1452, 44th Aerospace Sciences Meeting and Exhibit, Reno, NV, Jan. 9-12, 2006.

[21] Gaffney, R.L., Jr., White, J.A., Girimaji, S.S. and Drummond, J.P., "Modeling Turbulent and Species Fluctuations in Turbulent, Reacting Flow, " *Computing Systems in Engineering*, Vol. 5, No. 2, pp. 117–133, 1994.

[22] Yetter, R., Private Communications, Penn State University, August, 2007.

[23] Sankaran, V., Drozda, T.G., and Oefelein, J.C., "A Tabulated Closure for Turbulent Non-premixed Combustion Based on the Linear Eddy Model," *Proceedings of the Combustion Institute*, Vol. 32, pp. 1571 – 1578, 2009.

[24] Brinckman, K.W., Calhoon, W.H., Jr., Mattick, S.J., Tomes, J., and Dash, S.M., "Scalar Variance Model Validation for High-Speed Variable Composition Flows," *44th AIAA Aerospace Sciences Meeting and Exhibit*, Reno, NV, AIAA Paper 2006-0715, January 9–12, 2006.

[25] Arunajatesan, S., and Sinha, N., "Hybrid RANS/LES Modeling for Cavity Aeroacoustics Predictions," *Journal of Aeroacoustics*, Vol. 2, No. 1, pp. 65-93, 2003.

[26] Bataille, F., and Bertoglio, J. P., "Spectral Study of Weakly Compressible Turbulence," 11th Autralasian Fluid Mechanics Conference, University of Tasmania, Hobart, Australia, 14-18 Dec. 1992.

[27] Magnussen, B. F., and Hjertager, B. H., "On Mathematical Modeling of Turbulent Combustion with Special Emphasis on Soot Formation and Combustion," *Sixteenth Symposium (International) on Combustion*, The Combustion Institute, 1976, pp. 719–729.

[28] Byggstøyl, S. and Magnussen, B.F., "A Model for Flame Extinction in Turbulent Flow," in *Turbulent Shear Flows 4*, eds. Bradury et al., Springer-Verlag, New York, 1983, pp. 381–395.

[29] Gran, I. R. and Magnussen, B. F., "A Numerical Study of a Bluff-Body Stabilized Diffusion Flame. Part 2. Influence of Combustion Modeling and Finite-Rate Ghemistry", Combustion Science and Technology, 119:191, 1996.

[30] Janicka, J. and Kollman, W., "A Two-Variable Formalism for the Treatment of Chemical Reactions in Turbulent H_2-Air Diffusion Flames," Seventeenth Symp. (Int.) on Combustion, The Combustion Institute, p. 421, 1979.

[31] Kerstein, A. R., "Linear-Eddy Model of Turbulent Transport II. Application to Shear Layer Mixing," *Combustion and Flame*, Vol. 75, pp. 397–413, 1989.

[32] Kerstein, A. R., "Linear-Eddy Model of Turbulent Transport 4. Structure of Diffusion-Flames," *Combustion Science and Technology*, Vol. 81, pp. 75–96, 1992.

[33] Chakravarthy, V. K. and Menon, S., "Linear-Eddy Simulations of Reynolds and Schmidt Number Dependencies in Turbulent Scalar Mixing," *Physics of Fluids*, Vol. 13, pp. 488–499, 2001.

[34] Calhoon, W. H. Jr., Zambon, A., Sekar, B., and Kiel, B., "Subgrid Scale Combustion Modeling Based on Stochastic Model Parameterization," *J. of Engineering for Gas Turbines and Power*, Vol. 134, No. 3, Mar 2012, pp. 031505-1 – 031505-12.

[35] Kemenov, K.A., Calhoon, W.H. Jr., and Zambon, A., "Large-scale strain rate effects on the premixed flame propagation in LES of a lean swirl-stabilized gas turbine combustor," AIAA Paper 2013-0173, presented at the 51st AIAA Aerospace Sciences Meeting, Grapevine, TX, Jan. 7 – 10, 2013.

7.0 YEAR 3 AND 4 ACTIVITIES

Due to the sensitive nature of the work performed in Year 3 and 4 pertaining to applications to agent defeat problems of interest to DTRA, two (2) separate detailed reports were delivered directly to DTRA in July 2014 and December 2015.

In addition, CRAFT Tech has actively participated in the December 2015 Simulant Chemistry Workshop organized by DTRA. This was an excellent opportunity to further strengthen the link between DTRA's Basic Research portfolio and the applications side of DTRA's activities.

DEPARTMENT OF DEFENSE

DEFENSE THREAT REDUCTION
AGENCY
8725 JOHN J. KINGMAN ROAD
STOP 6201
FORT BELVOIR, VA 22060
ATTN: A. DALTON

DEFENSE TECHNICAL
INFORMATION CENTER
8725 JOHN J. KINGMAN ROAD,
SUITE 0944
FT. BELVOIR, VA 22060-6201
ATTN: DTIC/OCA

DEPARTMENT OF DEFENSE CONTRACTORS

QUANTERION SOLUTIONS, INC.
1680 TEXAS STREET, SE
KIRTLAND AFB, NM 87117-5669
ATTN: DTRIAC

OTHER

GEORGIA INSTITUTE OF
TECHNOLOGY
270 FERST DR
ATLANTA, GA 30332
ATTN: S. MENON
M. AKIKI